Perspectives of Cost-Efficient GNSS Equipment for Wide-Spread and High-Quality Meteorological and Positioning Applications

Krietemeyer, A.

DOI
10.4233/uuid:1491f45d-103e-49db-8688-5e9cd1273f0b

Publication date
2021

Document Version
Final published version

Citation (APA)
Krietemeyer, A. (2021). *Perspectives of Cost-Efficient GNSS Equipment for Wide-Spread and High-Quality Meteorological and Positioning Applications*. [Dissertation (TU Delft), Delft University of Technology]. https://doi.org/10.4233/uuid:1491f45d-103e-49db-8688-5e9cd1273f0b

Important note
To cite this publication, please use the final published version (if applicable).
Please check the document version above.

PERSPECTIVES OF COST-EFFICIENT GNSS EQUIPMENT FOR WIDE-SPREAD AND HIGH-QUALITY METEOROLOGICAL AND POSITIONING APPLICATIONS

PERSPECTIVES OF COST-EFFICIENT GNSS EQUIPMENT FOR WIDE-SPREAD AND HIGH-QUALITY METEOROLOGICAL AND POSITIONING APPLICATIONS

Proefschrift

ter verkrijging van de graad van doctor
aan de Technische Universiteit Delft,
op gezag van de Rector Magnificus Prof.dr.ir. T.H.J.J. van der Hagen,
voorzitter van het College voor Promoties,
in het openbaar te verdedigen op maandag 17 mei 2021 om 15:00 uur

door

Andreas KRIETEMEYER

Master of Engineering,
University of Applied Sciences Neubrandenburg, Duitsland,
geboren te Neubrandenburg, Duitsland.

Dit proefschrift is goedgekeurd door de

promotor: Prof.dr.ir. N.C. van de Giesen
promotor: Dr.ir. J.A.E. ten Veldhuis

Samenstelling promotiecommissie:

Rector Magnificus,	voorzitter
Prof.dr.ir. N.C. van de Giesen,	promotor, Technische Universiteit Delft
Dr.ir. J.A.E. ten Veldhuis,	promotor, Technische Universiteit Delft
Onafhankelijke leden:	
Prof.dr.ir. R. Uijlenhoet	Technische Universiteit Delft
Prof.dr. L.G. Evers	Technische Universiteit Delft, KNMI
Prof.dr. G. Venuti	Politecnico di Milano, Italië
Prof.dr. J. Wickert	Technische Universität Berlin, Geoforschungszentrum Potsdam, Duitsland
Dr.ir. H. van der Marel	Technische Universiteit Delft

Keywords: GNSS, Water Vapor, Zenith Tropospheric Delay, Antenna Calibration, low-cost, Phase Center Variation, goGPS, ZED-F9P
Printed by: Ipskamp Printing
Front & Back: Andreas Krietemeyer

ISBN 978-94-6421-351-5

An electronic version of this dissertation is available at
`http://repository.tudelft.nl/`.

Writing briefly takes far more time than writing at length.

Johann Carl Friedrich Gauß

CONTENTS

SUMMARY

Whether in cars, smartphones, watches or fitness-trackers - the use of Global Navigation Satellite Systems (GNSS) has become a part of our daily life. Currently there are more than 100 GNSS satellites in orbit. They are routinely utilized for positioning and timing purposes, but their signals can also be used to monitor our environment. The basic principle GNSS measurements rely on is measuring the time difference between the transmitted signal of the satellite antenna and the receiving antenna (typically on the ground). While propagating through the atmosphere, the signal is delayed by the physical properties of the particles in its various layers. This delay is traditionally seen as undesired noise that should be eliminated from the data. This noise however also includes information about the state of the atmosphere which can be described by various parameters. One of such parameters is the delay caused by the 'wet' particles (predominantly water vapor) in the troposphere (lower 20km of the atmosphere). Weather models can use this information to correct the amount and location of atmospheric humidity which has proved to be beneficial for rainfall forecasts. To extract this information from the total signal delay, the delay caused by the ionosphere (upper part of the atmosphere, up to about 1000km) must be eliminated. A standard method is to make use of the dispersive character of the ionized particles in this layer and to eliminate the majority of this error by forming a so-called ionosphere-free linear combination. This requires signals on at least two different frequencies. Traditionally, only geodetic instruments e.g. utilized as permanent ground receivers operated by (inter-) national organizations use hardware that track GNSS signals on at least two frequencies. Such receivers are expensive (in the order of several thousand Euros) and as a result many GNSS networks outside developed areas lack the station density that is needed to capture the complex distribution of atmospheric water vapor. A densification for meteorological purposes with geodetic-grade GNSS receivers and antennas is economically not feasible. Similarly, local precision positioning equipment is not accessible for many regions, foremost situated in the Global South, due to the coarse distribution of static GNSS ground stations and expensive equipment to perform surveying tasks.

Technological advances in recent years enabled the release of cost-efficient single- and dual-frequency GNSS receivers and antennas which may offer an alternative to the high-grade technology. However, the use of consumer-grade hardware is associated with challenges that need to be overcome. In this thesis, the performance of low-cost GNSS receivers in combination with antennas of a range of different type and qualities for high-precision applications was analyzed. In particular, the efficiency of using this equipment for meteorological and positioning applications was experimentally quantified and methods to enhance their performance were developed and implemented.

At first, as an alternative to geodetic-grade (multi-frequency, cost-intensive) receivers, only low-cost single-frequency receivers were available. GNSS observations on only a

single frequency impose a challenge to remove the error caused by the ionospheric influence on the signal. To process the single-frequency observations in Precise Point Positioning (PPP) mode, the Satellite-specific Epoch-differenced Ionospheric Delay (SEID) model was used. It relies on a surrounding network of dual-frequency stations. To represent a more realistic scenario for regions with low GNSS ground station density, two outside network configurations with inter-station distances of 50-80 kilometers and 200-300 kilometers were considered. The research setup enabled distinguishing between software, ionospheric and hardware related sources of error on the Zenith Tropospheric Delay (ZTD) estimations. It was demonstrated that single-frequency receivers can obtain similar quality results compared to those of geodetic-grade setups. Depending on the utilized antenna, the Root Mean Square Errors (RMSE) were between 4-7 mm using an outside network with inter-station distances between 50 and 80 km and about 10-12 mm with distances between 200 and 300 km. It was found that modeling of the ionosphere and the antenna type are the main sources influencing the ZTD precision.

By the end of 2018, low-cost dual-frequency receivers were released to the market. Observations on two frequencies enable eliminating the majority of the ionospheric error. This avoids the need of an outside network to account for this error source. As indicated in the study using single-frequency receivers, the receiving antenna appears to be a limiting factor of the outcome quality. For this purpose, the ZTD performance of a low-cost dual-frequency receiver in combination with a range of different quality antennas was analyzed. It was found that the receiver was very well capable of achieving high-quality ZTD estimations when the Phase Center Variations (PCVs) of the receiving antenna were known and included in the processing chain. Since antenna calibrations are typically not available for low-cost antennas, a relative antenna calibration was performed on-site. To achieve this, a base (in our case, a geodetic-grade receiver and antenna) and a rover (the low-cost dual-frequency receiver with different antennas) were used to form a short baseline. Over a short baseline, many errors, e.g. those caused by the troposphere and ionosphere, are the same for both stations and are cancelled by the differential processing. The remaining residuals contain primarily the differences between the phase variations from both antennas. The residuals together with the known antenna calibration from the base station were used to generate new absolute PCVs for each investigated rover antenna. After applying the newly derived PCVs, the ZTD RMSE using a low-cost antenna (when using a circular ground plane) was reduced from between 15-24 mm to about 4 mm. This level is excellent for meteorological applications. It opens the way for a wide-spread implementation of low-cost GNSS receiver and antenna setups.

Inspired by the ZTD results obtained with the low-cost dual-frequency receiver and self-calibrated antennas, the positioning performance of such setups were analyzed. For this purpose, the residuals and positioning results were examined in detail before and after applying the self-derived antenna calibrations. Considering that antenna-induced effects cancel over a short baseline if both antennas have the same phase characteristics, the same geodetic-grade antenna model (with known antenna calibrations) was used as a reference in our base and rover setup. Compared to this scenario, the conducted antenna calibration with low-cost antennas could reduce the L1 and L2 residual differences from between 30-90% to 12-52%. The estimated height component RMSE was improved

from 6-7 mm to 4 mm, a level which is close to those of geodetic-grade antennas. Additionally, the procedure to calibrate an antenna, if observations from a base and rover setup are available, was published online (gnss-antcal.citg.tudelft.nl) as a web-tool. It allows users to generate their own antenna calibrations directly in the field and promotes wide-spread application of the presented method.

1

INTRODUCTION

1.1. IRRIGATING THE DATA DESERT WITH COST-EFFICIENT GLOBAL NAVIGATION SATELLITE SYSTEM EQUIPMENT

'DER Weise äußert sich vorsichtig, der Narr mit Bestimmtheit über das kommende Wetter.' (analogous translation: The wise man comments carefully, the fool with certainty about the upcoming weather). This quote of the German poet Wilhelm Busch was not only valid during his lifetime (1832-1908), but also today. Weather forecasting is still not completely reliable, and it requires continuous efforts to understand, but also monitor weather processes to model them effectively. Whether it is too hot, too cold, too rainy, or too dry, everybody feels different about the weather. As a quote by the English art critic John Rushkin states: 'Sunshine is delicious, rain is refreshing, wind braces us up, snow is exhilarating; there is really no such thing as bad weather, only different kinds of good weather.' From choosing clothes, planning outdoor activities over to issue weather warnings to the people, predicting the weather is important for many social activities as well as commercial endeavors. In certain parts of the world, the weather forecasts are especially unreliable. As an example, a rainfall forecast in Africa for the next day is only as good as one for next week in Europe [1]. Besides the different climatological regions and the knowledge of the underlying physical processes, a main distinction between the European and the African situation is the observation density. Whilst Europe is covered with a dense network of multi-disciplinary ground observatories supplemented by satellite observations, this is only partially the case in Africa and the sparse observation network coverage causes large uncertainties [2].

For weather modeling the conditions in the vertical structure of the atmosphere are of particular importance. According to the physical properties, the atmosphere can generally be divided into several layers. Regarding signal propagation, we distinguish between the troposphere and the ionosphere. The weather as we experience it every day is happening almost entirely in the troposphere. The average height of it is about 17 km in mid-latitude regions. Monitoring the current state of it is a multidisciplinary task and an important part of forecasting the coming weather. High temporal and preferably high

spatial resolution measurements with high reliability are desired for this task. Classical parameters such as temperature, air pressure and wind speed, but also the amount of water vapor in the air are very important parameters. Especially water vapor is crucial for convection in the lower atmosphere and hence essential for the generation of clouds and rainfall. One possibility to monitor water vapor is by making use of signals from Global Navigation Satellite Systems (GNSS). In a nutshell, GNSS measures the distances between the satellites orbiting the Earth and the ground receiver. For precise GNSS analyses, basically two major processing modes exist, Precise Point Positioning (PPP) and a differential (relative) mode. PPP uses undifferenced observations and relies on precise satellite orbit and clock information to estimate parameters (e.g. coordinates, receiver clock, or troposphere errors) for each individual station. The differential processing technique (typically based on double-differences) gives high precision relative estimations between the stations of a network of two or more receivers. Both layers, troposphere, and ionosphere, delay the incoming signal. To estimate the delay caused by the 'wet' particles in the troposphere (predominantly water vapor), the signal delay caused by the ionosphere must be removed from the total delay. This is traditionally done with dual-frequency receivers. The main advantage of dual-frequency measurements is the possibility to exploit the dispersive character of the ionosphere which allows removing most of the delay caused by this layer of the atmosphere by a so-called ionosphere-free linear combination of observations on two frequencies. For long baselines in the network processing or in the PPP application, the ionosphere-free linear combination is used. Since particularly the humidity information e.g. from weather models are not sufficient for highest accuracy GNSS measurement analysis, the troposphere parameters are estimated in the GNSS processing. The GNSS signals typically do not arrive from the zenith direction and their propagation time caused by the troposphere increases the lower the observed satellite is. The observations are therefore a function of the elevation angle of the individual satellite. The tropospheric delays affecting the different observations, called slant delays, are mapped to the zenith direction yielding the Zenith Tropospheric Delay (ZTD). Together with surface meteorological parameters (temperature and pressure) at the station position, the ZTD can be converted to Precipitable Water Vapor (PWV) estimations.

GNSS-derived ZTD and PWV estimations proved to be valuable for the forecasting of rainfall in general [3] but are also crucial for smaller scale convective events [4]. Many initiatives, especially in Europe, America and Asia started to effectively integrate GNSS products in global and regional weather forecasts. Especially in the case of early warning systems, the high reliability and high temporal resolution of GNSS stations, delivering observations under all weather conditions, makes them an important part of the atmospheric observation scheme. Most regions that effectively use GNSS-derived products in their weather models have set up dense observation networks. As an example, in Europe, the EUMETNET EIG GNSS water vapor programme started in 2004 as an operational GNSS meteorology system and consists currently of about 3500 stations. Monitoring of atmospheric water vapor works well in areas with good coverage. The installation of dense networks is, however, limited by the substantial investment costs associated with it. Typical geodetic receiver-antenna setups are in the order of several thousand Euros. This is part of the reason why countries in the Global South have a sparse coverage of

GNSS stations that can be used for atmosphere monitoring.

This thesis work was motivated by the introduction of low-cost GNSS receivers on the market. Initially, only single-frequency GNSS receivers were available as an alternative to their expensive dual-frequency counterparts. However, measurements on only one frequency impose an additional challenge, as removing the delay caused by the ionosphere relies on modeling of the ionosphere. A solution for this is to use an existing network of surrounding dual-frequency receivers to model the state of the ionosphere for the single-frequency receivers inside. The possible model used for this densification is the Satellite-specific Epoch-differenced Ionospheric Delay (SEID) model. The impact on the tropospheric delay estimations in an experimental setting are discussed later in this thesis.

By the end of 2018, also affordable dual-frequency receivers were introduced to the market. With this type, it is no longer required to rely on an existing nearby dual-frequency network to model the ionosphere. Instead, the dispersive property of the ionosphere can be exploited by utilizing the linear combination of observations on two frequencies. The drawback of this method is however, that the noise in the data is multiplied by a factor of about 3. This makes the low-cost equipment particularly vulnerable to errors, especially those introduced by unmodeled characteristics of the phase center of the low-cost receiving antennas. This is because the position of the antenna phase center is generally not aligning with the geometric center of the antenna and behaves differently depending on the direction and the frequency of the incoming signal. Whilst traditional GNSS antennas used for geodetic networks are typically manufactured to comply with high precision requirements to reproduce identical mean antenna phase centers for each antenna, this is not the case for low-cost antennas, as these are mass-produced. So far, no antenna calibrations for commonly used low-cost dual-frequency antennas are openly available. A new antenna calibration method for direct field applications is developed and the impact on the positioning and tropospheric estimations are discussed in this thesis.

1.2. OBJECTIVES AND RESEARCH QUESTIONS

THE aim of this dissertation is to investigate and improve the performance of low-cost GNSS equipment for high precision applications. Of particular interest are cost-efficient single- and dual-frequency receivers and antennas. Central in the current approach is to experimentally quantify the trade-offs implicated by using the low-cost devices for meteorological and positioning purposes and to develop and implement ways to enhance their performance. Specifically, the following research questions are addressed:

Can single-frequency GNSS receivers be used to accurately measure water vapor in the atmosphere and to what extent does the hardware and the Satellite-specific Epoch-differenced Ionospheric Delay (SEID) model affect the outcome?

A first experimental setup consisting of one geodetic quality dual-frequency reference station (IGS station DLF1) and two co-located single-frequency receivers with different antennas is created to investigate their potential for water vapor monitoring. A network of dual-frequency stations is selected to act as SEID reference stations, with

minimum distances of 80 km to represent situations with low GNSS coverage, where application of low-cost devices is particularly beneficial. By comparing the output to existing reference datasets and dual-frequency stations, the impact and errors introduced by the low-cost receiver and by utilizing the chosen SEID model in relation to the distance to the outside network stations on the water vapor estimations is quantified. A second experiment is conducted that splits the antenna signal of a calibrated geodetic-grate antenna to dual- and low-cost single-frequency receivers. This allowed assessing the accuracy of the sensor hardware.

What is the quality of Zenith Tropospheric Delay (ZTD) estimations using a low-cost dual-frequency receiver in combination with different quality antennas in Precise Point Positioning (PPP) mode? To what degree can relative antenna calibrations improve the ZTD performance?

The release of affordable dual-frequency receivers triggers an interest of testing their performance on ZTD estimations. An important question is how the dual-frequency observations improve performance compared to low-cost single-frequency receivers and their expensive (geodetic-grade) counterparts. Additionally, the results from the previous research question indicate a strong dependency on the ZTD outcome on the receiving antenna patterns. An analysis of low-cost GNSS receiver performance in combination with a range of different quality of cost-efficient antennas is warranted. For this purpose, an experiment consisting of a series of consecutive measurement campaigns using different quality antennas and a low-cost dual-frequency receiver is conducted. The ZTD performance of each antenna is evaluated against the co-located reference station DLF1. The same experimental datasets are used for relative antenna calibrations using the known antenna pattern of station DLF1 as base. By correcting the recorded antenna datasets with the obtained antenna calibrations, the impact on the ZTD performance is assessed.

What are the effects of relative antenna calibrations on positioning solutions for low-cost antennas in combination with a low-cost dual-frequency receiver? And how can wide-spread application of relative antenna calibrations in the field be made feasible?

Positioning remains the major asset and main application of GNSS. Inspired by the results on ZTD estimations of low-cost antennas with self-derived antenna calibrations, the question arose as to the impact on positioning performance. By analyzing the kinematic positioning solutions with and without antenna calibrations over a known baseline, the positioning repeatability and offsets are analyzed. For this purpose, the datasets from the previous low-cost dual-frequency receiver and antenna experiment are used. Quantifying the effects caused by the antenna design on the positioning repeatability and the corresponding offsets is an essential step towards using low-cost antennas operationally. By releasing the calibration tool as an online web-service, wide-spread application of low-cost positioning solutions is made possible.

1.3. OUTLINE

THE contents presented in this dissertation are based on a review chapter and three journal articles. Each of them is self-contained and some overlap between them may be present.

Chapter 2 presents a review on the atmosphere, GNSS positioning, GNSS meteorology and ionosphere modeling. In chapter 3, an experiment in mid-latitude region on water vapor estimation with low-cost single-frequency receivers is presented. With data collected from 3 months to 1 year, the feasibility of single-frequency receivers for water vapor estimations is investigated. By utilizing different outside networks to model the ionosphere, the station distances dependence is analyzed. Chapter 4 shows the ZTD estimation performance with a recently released low-cost dual-frequency receiver and different quality antennas in PPP. The estimation precision is increased by applying a relative antenna calibration on the input data. The antenna calibration method is further developed and its impact on the positioning performance is analyzed in further detail in chapter 5. Finally, overall conclusions and recommendations for future research are given in chapter 6.

REFERENCES

[1] T. Haiden, M. J. Rodwell, D. S. Richardson, A. Okagaki, T. Robinson, and T. Hewson, *Intercomparison of Global Model Precipitation Forecast Skill in 2010/11 Using the SEEPS Score,* Monthly Weather Review **140**, 2720 (2012).

[2] M. B. Sylla, F. Giorgi, E. Coppola, and L. Mariotti, *Uncertainties in daily rainfall over Africa: assessment of gridded observation products and evaluation of a regional climate model simulation,* International Journal of Climatology **33**, 1805 (2012).

[3] M. Oigawa, T. Tsuda, H. Seko, Y. Shoji, and E. Realini, *Data assimilation experiment of precipitable water vapor observed by a hyper-dense GNSS receiver network using a nested NHM-LETKF system,* Earth, Planets and Space **70**, 1 (2018).

[4] S. Barindelli, E. Realini, G. Venuti, A. Fermi, and A. Gatti, *Detection of water vapor time variations associated with heavy rain in northern Italy by geodetic and low-cost GNSS receivers,* Earth, Planets and Space **70**, 28 (2018).

2

GNSS METEOROLOGY

This chapter has been used as a part of the report for the Go-No-Go procedure at Delft University of Technology (2017).

2.1. WATER VAPOR IN THE ATMOSPHERE

WATER in its solid, liquid or gaseous state is indispensable for life on Earth. In its evaporated state, water vapor plays an important role for atmospheric processes. It is the most abundant greenhouse gas in the air [1] and is spatially and temporally highly variable [2]. Atmospheric water vapor is essential for convection in the lower atmosphere and hence crucial for the generation of clouds and rainfall. With regard to a warming climate, the amount of water vapor in the atmosphere increases and causes additional absorption of long-wave radiation and reflects it back to the ground [3]. Consequently, the distribution of atmospheric water vapor is an important factor for climate models and its monitoring is crucial for climate research.

For meteorological applications, the amount of water vapor in a defined column of air is of special interest. The total atmospheric water vapor in a vertical column of air is defined as Precipitable Water Vapor (PWV) or Integrated Water Vapor (IWV). The capability of water vapor to transport moisture and latent heat in the atmosphere makes it an important factor for the weather and climate [4]. In this context, the measurements are applied in many ways such as weather forecasting and climate models. Field *et al.* [5] and Stocker *et al.* [6] state that severe weather events occur more and more frequently. A relationship with water vapor fields in the air and extreme rainfall has been observed e.g. by Seko *et al.* [7].

One approach to determine PWV is to exploit the signal delay from Global Navigation Satellite System (GNSS) transmitted signals. Recent studies conducted e.g. by Brenot *et al.* [8] demonstrate that GNSS is capable and beneficial for the monitoring of severe weather events. Currently, globally distributed networks of GNSS multi-frequency receivers are used for this purpose. They typically receive signals on at least two frequencies (L_1: 1575.42 MHz and L_2: 1227.60 MHz).

To understand the propagation of satellite signals through the atmosphere, the structure of the atmosphere itself must be defined. The atmosphere is a gaseous mixture that surrounds the earth and is prevented by gravitation from leaking into space. It consists of several layers that are separated based on their physical properties. Figure 1 shows the structure of the neutral atmosphere and the ionosphere with respect to altitude, temperature and plasma density (number of electrons per cubic centimeter).

Based on temperature characteristics, the atmosphere is divided into the troposphere (ranging from the surface to 9 km at the poles and up to 16 km at the equator), the stratosphere (until about 50 km), the mesosphere (unto about 85 km) and the thermosphere (>85 km). Bearing in mind Fermat's principle that out of all possible paths an electromagnetic wave may take, it takes the path with the shortest travel time, the refraction properties of particles in the atmosphere are of special interest. Relevant to this characteristics are tropospheric and an ionospheric components of the atmosphere. Regarding the refraction characteristic the troposphere is referred to as the combination of the troposphere and the stratosphere which then ranges until approximately 50 km height. The ionosphere extends from about 50 km to approximately 1000 km [10]. It consists of electrically charged particles and is dispersive at 1.5 GHz. Dispersion occurs if the propagation velocity is dependent of the frequency. In a dispersive medium the refractivity depends on the frequency or wavelength. The ionizing effect of the sun's radiation on the earth's upper atmosphere produces free electrons. In the ionosphere layer the amount of

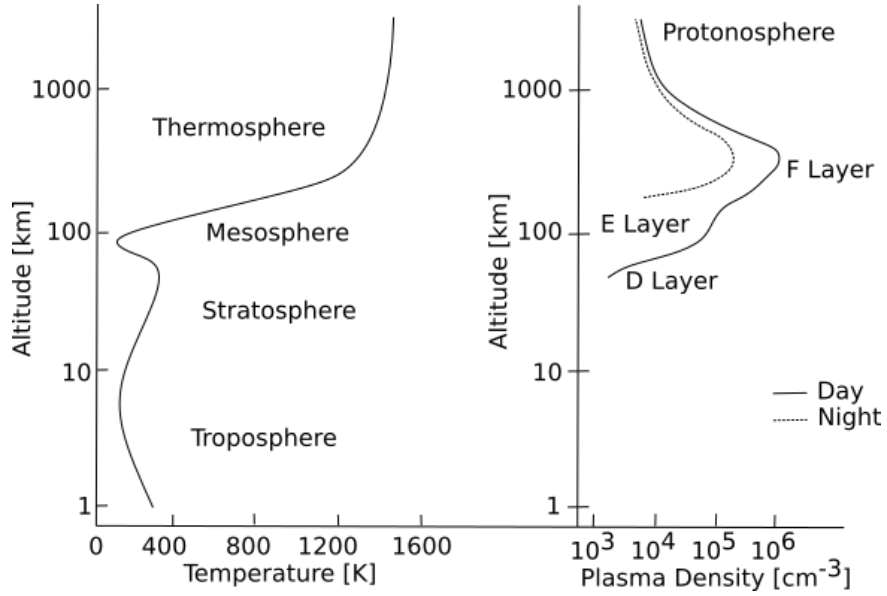

Figure 2.1: Structure of the neutral atmosphere and the ionosphere after Bauer [9]

these free electrons affects the propagation of electromagnetic waves. This region consists of plasma containing the charged particles. The free electrons in the lower boundary of the ionosphere can only exist for a short time until they are captured by positive ions and atoms are recombined. The refractive index depends on the electron density and the frequency of the electromagnetic signal traveling through it. The diversity of the ionosphere varies as a function of time of the day. It is categorized in several layers, namely the D, E and F layers. The recombination is high in the D-layer and almost complete deionization is reached during nighttime from about 50 to 90 km caused by the high particle and low electron density. The E-layer (90-150 km) is influenced by X-rays (1-10 nm) and far ultraviolet solar radiation ionization of molecular oxygen. During nighttime it is affected by cosmic rails and meteors [4]. The F-layer (150-1000 km), also known as the Appleton layer, splits into two layers F1 (150-200 km) and F2 (200-1000 km) where the F1 layer merges into the F2 layer at night. The solar radiation ionizes atomic oxygen and its ionization reaches its peak at around noon and decreases towards the sunset. Extreme ultraviolet solar radiation and coronal mass ejections strongly disturb the earth's magnetic field and cause geomagnetic storms which cause radio and radar scintillation. Strong magnetic regions on the sun (sunspots) generally quantify the solar activity and shows an 11-year variation cycle.

Unlike the ionosphere, the troposphere is non-dispersive for frequencies below 30 GHz. The propagation is frequency independent and the excess group delay caused by this region is constant. At higher radio frequencies, water vapor and molecular oxygen will have an effect on radio observations. The phase velocity will differ from the group velocity and a frequency dependent propagation delay can be observed. The troposphere consists of up to 99% of the total amount of water vapor. Based on 15 radiosonde

launches in a summer period, Sato *et al.* [11] observed 99% of the total accumulated water vapor between 8 and 9 km altitude. Most of the water vapor is in the boundary layer, the lowest 2 km of the atmosphere. The amount of water vapor varies widely, both temporally and spatially. It plays a significant role from global climate to micrometeorology. With regard to the tropospheric refraction index, the magnitude of rain, fog and cloud attenuation is negligible for L-band frequencies.

2.2. TECHNIQUES FOR MEASURING ATMOSPHERIC WATER VAPOR

SEVERAL techniques exist to observe the water vapor content in the atmosphere and were highlighted e.g. by Bevis *et al.* [12]. The traditional method to measure the PWV in the air is by releasing radiosonde balloons. A radiosonde consists of a small instrument package that is suspended below a balloon inflated with helium or hydrogen for updraft. The balloon may rise at a rate of 300 meters per minute unto an altitude of about 28 km and transmits in-situ measurements of temperature, pressure and humidity to the ground station. Through an equipped GPS sensor, strength and direction of the wind can also be obtained. During the ascension a vertical profile of the weather parameters is produced. IWV in $\frac{kg}{m^2}$ is then estimated from the integral of the mean density of water vapor at defined height intervals.

$$IWV = \int_{h1}^{h2} \rho_v dh = \sum_{i=1}^{n} \rho_{d,i} r_i \Delta h_i$$

Where ρ_v is the mean density of water vapor for each layer in $\frac{kg}{m^3}$, dh the height difference of each layer of the atmosphere, ρ_d the dry air density in $\frac{kg}{m^3}$, r the mixing ratio and Δh_i the altitude steps in meter. The dry air density may be expressed as

$$\rho_d = \frac{P}{R_d T}$$

With P the air pressure in Pa, R_d the specific gas constant for dry air ($287.058\, J\, kg^{-1}\, K^{-1}$) and T the observed temperature in K. The mixing ratio r is a dimensionless ratio of the water vapor mass to the mass of dry air:

$$r = 0.622 \frac{e}{P - e}$$

Where e is the vapor pressure and P the air pressure. With the relative humidity (RH) measurements from the radiosonde the vapor pressure may be computed:

$$e = \frac{RH \cdot e_{sat}}{100}$$

$$e_{sat} = 6.112[Pa] \cdot exp(\frac{17.62T}{243.12 + T})$$

With e_{sat} the saturation vapor pressure and T the temperature in degree Celsius. The mean partial pressure of water vapor is defined as a function of the mean relative humidity and temperature. The relationship between IWV and PWV in mm is defined as

$$PWV = \frac{IWV}{\rho}$$

with ρ defined as the density of liquid water. Caused by the drift of the balloon, the observed profile does not correspond exactly to the profile at the launch site. Ice contamination may further lead to inaccuracies of the humidity measurements. Despite the coarse temporal and spatial resolution the measurements contain valuable information of the atmospheric state. However, driven by practical and economical reasons, only a few launches are typically performed per week. In the whole Netherlands, only one radiosonde launch is performed every 12-24 hours.

Using space- or ground based Water Vapor Radiometers (WVRs) is another method to estimate PWV. They generally operate on the two frequencies 20.6 GHz and 31.6 GHz [13]. The lower frequency is close to the water vapor absorption line at 22.2 GHz. The brightness temperature (measurement of the radiance of microwave radiation traveling from the atmosphere top to the satellite) is the fundamental parameter obtained by passive microwave radiometers. It responds primarily to vapor whereas the 31.6 GHz is sensitive to liquid. The raw antenna counts are calibrated to obtain the brightness temperature. Driven by the characteristics of gases and liquid, wavelengths of about 1 cm and below are suitable to measure temperature, vapor and cloud liquid. Several centimeters wavelengths are required to observe heavy rain. However, this condition also makes the measurements less accurate during medium and heavy rainfall. The coefficients required to estimate PWV are derived by a-priori statistics from e.g. radiosonde profiles. Liquid water also emits radiation of similar intensity than the water vapor at the frequency of 22 GHz. However, both radiation processes have different spectral features [14] which allows to separate the liquid from the vapor contribution by using two different frequencies. Various approximations and algorithms were developed to estimate the water vapor content of the column of the observed brightness temperatures ([13] and [15]).

The down-looking, space-based WVR observes the absorption lines in the radiation from the hot background of the earth. The determination of water vapor is more complicated over land than over the ocean since the temperature of the hot background varies a lot and is difficult to determine. The same problem arises with the presence of clouds, because the background temperature changes significantly from the surface to the cloud top and is not easily specified. Even though it is possible to model these characteristics, it results in most cases in a difficult and time consuming task. As a result, they are more useful to be utilized over oceans than over land. They provide good spatial but poor temporal resolution and their use is limited by cloud cover. The Global Microwave Imager (GMI) on the Global Precipitation Measurement (GPM) mission, lauched on February 27 2014, has a mean footprint resolution between 15 and 12 km at the frequencies 19 GHz and 31-47 GHz [16]. In these frequencies the instrument covers a swath of about 931 km on the Earth's surface. Also on board is the Advanced Microwave Scanning Radiometer 2 (AMSR2) which covers a swath of 1450 km with a resolution between 22 and 12 km at 19

GHz and 31-37 GHz.

An upward-looking, ground based WVR measures the background radiation of water vapor in contrast to the cold background from space. It is capable to estimate the IWV along the line of sight. It also measures the sky brightness temperature using two or more frequencies which allows to simultaneously estimate IWV and even integrated liquid water [17]. The measurements are not affected by light cloud cover, and continuous slant measurements can be achieved. A major disadvantage of the WVR is the poor performance in heavy cloud or rainy conditions [12]. Validation studies conducted by Ware *et al.* [18] and Braun and Rocken [19] found an almost constant IWV error of approximately 1.3 kg per m² independent of the total amount of water vapor in the atmosphere. The relative error is more significant during dry periods (~20%), than during wet conditions (~2%).

Satellite-based infrared radiation measurements can also monitor the water vapor. Water vapor emits radiation in the 6.7 μm infrared wavelength. However, studies conducted by Gutman and Benjamin [20] and Elliott [21] state that they are only reliable in cloud-free conditions. Whereas other methods integrate the amount of water vapor along the propagation path, satellite acquired infrared water vapor images only detect upper-level and middle layer water vapor. A humid upper layer will prevent the detection of water vapor below this layer. Vice-versa, a dry upper layer allows to detect moisture in the middle layer. Since there is usually sufficient moisture in these layers, it is not possible to detect humidity in the lower levels. Low level clouds appear darker on an infrared image than high level clouds since the observed temperature in the troposphere decreases with height.

Very Long Baseline Interferometry (VLBI) is present in geodesy since 40 years and offers a unique technique observing extra-galactic radio sources (quasars). Only a few antennas exist on the globe resulting in intercontinental baselines. The measurements are characterized by very high quality and contribute significantly to the realization of the International Terrestrial Reference System (ITRS). The technique measures the time differences in the arrival of the emitted microwave signals at two or more VLBI antennas (typically in the S-band: 2.3 GHz and X-band: 8.4 GHz). By correlating the phase samples of various frequency channels and times, the phase delay, phase delay rate, group delay and amplitude are produced [22]. Similar to high precision satellite positioning, models of physical properties must be considered (e.g. tectonic motions, solid earth tides, alterations caused by local geological and hydrological processes, ...). Ionospheric effects are eliminated by using signals on two frequencies. However the contribution of the neutral atmosphere (troposphere) remains a major error source. VLBI is able to determine the integrated properties of the atmosphere and thus also water vapor.

Utilizing microwave imaging systems like the Interferometric Synthetic Aperture Radar Interferometry (InSAR) is another possibility to estimate temporal water vapor changes in the atmosphere. Contrary to the infrared systems, it has cloud penetrating capabilities. Recent studies have demonstrated that InSAR is capable to derive PWV spatial distributions. The spatial resolution depends on the pixel size of the data used for the analysis. Using the European Remote Sensing (ERS) satellites images, a spatial resolution of e.g. 20 m is possible [23]. Typically, InSAR has been used to derive digital elevation models (DEMs) or precise surface deformations. However, their accuracy is

limited by the tropospheric delay caused by the water vapor content in the atmosphere [24]. Two not simultaneously taken SAR images are affected differently by the atmosphere. Two microwave images from almost the same position are acquired at different epochs. By using a digital terrain model the geometric path length differences are removed and a differential interferogram is formed. Since the interferometric pairs are recorded within a short time interval, the remaining phase delay is assumed to only be related to the atmospheric propagation delay. The terrain deformations are neglected which leads to an almost proportional phase delay to the integrated water vapor along the propagation path.

Another approach to determine atmospheric water vapor is to exploit the signal delay from Global Navigation Satellite System (GNSS) transmitted signals. GNSS is mostly known for their positioning and navigation purposes but apart from this it is also a valuable and established tool for atmospheric sounding. In the past, geodesists treated the delay caused by the atmosphere as an error which needed to be removed from the data. During error investigations Davis *et al.* [25] found that the observed signal delay can be used for water vapor estimation. Bevis *et al.* [12] proposed to use dual-frequency receivers on the ground to obtain the signal delay and thus the water vapor along the signal path from the satellite to the receiver. Whilst commonly used radiosondes have a poor temporal resolution (typically every 6 or 12 hours), using GNSS, it is possible to continuously monitor PWV in the atmosphere with a high temporal resolution. Contrary to microwave radiometers, the method does not require additional calibrations and is not affected by meteorological conditions. The potential of GNSS using ground based receivers to derive PWV has been demonstrated and validated by several case studies (e.g. [12, 26–28]). GNSS can also be used for a technique called Radio Occultation (RO) to monitor the atmosphere. The GNSS satellite radio signals from low elevation angles are observed at a Low Earth Orbit (LEO) satellite. During a GNSS occultation a LEO satellite receives signals while it rise or sets behind the Earth's limb. The received signal is bent by the atmosphere depending on its density. This bending causes a longer travel time of the signal and together with the bending angle the atmospheric density can be obtained. The observed change in delay includes the effect of the atmosphere which refracts and bends its path. The data may be used to estimate temperature, pressure, humidity in the neutral atmosphere and electron density in the ionosphere. At microwave wavelengths, the refractivity is dependent of the pressure, temperature, moisture, ionosphere and scattering by liquid water and ice [29]:

$$N = 77.6\frac{P}{T} + 3.73 \cdot 10^5 \frac{P_w}{T^2} - 40.3 \cdot 10^6 \frac{n_e}{f^2} + 1.4W$$

Where N is the refractivity, P the atmospheric pressure in mbar, T the atmospheric temperature in Kelvin, P_w the water vapor partial pressure in mbar, n_e the electron number density per cubic meter, f the transmitter frequency in Hertz and W the liquid water content in grams per cubic meter. Since the contribution to the path delay caused by (ice and) liquid water are very small, this effect is neglected. With this technique, the electron density above 60 km and the neutral atmosphere from about 6 km to 70 km height is observed. Together with a boundary condition of pressure at a certain height, profiles of the pressure, temperature and geopotential heights may be observed in the

middle atmosphere. Below 6 km the water vapor concentration generally increases and contributes up to 30% to the net refractivity. To extract water vapor directly from the RO vertical profile, knowledge of temperature derived from climatology, independent observations or weather analyses is required. For this purpose the dry part can be subtracted from the total refractivity or derived by a (1D) variational method which combines the refractivity with analysis temperature, water vapor profiles and surface pressure. The COSMIC (Constellation Observing System for Meteorology, Ionosphere, and Climate), a joint project between Taiwan and US, currently consists of 4 LEO micro-satellites (originally 6) was launched in 2006 and provides daily 800 - 900 RO profiles. This method uses one or more receivers on a Low Earth Orbit (LEO) satellite. Using GPS RO, vertical profiles (with about 200 m vertical resolution) of atmospheric parameters like temperature and water vapor on a global scale can be obtained. Since the RO technique is based on time delays, and the raw measurements are not based on a physical device that deteriorates with time, no instrument drift or bias is present and hence no calibration is required. It allows to obtain a high vertical resolution with high accuracy [30, 31].

2.3. GNSS SIGNAL PROCESSING

GNSS is a generic term for existing and future satellite systems such as GPS, GLONASS, BeiDou and Galileo. It is a space-based system providing global coverage of geospatial positioning, navigation and time measurements by receiving signals transmitted by orbiting satellites. All GNSS use carriers in the L Band (ranging from 1 to 2 GHz). GPS transmits data in the L1 band (1575.42MHz), L2 (1227.60MHz) and L5 (1176.45MHz). Since each satellite transmits its signals through the atmosphere on the same frequencies in the L-band, interference between the signals of different satellites on the same carrier frequency must be avoided by the signal design. Each GPS satellite transmits a satellite-specific Pseudo-Random Noise (PRN) code which is used for satellite identification and is independent from the transmitted data. In order to distinguish simultaneous incoming signals, GPS uses Code Division Multiple Access (CDMA). This technique allows to extract the desired signal while rejecting all other sources as random noise. CDMA divides each bit into short intervals (chips). Transmitting 1 information bit requires to send its chip sequence. Each bit is therefore multiplied with the chip code data stream. The data stream is modulated onto a carrier and the overall signal is spread over a wider bandwidth compared to the original data. To decode the data, the receiver first demodulates the CDMA signal from the carrier. Together with the spreading code the original data is recovered. With the CDMA technique it is possible to transmit several sets of data independently on the same carrier and recover them without interference by other signals. The instrumental accuracy of measurements is up to 1% of the chip length. It depends on the utilized code type and is in the order of decimeters. The carrier phase measurements whereas is better than 1% of the wavelength and in the order of 1.5 mm. Modulated onto the carrier frequencies are information, such as the satellite-specific PRN, satellite time and orbit parameters, used to calculate the satellite position in the orbit and auxiliary data like the satellite clock correction. A more in-depth description of the signal multiplexing and data processing is described by Hofmann-Wellenhof *et al.* [4].

Each receiver is equipped with an antenna which detects the electromagnetic waves

sent by the satellites and converts the wave energy into an electric current. Since the incoming GNSS signals are very weak, the antenna must be very sensitive and before directing the signal to the receiver electronics, the signal strength is typically amplified. The receiver handles signal filtering to ensure low noise and to reject out-of-band interference. The incoming signal is down-converted to a lower frequency. For this purpose, the incoming radio frequency signal is combined with a sinusoidal signal generated by a local oscillator (generally based on a less expensive quartz crystal). Whilst the carrier frequency is lower, the new frequency contains still all data from the original signal. Because the oscillator does not provide the same stability as the atomic clocks in the satellites, the time offset is estimated as a fourth unknown in the observation equations. The receiver compares the modified satellite signal carrier phase with a copy generated by receiver itself. All signals coming from all visible satellites are isolated and identified by their known PRN code. The pseudorange is calculated by scaling the transmission time of the signal to the receiver. It is called pseudorange because it does not match with the satellite-receiver euclidean distance due to e.g. the clock errors. Beside the code measurement (from the code replica generated by the receiver), the carrier is reconstructed. Different techniques exist for this task. The carrier-phase observable is the difference between the satellite transmitted and the Doppler-shifted carrier phase. The observable is off by an unknown integer number of cycles which can be added to the observable. Since the ambiguity and other parameters are linearly dependent, ambiguity fixing is not a trivial problem [32]. Either the parameters are eliminated by forming differences or carefully treated in the parameter estimation. The signal is not traveling through vacuum and is refracted and delayed by the atmosphere. For the code measurement the following observation equation is used:

$$P_r^s = \rho_r^s + (\delta t_r - \delta t^s) \cdot c + \delta_{r,ion}^s + \delta_{r,tropo}^s + \xi$$

where c is the speed of light, the subscripts r and s denote the receiver and satellite, ρ the geometric range, δt_r and δt^s the receiver and satellite clock offsets, $\delta_{r,ion}^s$ the ionospheric correction, $\delta_{r,tropo}^s$the tropospheric correction and ξ remaining error sources (e.g. multipath, relativity, hardware biases and measurement noise). Utilizing the phase difference between receiver carrier wave and the the one generated by the local oscillator yields the carrier phase measurement in units of length:

$$L_r^s = \lambda \cdot \phi = \rho_r^s + c \cdot (\delta t_r - \delta t^s) + \lambda \cdot N_r^s - \delta_{r,ion}^s + \delta_{r,trop}^s + \xi$$

where λ denotes the carrier wavelength and N_r^s the initial carrier phase ambiguity. The opposite sign of the ionospheric correction is caused by the time delay caused by the group velocity of the code sequence and by the phase velocity in the ionosphere.

The general principle to estimate the three-dimensional receiver position is determined by resection (intersection of i.e. three spheres defined by three different pseudoranges). Since the receiver clock and the satellite clocks are not running synchronously, an additional fourth satellite is required to estimate the error between the receiver and satellite clocks. Geometrically, this is realized by a sphere that is tangent to the four spheres defined by the pseudoranges. Further satellite ranges are used as an overdetermination to improve the receiver position. Removing satellites with low elevation

angles typically improves the positioning solution, because of the greater distortions caused by the atmospheric impacts [4].

The basic GNSS observables can be used to create combined signals. There exist an infinite number of linear combinations. One example is the ionosphere-free combination L_{IF} which removes the first order (up to 99.9%) of the ionospheric effect. The first order ionospheric effect on the code propagation is of the same order as the carrier phase propagation error but has the opposite sign.

$$L_{IF} = \frac{1}{f_1^2 - f_2^2}(f_1^2 L_1 - f_2^2 L_2)$$

$$L_{IF} = \rho + c \cdot (dt_r - dt^s) + \frac{c \cdot f_1 \cdot N_1 - c \cdot f_2 \cdot N_2}{f_1^2 - f_2^2} + T + \varepsilon_{L_{IF}}$$

where T is the ionosphere-free combination of the tropospheric error on the two frequencies and $\varepsilon_{L_{IF}}$ is the combination of their residual errors. The L_{IF} combination eliminates the first-order ionospheric delay on the observables. Unfortunately, the noise is increased by about a factor of three and ambiguities cannot be directly solved as integers [33]. Similarly, a combination may be formed to isolate the ionosphere, also known as the geometry-free linear combination:

$$L_4 = L_1 - L_2 = -\xi_4 I + \lambda_1 N_1 - \lambda_2 N_2$$

$$\xi_4 = 1 - \frac{f_1^2}{f_2^2}$$

This eliminates the geometric term including the clock offsets and tropospheric delay. In pre-processing it is often used together with the wide-lane linear combination to detect cycle slips [34]. To achieve high precision positioning, carrier phase measurements are used and all error sources of the signal must be accounted for. If two receiving antennas are processed together and are close to each other (short baseline), many common errors are eliminated by differencing. Over short baselines (few kilometers) the ionospheric and tropospheric delay will be almost canceled because the received signals from the observed satellites are almost identical. In particular, this is used for the satellite and receiver clock errors. With this technique, only the differences between the biases remain [33].

One distinguishes between Single Differences (SD) and Double Differences (DD). Four observations can be retrieved from two receivers and two satellites. SDs can be formed between two satellites, two receivers or two epochs. In geodesy single-differences are usually formed between the simultaneous code or phase observations from two receivers to the same satellite. This eliminates the common satellite clock error. The corresponding code and phase SD observation equations write:

$$\Delta P_{ij}^p = P_i^p - P_j^p = \Delta\rho_{ij}^p + c \cdot \Delta\delta t_{ij} + \Delta I_{ij}^p + \Delta T_{ij}^p + \varepsilon_{P,ij}^p$$

$$\Delta L_{ij}^p = L_i^p - L_j^p = \Delta\rho_{ij}^p + c \cdot \Delta\delta t_{ij} - \Delta I_{ij}^p + \Delta T_{ij}^p + \lambda \cdot \Delta N_{ij}^p + \varepsilon_{L,ij}^p$$

P and L are the code and phase observations in units of length, ρ the range from the receiver to the satellite, c the speed of light in the vacuum, δt the receiver clock, I the ionospheric, T the tropospheric and ε the multipath and receiver noise errors. λ denotes the wavelength and N the ambiguity. The superscript p denotes the satellite, the subscripts i and j the receivers. The code and phase SD between one receiver and two satellites p and q writes:

$$\nabla P_i^{pq} = P_i^p - P_i^q = \nabla\rho_i^{pq} + c\cdot\nabla\delta t^{pq} + \nabla I_i^{pq} + \nabla T_i^{pq} + \varepsilon_{L,i}^{pq}$$

$$\nabla L_i^{pq} = L_i^p - L_i^q = \nabla\rho_i^{pq} + c\cdot\nabla\delta t^{pq} - \nabla I_i^{pq} + \nabla T_i^{pq} + \lambda\nabla N_i^{pq} + \varepsilon_{L,i}^{pq}$$

This SD cancels the receiver clock term. The DD approach eliminates satellite and receiver clock errors. DDs are constructed by further differencing between receivers:

$$\nabla\Delta P_{ij}^{pq} = \Delta P_{ij}^p - \Delta P_{ij}^q = \nabla\Delta\rho_{ij}^{pq} + \nabla\Delta I_{ij}^{pq} + \nabla\Delta T_{ij}^{pq} + \varepsilon_{L,ij}^{pq}$$

$$\nabla\Delta L_{ij}^{pq} = \Delta L_{ij}^p - \Delta L_{ij}^q = \nabla\Delta\rho_{ij}^{pq} - \nabla\Delta I_{ij}^{pq} + \nabla\Delta T_{ij}^{pq} + \lambda\cdot\nabla\Delta N_{ij}^{pq} + \varepsilon_{L,ij}^{pq}$$

Being able to fix the carrier phase ambiguities to integers, DD is a common technique used for high precision positioning. In short-baseline Real Time Kinematics (RTK) processing (about 10 km baseline length), centimeter level accuracy positioning can be achieved in real time. Errors caused by orbit, ionospheric and tropospheric signal refraction are distance dependent and increase with the length of the baseline. By applying area corrections from surrounding reference stations the reference spacing may be extended up to 70-100 km [32]. One RTK network solution is based on a Virtual Reference Station (VRS) [35]. This virtual station can be used for fast static or RTK processing. It enables to reduce the baseline distance between rover and reference station. It makes use of corrections from the reference network and help to remove spatially correlated errors. At least three reference stations are required which are continuously processed in real-time with an ambiguity-fixed solution at a control center. However, the rover needs to transmit its position to the control center which in turn generates the VRS coordinates and sends the corrections back to the rover.

2.4. PRECISE POINT POSITIONING

Precise Point Positioning (PPP) primarily relies on un-differenced carrier phase observations from a singular receiver [36]. It allows processing a large number of stations simultaneously respecting the high precision requirements of geodetic applications. Nowadays it has become a popular strategy to estimate positions and atmospheric parameters. Contrary to the differential processing, PPP requires no reference stations directly. Instead, un-differenced phase and pseudorange observations from a single receiver are utilized. Using undifferenced observations, all biases and nuisance parameters are explicitly included in the observation equation. Errors such as the receiver and satellite clock errors do not cancel with this method. To eliminate the first order ionospheric delay effects, measurements on at least two different frequencies are required to form the ionosphere-free linear combination. In order to use PPP if data on only one frequency is

available, the data must be corrected for the ionospheric influence. Most existing ionosphere models are developed for large regions and are not able to represent rapid and small scale ionospheric fluctuations [37]. Even though alternative approaches were designed [38, 39], the processing requires special analysis software. Deng *et al.* [40] developed the Satellite specific Epoch-differenced Ionospheric Delay (SEID) model, which is independent from the GNSS software packages. The method generates a L2 observable by using a network of surrounding dual-frequency receivers. This approach allows to apply the ionosphere-free linear combination and process the dataset with existing geodetic processing software in PPP mode (see also Chapter 3 or [40] and [41]).

To account for other effects that introduce errors to the signal length, PPP makes use of detailed physical models whilst other parameters are estimated. Without proper modeling of these corrections, the errors can exceed several meters [42]. PPP utilizes processed precise satellite orbit, clock and antenna errors provided by analysis centers (e.g. the IGS). These orbit and clock products by the IGS are a combined solution of different analysis centers from a world-wide network of GNSS stations. Each analysis center uses different processing engines for the orbit and clock estimation. Some tracking stations are equipped with atomic clocks (rubidium, cesium, ...) for their local oscillator and can separate between the station's clock and orbit error.

The measurements obtained by the receiver refer to the satellite antenna phase center. Using the precise IGS satellite coordinates and clock products, phase center offsets must be applied to the specific satellite orbits in space since the data refers to the corresponding satellite center of mass. Another effect is caused by the rotation of the satellite along its own axis. The so called phase wind up is caused by the reorientation of the satellite towards the sun of its solar panels and affects only the transmitted carrier-phase data. Since the satellites and receivers are moving with respect to each other and are in different gravitational fields, the observations must be corrected for relativistic effects. Other errors are caused by the movements of the station caused by gravitational forces. The "solid" Earth responds to the lunisolar gravitational forces which generate the ocean tides. The modeled effect can reach up to 30 cm and consists of a latitude dependent permanent displacement and a periodic part with changing semi-diurnal and diurnal amplitudes [43]. Similar to the deformations caused by the gravitational forces of the sun and the moon, the Earth is also subject to changes of its spin axis with regard to the defined reference system. Different to the solid earth tides, the corrections are not averaged over a 24 hour period. The polar motion may cause up to 25 mm height and 7 mm horizontal displacement. Another error source the ocean loading. Even though this effect is very localized, it needs to be taken into account for tropospheric estimations, except the station is far away from the nearest coast (> 1000 km).

The receiver antenna is also a source of error. Equivalent to the satellite antenna, the receiver antenna phase center is not only different to the center of mass, but also frequency dependent. For each considered frequency, antenna corrections include a Phase Center Offset (PCO) and Phase Center Variations (PCVs). PCVs are expressed as a function of the elevation- and azimuth angles of the incoming satellite signal while PCOs are local coordinates originating at the Antenna Reference Point (ARP). The ARP is defined as the center of the intersection point between the vertical axis and the ground of the antenna. The receiver antenna is also subject to multipath (e.g. near-field effects). This

effect can cause positional changes, but may also cause the receiver to lose the phase lock and cycle slips can occur. For static antennas, the multipath is mainly dependent on the azimuth and elevation of the observed satellite. This effect repeats with the periodicity of the satellite orbits. Therefore, e.g. for GPS satellites the same delay is observed every 23 hours and 56 minutes. By stacking the daily residuals, the multipath effects can be estimated and separated from the slant delay caused by atmospheric impacts [44].

Specifically for PPP or long baselines, the atmosphere causes errors to the satellite propagation time. Since first-order ionospheric delays are eliminated by using the ionosphere-free linear combination, the lower part of the atmosphere, the troposphere, remains as a major atmospheric influence. The troposphere is a mixture of dry gases and water vapor that affects the propagation of the signals. It consists of about 80% of the atmosphere's mass and is that part of the atmosphere where the weather, i.e. clouds, rain, snow, etc. takes place [2]. The molecules and atoms in this layer are mostly neutral and accordingly non-dispersive up to a frequency of about 30 GHz. The GNSS signals transmitted on different frequencies are thus affected by the troposphere in the same way and no combinations of the observations can eliminate the effect of the tropospheric refraction. The following section describes how the tropospheric delay can be used to estimated the amount of water vapor in the atmosphere.

2.5. DERIVING PWV FROM GNSS SIGNAL DELAYS

THE study by Davis *et al.* [25] proposed to separate the lower part of the signal delay, the tropospheric component, into a hydrostatic (dry) and a non-hydrostatic (wet) delay. In order to mitigate these effects, models can be used. The dry component accounts for about 90% of the total tropospheric delay and is caused by different atmospheric gases like oxygen, carbon dioxide and nitrogen. The wet delay is determined by the water vapor in the atmosphere and depends on the atmospheric conditions. It influences the refractivity by up to 30%. Bevis *et al.* [12] demonstrate how surface temperature and pressure measurements can be used to convert the tropospheric wet delay from GPS measurements to derive integrated water vapor observations overlying the receiver. The total tropospheric delay (here referred as: Δ^{Trop}) along the refracted path s can be calculated as the difference between the bent ray path and the geometric distance [10]:

$$\Delta^{Trop} = \int (n-1)ds = 10^{-6} \int N ds \tag{2.1}$$

Where n is the refractive index of air and N the refractivity along the propagation path. Both are dimensionless numbers. According to [45], the refractivity in the troposphere can be considered as the sum of a dry (hydrostatic) and a wet component which can be related to the atmospheric temperature and partial pressure of water vapor and dry gases:

$$N = N_{dry} + N_{wet} = k_1 \frac{p_d}{T} + k_2 \frac{e}{T} + k_3 \frac{e}{T^2} \tag{2.2}$$

The first term on the right side accounts for the dry part and the last two terms for the wet part. p_d is the combined partial pressure of the dry gases in mbar, T the

temperature in degree Kelvin and e the partial pressure of water vapor in mbar. $k_1 = (77.604 \pm 0.0014)\frac{K}{mbar}$, $k_2 = (64.79 \pm 0.08)\frac{K}{mbar}$ and $k_3 = (3.776 \pm 0.004)\frac{10^5 K^2}{mbar}$ are empirical constants determined by Thayer [45]. The integral of refractivity N (eq. 2.2) in the zenith direction is referred to as the Zenith Tropospheric Delay (ZTD), which is in turn expressed as the sum of the Zenith Hydrostatic Delay (ZHD) and Zenith Wet Delay (ZWD). The ZHD can be estimated using e.g. the Saastamoinen or Hopfield model. Saastamoinen [46] defines the ZHD in meters as:

$$ZHD = \frac{0.0022768 P_0}{1 - 0.00266 cos(2\Phi) - 0.00028 H} \tag{2.3}$$

Where P_0 is the total atmospheric pressure in mbar, expected to be observed at the observation point, Φ is the latitude in radians and H the height above the reference ellipsoid in kilometers. Given good surface pressure measurements (±1mbar), the ZHD can be estimated with a few millimeters accuracy [20]. ZWD can be derived from the GNSS estimated ZTD by removing the ZHD component (e.g. from equ. 2.3):

$$ZWD = ZTD - ZHD \tag{2.4}$$

The approach to estimate the non-hydrostatic delay by taking the difference between ZTD and ZHD is preferred since the wet delay is much more variable than the hydrostatic delay and its predictive value is poor in comparison to the ZHD estimation [12]. 90% of the total delay is attributed to the dry (hydrostatic) and 10% to the wet (non-hydrostatic) delay [47]. Using parameters of a standard atmosphere, the Saastamoinen tropospheric zenith delay results in approximately 2.3 meters [4]. The ZWD can be close to zero in arid regions and up to 35 cm in humid regions. Using the ZWD, the PWV can be estimated with a non-dimensional ratio (Π) defined as:

$$\Pi = \frac{10^6}{\rho R_v \left[\left(\frac{k_3}{T_m}\right) + k_2'\right]} \tag{2.5}$$

Where ρ is the density of liquid water, R_v the specific gas constant for water vapor and T_m the weighted mean temperature along the propagation path.

The conversion factor Π is typically around 0.16 and varies up to 20% depending on the location, height and meteorological conditions [48]. Bevis *et al.* [12] estimate T_m and k_2' with:

$$T_m = 70.2 + 0.72 T_s \tag{2.6}$$

and

$$k_2' = k_2 - m k_1$$

Where T_s is the surface temperature in Kelvin. k_2' is represented as units of Kelvin per millibar and is composed of the earlier stated constants and the ratio of the molar masses of water vapor and of dry air. The PWV, defined as the height of the water column overlying the receiver, is then defined as $PWV = \Pi \times ZWD$. Typically, PWV values are lower in winter periods and higher in summer.

The tropospheric zenith delay is obtained by using an elevation dependent mapping function for the observed delays from the satellites at different elevations. Mapping functions provide the ratio between the delay in zenith direction and that in the slant direction and are generally a measure for the thickness of the atmosphere compared to the Earth radius. Prominent examples were developed by Davis *et al.* [25], Niell [49] and Boehm *et al.* [50]:

$$m(e) = \cfrac{1}{sin(e) + \cfrac{a}{sin(e) + \cfrac{b}{sin(e) + ...}}}$$

These mapping functions rely on the assumption of an azimuthal symmetric atmosphere. However, driven by climatic and weather phenomena the path delays are not constant with varying azimuth. Sites in northern latitudes will have a systematically larger path delay towards South because the height of the troposphere is here larger than above the poles [51]. Introducing gradients to the observation equations can geometrically be interpreted as a tilting of the mapping function. Estimating gradients is particularly important when using observations from low elevation angles. A simple model has been introduced by MacMillan [52]:

$$\Delta L(\phi, e) = \Delta L_0(e) + m(e)cot(e)[G_N cos(\phi) + G_E sin(\phi)]$$

where ΔL_0 is the isotropic delay, e the elevation angle, ϕ the azimuth, $m(e)$ the mapping function and G_N and G_E the gradient vectors in the North-South and East-West directions. Estimating the tropospheric gradients allows to cope the asymmetry of the local troposphere.

2.6. APPLICATION AND VALIDATION STUDIES

ATMOSPHERIC measurements containing information about the amount of water vapor in the air, whether obtained by radiosonde profiles, WVR, VLBI or ground- or space (RO) based GNSS measurements, are important for climate and Numerical Weather Prediction (NWP) models. It has become a standard procedure for weather agencies to assimilate GNSS data into their models. The impact on the overall performance is typically positive and has been investigated by several studies which compare the GNSS-derived atmospheric products (ZTD, STD, PWV) to NWP outputs without assimilation: e.g. de Haan [53], Haase *et al.* [54], Gendt *et al.* [55] or Bock *et al.* [56]. Every NWP model is configured differently and has own characteristics to match local requirements. GNSS meteorology is characterized by the possibility to obtain tropospheric parameters with a higher spatial and temporal resolution compared to e.g. traditional observations using radiosondes. GNSS fixed ground stations are able to track the PWV continuously under all weather conditions. Globally available long-term ZTD observations enable trend analysis and allow to optimize models used in GNSS data processing. For kinematic positioning applications, tropospheric information obtained from weather models or a network of GNSS stations can be used to reduce errors in the height component which are highly correlated to the tropospheric delays. An RMS of less than

3 mm is the desired threshold accuracy of PWV capable to be assimilated into an NWP nowcasting model [57].

2.6.1. NUMERICAL WEATHER PREDICTIONS

SEVERAL studies in Europe, North America and Asia (e.g. Gendt *et al.* 55, Gutman *et al.* 58, Vedel and Huang [59]) were performed that concluded a positive impact of GPS derived PWV estimates assimilated into numerical weather prediction models. About 250 European GNSS stations in the EUREF permanent network provide daily ZTD estimates with a 1h temporal resolution ranging from 1996 until today. More than 100 stations within the network are collocated with radiosondes and a few with VLBI radio telescopes. Several European projects were carried out in order to exploit GNSS derived signal delays for water vapor retrieval and meteorological applications. The MAGIC (Meteorological Applications of GPS Integrated Column Water Vapor Measurements in the western Mediterranean) project from 1998 to 2001 used GPS sites in France, Italy and Spain to demonstrate the value of combining the GPS network for weather forecasting applications [60]. The EC COST Action 716 lasted from 1999 to 2003 and included 15 European countries. GPS derived ZTD estimations were provided on an operational basis [61]. The TOUGH (Targeting Optimal Use of GPS Humidity Measurements in Meteorology) project lasted from 2003 until 2006 and provided GPS derived zenith and slant delays. The delay data has been assimilated into a numerical weather model whereof its impact was studied. The project E-GVAP (EUMETNET GPS Water Vapor Programme) includes over 1,800 European stations and ended in 2017. It established a fully operational European GPS meteorology service. The transitioning from near-real-time to true real-time is one of the current topics, such as the ongoing European COST Action ES1206. It aims to combine GPS, GLONASS and Galileo data for monitoring the troposphere and forecasting severe weather events. The UK Met Office and Météo France were the first that performed a large scale operational assimilation of GNSS for weather prediction after the founding of E-GVAP [62]. The UK Met Office assimilates GPS derived ZTDs into their North Atlantic and European NWP model since 2007 [63]. They conclude a general increase of relative humidity in the analyzed vertical levels and improvements of cloud forecasts. Trial analysis were performed between no-GPS, GPS 3D-Var and GPS 4D-Var. The trial GPS 3D-Var and no-GPS demonstrate a general decrease of the negative temperature forecast bias. According to their first analysis with 4D-Var assimilation, no significant benefits were identified over 3D-Var assimilation. Since 2012, global ZTD data processed by the Geodetic Observatory Pecny has also been assimilated into the Met Office global model [64]. Currently they are using double-differenced data, but in the future, the PPP technique may be applied to support an arbitrary amount of simultaneously processed stations.

An impact study of 4D-Var ZTD assmimilation at Météo France has been conducted by [65]. The conducted trials in winter, spring and summer 2005 indicate generally a positive impact of ZTD in 1 to 4 day forecasts. Compared to radiosondes minor improvements were observed on geopotentials and winds after the assimilation of GPS ZTD. The spring and summer trials suggest better forecasts in the +12 and +36 hour scales of precipitation patterns over France. Vedel and Huang [59] examined the impact of GPS ZTD assimilation into the HIRLAM local area NWP in Europe. They assimilated

the ZTD in 3D-Var mode with 0.45 and 0.15 degree resolution. They compared the results against rain gauge observations and report a positive impact on heavy precipitation events. Heavy precipitation was generally better predicted in regions with good GPS receiver coverage.

Since 2009 the Japan Meteorological Agency (JMA) uses the GEONET (GPS Earth Observation Network System) PWV estimates for their operational mesoscale analysis (Japan Meteorological Agency, 2013). The GEONET is a Japanese nationwide GPS observation network consisting of 1,300 stations and a horizontal resolution of approximately 20 km for the detection of crustal deformations in real-time. However, their data is also a valuable resource for meteorological applications. Their assimilation demonstrate a positive impact on NWP models (e.g. Seko *et al.* 7, Kawabata *et al.* [67]). Shoji *et al.* [68] demonstrate that the operational mesoscale model of the JMA was not able to predict a heavy rainfall event in 2008. The initial condition of the model underestimated the water vapor prior to the rainfall event driven by a positional error of a low-level convergence zone compared to the GEONET estimations. Assimilation of the GEONET and surrounding IGS stations with the JMA's mesoscale 4D-Var system resulted in an improvement of the positional convergence zone and forecast of the observed rainfall.

2.6.2. PWV-ONLY RAINFALL FORECASTING

PWV observations at a local scale in a high temporal resolution are essential for the now- and forecasting of localized severe rain. Local PWV fluctuations may be related with water vapor increases in the lower troposphere which leads to deep convection [69]. Seko *et al.* [7] report that about 20 minutes before rain occurs, the amount of water vapor in the atmosphere at 1 km height tends to increase. This can be an indicator for rainfall which in turn requires a high spatial and temporal monitoring of PWV. To investigate the temporal nature of GPS derived PWV for intense precipitation cases in the Lisbon region from 2010-2012, Benevides *et al.* [70] analyzed the evolution of ascending and descending trends in the PWV time series. Most severe rainfall events occurred after a long ascending period with a subsequent PWV decline. They implemented a simple algorithm to forecast 6h rainfall after a rapid increase of PWV. Their algorithm was able to predict heavy rainfalls, but also generated false alerts ranging from 15-85% depending on the threshold of the rate of change. A low PWV threshold of 0.3 $mm\,h^{-1}$ was able to predict all severe rain events and almost all other minor rain events, but generated false alerts of approximately 85%. Increasing the rate of change threshold monotonically decreases the correctly forecasted rain events and false alerts. However, the success rate of detecting severe rain events only decreases slowly, but drops sharply at a rate of change of about 2.5 $mm\,h^{-1}$. At $1.5 mm\,h^{-1}$, 90% of the severe events and 75% of the total rain could be tracked with an error of 60-70%. Using a $2.5 mm\,h^{-1}$ threshold results in the successful tracking of 75% severe rain events, 40% of the total rain and an error ratio of 40%. It must be noted that this simple forecasting algorithm is purely based on only GPS PWV estimations of a single station. The results coincide with prior findings e.g. by Champollion *et al.* [71] and Brenot *et al.* [8], which concluded that many but not all anomalous positive PWV peaks correlate positively with precipitation. The demonstrated relationship between temporal PWV increases and severe rain events are coherent with a similar study of Inoue and Inoue [72]. They show that PWV increments before thunderstorms

are essentially higher than those in other weather situations and suggest a clear relationship between convection and PWV increments. The results were also verified by a study of Shoji [69], who states an increase of the precipitation frequency when the PWV reached a certain threshold under consideration of the surface temperature.

2.6.3. INTER-TECHNIQUE VALIDATION STUDIES

SEVERAL studies were conducted that compare the water vapor estimations from GNSS with different measurement techniques. Choy *et al.* [73] compared GPS retrieved PWV estimations from eight dual-frequency GPS ground stations with radiosonde launches and two co-located Very Long Baseline Interferometry (VLBI) sites distributed throughout Australia from 2008-2012. They investigated the quality of GPS derived PWV with respect to their use in climate studies and research in Australia. A mean difference between GPS and VLBI was found less than 1 mm with a standard deviation of about 3.5 mm. Outliers were removed for the comparison of GPS to radiosonde measurements. Even though the distances between radiosonde sites and GPS receivers ranged between 7 km and 173 km, the closest GPS sites demonstrated a mean PWV difference of 0.1 mm and a standard deviation of 4 mm over the 5 year period. The largest spread was observed for stations with high atmospheric moisture and large distances between GPS and radiosonde sites. It must also be noted that further errors are introduced by the separation of GPS and meteorological sites (between 7 and 45 km). However, regarding their comparisons they concluded promising application of the GPS for climate research in Australia. They expect to improve the precision of GPS PWV estimations by colocating weather stations and radiosonde release sites.

Sato *et al.* [11] set up a dense real-time PWV system consisting of 17 dual-frequency GNSS receivers covering an area of approximately 10 x 6 km² around the Japanese Kyoto Uji campus. The inter-station distance is about 1-2 km. They validated the GNSS PWV estimations with radiosonde and radiometer measurements and achieved an RMS of about 2 mm. They also compared the closest GNSS single slant delays with the radiosonde and radiometer observations. Of their 15 radiosonde launches, they selected two with the special characteristics that one visible satellite was sufficiently close to the radiosonde path. They used the accumulated water vapor of the radiosonde until it reached an altitude of 10 km to track at least 99% of the water vapor in the atmosphere. It was demonstrated that the GNSS single slant water vapor estimate was much closer to the radiosonde PWV than using all available satellites. The result was verified with a second test during which one of the slant paths was sufficiently close to the radiosonde trajectory. The comparison with a radiometer to GNSS PWV estimation using all available satellites demonstrated a similar behavior to the radiosonde results. They achieved an RMS of about 2 mm. Using only a single satellite for validation, the short term temporal fluctuations were tracked better, but the overall performance was worse compared to the results obtained by using all satellites. However, this behavior was not confirmed during other tests. They point out that the bias between radiometer and single satellite may be caused by a radiometer calibration or GNSS modelling error. Sato *et al.* [11] compared the use of low-elevation cutoff angles and to the use of high elevation satellites within their experiment domain (10 x 6 km²). Using low-elevation satellites yields a smoother PWV temporal and horizontal distribution. This is caused by spatial averaging

over wider portions of the troposphere. For a height of 10 km and assuming a flat earth, an elevation cutoff of 10° monitors about 55 km in all directions whilst a cutoff of 60° only accounts for about a tenth of the area. By exploiting the permanent availability of at least one satellite in almost zenith direction (regional QZSS) they conclude an opportunity for an improvement of the detection of water vapor fluctuations than using the standard method. With regard to the increasing amount of satellites and regional GNSS like the QZSS in Japan, the use of high-elevation satellites increases the horizontal resolution. Sato *et al.* [11] concluded to use high elevation cutoff angles in dense networks to preserve the monitoring of local PWV fluctuations.

Lu *et al.* [74] estimated PWV in near-real-time using dual-frequency receivers in GPS-only, GLONASS-only and combined solution mode. They compared the results among each other and performed further comparisons with radiosonde measurements and VLBI data. Relative to the radiosonde observations, the GPS-only PWV solution shows an RMS of 1.6 - 2.4 mm. The RMS between GLONASS-only and radiosonde data behaves similar and ranges between 1.8 and 2.6 mm. The combined solution produced slightly more accurate PWV estimations with an RMS of 1.5 - 2.3 mm compared to the radiosonde measurements. The inter-comparison results of GLONASS-only to GPS-only show a PWV RMS of 1.2 mm. Compared to the VLBI data, the combined solution demonstrates the best results. The ZTD RMS ranges from 5.1 - 10.6 mm (equals a PWV of 0.8 - 1.7 mm). They conclude that more robust and accurate real-time PWV estimations can be obtained using the combined GPS/GLONASS solution. Studies using multi-GNSS demonstrate an improvement regarding positioning with a reduction of positioning convergence time [75, 76]. Only limited studies were performed that used GLONASS-only or a combined solution. Bruyninx [77] demonstrated a ZTD underestimation of about 0-2 mm from the combined solution compared to the GPS-only solution. However, the discrepancy disappeared after adoption of the new IGS antenna phase center models [78].

The GNSS-derived ZTD and PWV estimations based on geodetic-grade dual-frequency equipment have demonstrated their value for meteorological applications. The application thus far is predominantly based on using high-cost equipment distributed unevenly across the globe. This binds the capabilities to cost-intensive applications. Installing dense networks with such hardware is associated with substantial investment costs and for most cases economically not feasible. Low-cost GNSS equipment, recently introduced to the marked, may offer an alternative. The following chapters investigate meteorological and positioning applications of cost-efficient single- and dual-frequency receivers and demonstrate current performance and improvements for high precision applications.

REFERENCES

[1] J. T. Kiehl and K. E. Trenberth, *Earth's Annual Global Mean Energy Budget,* Bulletin of the American Meteorological Society **78**, 197 (1997).

[2] D. Andrews, *An Introduction to Atmospheric Physics*, International geophysics series (Cambridge University Press, 2000).

[3] R. D. Cess, G. L. Potter, J. P. Blanchet, G. J. Boer, A. D. Del Genio, M. Déqué, V. Dymnikov, V. Galin, W. L. Gates, S. J. Ghan, J. T. Kiehl, A. A. Lacis, H. Le Treut, Z.-X. Li, X.-Z. Liang, B. J. McAvaney, V. P. Meleshko, J. F. B. Mitchell, J.-J. Morcrette, D. A. Randall, L. Rikus, E. Roeckner, J. F. Royer, U. Schlese, D. A. Sheinin, A. Slingo, A. P. Sokolov, K. E. Taylor, W. M. Washington, R. T. Wetherald, I. Yagai, and M.-H. Zhang, *Intercomparison and interpretation of climate feedback processes in 19 atmospheric general circulation models,* Journal of Geophysical Research: Atmospheres **95**, 16601 (1990).

[4] B. Hofmann-Wellenhof, H. Lichtenegger, and E. Wasle, *GNSS - Global Navigation Satellite Systems* (Springer-Verlag Wien New York, 2008).

[5] C. Field, V. Barros, T. Stocker, Q. Dahe, D. Jon Dokken, K. Ebi, M. Mastrandrea, K. Mach, G. Plattner, S. Allen, M. Tignor, and P. Midgley, *Managing the risks of extreme events and disasters to advance climate change adaptation: Special report of the intergovernmental panel on climate change* (Cambridge University Press, 2012) pp. 1–582.

[6] T. Stocker, D. Qin, G.-K. Plattner, M. Tignor, S. Allen, J. Boschung, A. Nauels, Y. Xia, V. Bex, and P. Midgley, *Climate change 2013 the physical science basis: Working Group I contribution to the fifth assessment report of the intergovernmental panel on climate change* (Cambridge University Press, 2013) pp. 1–1535.

[7] H. Seko, H. Nakamura, Y. Shoji, and T. Iwabuchi, *The meso-y scale water vapor distribution associated with a thunderstorm calculated from a dense network of GPS receivers,* Journal of the Meteorological Society of Japan **82**, 569 (2004).

[8] H. Brenot, A. Walpersdorf, M. Reverdy, J. Van Baelen, V. Ducrocq, C. Champollion, F. Masson, E. Doerflinger, P. Collard, and P. Giroux, *A GPS network for tropospheric tomography in the framework of the Mediterranean hydrometeorological observatory Cévennes-Vivarais (southeastern France),* Atmospheric Measurement Techniques **7**, 553 (2014).

[9] S. J. Bauer, *Physics of Planetary Ionospheres*, Vol. 6 (Springer Science & Business Media, 1973).

[10] B. Hofmann-Wellenhof, G. Kienast, and H. Lichtenegger, *Global Positioning System: Theroy and Practice*, 5th ed. (Springer-Verlag Wien New York, 2001).

[11] K. Sato, E. Realini, T. Tsuda, M. Oigawa, Y. Iwaki, Y. Shoji, and H. Seko, *A high-resolution, precipitable water vapor monitoring system using a dense network of GNSS receivers,* Journal of Disaster Research **8**, 37 (2013).

[12] M. Bevis, S. Businger, T. A. Herring, C. Rocken, R. A. Anthes, and R. H. Ware, *GPS meteorology: Remote sensing of atmospheric water vapor using the global positioning system,* Journal of Geophysical Research: Atmospheres **97**, 15787 (1992).

[13] G. M. Resch, *Inversion algorithms for water vapor radiometers operating at 20.7 and 31.4 GHz,* in *The Telecommunications and Data Acquisition Report* (1984).

[14] G. E. Becker and S. H. Autler, *Water Vapor Absorption of Electromagnetic Radiation in the Centimeter Wave-Length Range,* Physical Review (1946), 10.1103/PhysRev.70.300.

[15] B. L. Gary, S. J. Keihm, and M. A. Janssen, *Optimum strategies and performance for the remote sensing of path-delay using ground-based microwave radiometers,* IEEE transactions on geoscience and remote sensing , 479 (1985).

[16] D. W. Draper, D. A. Newell, F. J. Wentz, S. Krimchansky, and G. M. Skofronick-Jackson, *The Global Precipitation Measurement (GPM) Microwave Imager (GMI): Instrument Overview and Early On-Orbit Performance,* IEEE Journal of Selected Topics in Applied Earth Observations and Remote Sensing **8**, 3452 (2015).

[17] G. M. Resch, *Water Vapor Radiometry in Geodetic Applications,* in *Geodetic Refraction: Effects of Electromagnetic Wave Propagation Through the Atmosphere*, edited by F. K. Brunner (Springer Berlin Heidelberg, Berlin, Heidelberg, 1984) pp. 53–84.

[18] R. Ware, C. Alber, C. Rocken, and F. Solheim, *Sensing Integrated Water Vapor along GPS Ray Paths,* Geophysical Research Letters **24**, 417 (1997).

[19] J. Braun and C. Rocken, *Comparisons of Line-of-Sight Water Vapor Observations Using the Global Positioning System and a Pointing Microwave Radiometer,* Journal of Atmospheric and Oceanic Technology **20**, 606 (2003).

[20] S. I. Gutman and S. G. Benjamin, *The Role of Ground-Based GPS Meteorological Observations in Numerical Weather Prediction,* GPS Solutions **4**, 16 (2001).

[21] W. P. Elliott, *On detecting long-term changes in atmospheric moisture,* Climatic Change **31**, 349 (1995).

[22] O. J. Sovers, J. L. Fanselow, and C. S. Jacobs, *Astrometry and geodesy with radio interferometry: experiments, models, results,* Reviews of Modern Physics **70**, 1393 (1998).

[23] R. Hanssen, I. Weinreich, S. Lehner, and A. Stoffelen, *Tropospheric wind and humidity derived from spaceborne radar intensity and phase observations,* Geophysical Research Letters **27**, 1699 (2000).

[24] F. Beauducel, P. Briole, and J.-L. Froger, *Volcano-wide fringes in ERS synthetic aperture radar interferograms of Etna (1992–1998): Deformation or tropospheric effect?* Journal of Geophysical Research: Solid Earth **105**, 16391 (2000).

[25] J. L. Davis, T. A. Herring, I. I. Shapiro, A. E. E. Rogers, and G. Elgered, *Geodesy by radio interferometry: Effects of atmospheric modeling errors on estimates of baseline length,* Radio Science **20**, 1593 (1985).

[26] P. Tregoning, R. Boers, D. O'Brien, and M. Hendy, *Accuracy of absolute Precipitable Water vapor estimates from GPS observations,* Journal of Geophysical Research Atmospheres **103**, 28701 (1998).

[27] D. Wolfe and S. Gutman, *Developing an operational, surface-based, GPS, water vapor observing system for NOAA: Network design and results,* Journal of Atmospheric and Oceanic Technology **17**, 426 (2000).

[28] A. Walpersdorf, M.-N. Bouin, O. Bock, and E. Doerflinger, *Assessment of GPS data for meteorological applications over Africa: Study of error sources and analysis of positioning accuracy,* Journal of Atmospheric and Solar-Terrestrial Physics **69**, 1312 (2007).

[29] E. Kursinski, G. Hajj, J. Schofield, R. Linfield, and K. R. Hardy, *Observing Earth's atmosphere with radio occultation measurements using the Global Positioning System,* Journal of Geophysical Research: Atmospheres **102**, 23429 (1997).

[30] E. R. Kursinski, G. A. Hajj, K. R. Hardy, L. J. Romans, and J. T. Schofield, *Observing tropospheric water vapor by radio occultation using the Global Positioning System,* Geophysical Research Letters **22**, 2365 (1995).

[31] J. Wickert, C. Reigber, G. Beyerle, R. König, C. Marquardt, T. Schmidt, L. Grunwaldt, R. Galas, T. K. Meehan, W. G. Melbourne, and K. Hocke, *Atmosphere sounding by GPS radio occultation: First results from CHAMP,* Geophysical Research Letters **28**, 3263 (2001).

[32] G. Wübbena, A. Bagge, and M. Schmitz, *RTK Networks based on GEO++ GNSMART - Concepts, Implementation, Results,* Proc. ION GPS-2001, Salt Lake City (2001).

[33] G. Seeber, *Satellite Geodesy*, 2nd completely revised and extended edition ed. (Walter de Gruyter, 2003).

[34] G. Blewitt, *An automatic editing algorithm for GPS data,* Geophysical Research Letters **17**, 199 (1990).

[35] H. Landau, U. Vollath, and X. Chen, *Virtual Reference Station Systems,* Journal of Global Positioning Systems **1**, 137 (2002).

[36] J. Zumberge, M. Heflin, D. Jefferson, M. Watkins, and F. Webb, *Precise point positioning for the efficient and robust analysis of GPS data from large networks,* Journal of Geophysical Research B: Solid Earth **102**, 5005 (1997).

[37] S. Schaer, *Mapping and predicting the Earth's ionosphere using the Global Positioning System.* Geod.-Geophys. Arb. Schweiz, Vol.59 **59** (1999).

[38] C. Rocken, J. Johnson, J. Braun, H. Kawawa, Y. Hatanaka, and T. Imakiire, *Improving GPS surveying with modeled ionospheric corrections,* Geophysical Research Letters **27**, 3821 (2000).

[39] V. Janssen and C. Rizos, *Mixed-mode GPS deformation monitoring a cost-effective and accurate alternative?* in *Proceedings of the International Association of Geodesy, IAG 2003*, Vol. 128 (2005) pp. 533–537.

[40] Z. Deng, M. Bender, G. Dick, M. Ge, J. Wickert, M. Ramatschi, and X. Zou, *Retrieving tropospheric delays from GPS networks densified with single frequency receivers,* Geophysical Research Letters **36** (2009), 10.1029/2009GL040018.

[41] Z. Deng, M. Bender, F. Zus, M. Ge, G. Dick, M. Ramatschi, J. Wickert, U. Lhnert, and S. Schön, *Validation of tropospheric slant path delays derived from single and dual frequency GPS receivers,* Radio Science **46** (2011), 10.1029/2011RS004687.

[42] J. Kouba and P. Héroux, *Precise Point Positioning Using IGS Orbit and Clock Products,* GPS Solutions **5**, 12 (2001).

[43] J. Kouba, *A guide to using International GNSS Service (IGS) products,* (2015).

[44] H. van der Marel and B. Gündlich, *Development of Models for Use of Slant Delays Slant Delay Retrieval and Multipath Mapping Software Report for WP6100 TOUGH Deliverable D33*, TU Delft (2003).

[45] G. Thayer, *An improved equation for the radio refractive index of air,* Radio Science **9**, 803 (1974).

[46] J. Saastamoinen, *Contributions to the theory of atmospheric refraction,* Bulletin Géodésique **46**, 279 (1972).

[47] H. W. Janes, R. B. Langley, and N. S. P., *A comparison of several models for the prediction of tropospheric propagation delay,* Proceedings 5th International Geodetic Symposium on Satellite Positioning, Las Cruces, New Mexico, USA , 777 (1989).

[48] M. Bevis, *GPS meteorology: mapping zenith wet delays onto precipitable water,* Journal of Applied Meteorology **33**, 379 (1994).

[49] A. Niell, *Global mapping functions for the atmosphere delay at radio wavelengths,* Journal of Geophysical Research: Solid Earth **101**, 3227 (1996).

[50] J. Boehm, B. Werl, and H. Schuh, *Troposphere mapping functions for GPS and very long baseline interferometry from European Centre for Medium-Range Weather Forecasts operational analysis data,* Journal of Geophysical Research: Solid Earth **111** (2006).

[51] T. Nilsson, J. Böhm, D. D. Wijaya, A. Tresch, V. Nafisi, and H. Schuh, *Path Delays in the Neutral Atmosphere,* in *Atmospheric Effects in Space Geodesy*, edited by J. Böhm and H. Schuh (Springer Berlin Heidelberg, Berlin, Heidelberg, 2013) pp. 73–136.

[52] D. MacMillan, *Atmospheric gradients from very long baseline interferometry observations,* Geophysical Research Letters **22**, 1041 (1995).

[53] S. de Haan, *Measuring atmospheric stability with GPS,* Journal of Applied Meteorology and Climatology **45**, 467 (2006).

[54] J. Haase, M. Ge, H. Vedel, and E. Calais, *Accuracy and variability of GPS tropospheric delay measurements of water vapor in the western Mediterranean,* Journal of Applied Meteorology **42**, 1547 (2003).

[55] G. Gendt, G. Dick, C. Reigber, M. Tomassini, Y. Liu, and M. Ramatschi, *Near real time GPS water vapor monitoring for numerical weather prediction in Germany,* Journal of the Meteorological Society of Japan **82**, 361 (2004).

[56] O. Bock, M.-N. Bouin, A. Walpersdorf, J. Lafore, S. Janicot, F. Guichard, and A. Agusti-Panareda, *Comparison of ground-based GPS precipitable water vapour to independent observations and NWP model reanalyses over Africa,* Quarterly Journal of the Royal Meteorological Society **133**, 2011 (2007).

[57] S. de Haan, *National/regional operational procedures of GPS water vapour networks and agreed international procedures*, Tech. Rep. (World Meteorological Organization, 2006).

[58] S. Gutman, S. Sahm, S. Benjamin, B. Schwartz, K. Holub, J. Stewart, and T. Smith, *Rapid retrieval and assimilation of ground based GPS precipitable water observations at the NOAA Forecast Systems Laboratory: Impact on weather forecasts,* Journal of the Meteorological Society of Japan **82**, 351 (2004).

[59] H. Vedel and X.-Y. Huang, *Impact of Ground Based GPS Data on Numerical Weather Prediction,* Journal of the Meteorological Society of Japan. Ser. II **82**, 459 (2004).

[60] J. Haase, E. Calais, J. Talaya, A. Rius, F. Vespe, R. Santangelo, X.-Y. Huang, J. Davila, M. Ge, L. Cucurull, A. Flores, C. Sciarretta, R. Pacione, M. Boccolari, S. Pugnaghi, H. Vedel, K. Mogensen, X. Yang, and J. Garate, *The contributions of the MAGIC project to the COST 716 objectives of assessing the operational potential of ground-basedGPS meteorology on an international scale,* Physics and Chemistry of the Earth, Part A: Solid Earth and Geodesy **26**, 433 (2001).

[61] G. Elgered, H. Plag, H. V. D. Marel, S. Barlag, and J. Nash, *Exploitation of Ground-based GPS for Operational Numerical Weather Prediction and Climate Applications - Final Report* (EU Publications Office (OPOCE), 2005).

[62] G. Guerova, J. Jones, J. Douša, G. Dick, S. De Haan, E. Pottiaux, O. Bock, R. Pacione, G. Elgered, H. Vedel, and M. Bender, *Review of the state of the art and future prospects of the ground-based GNSS meteorology in Europe,* Atmospheric Measurement Techniques **9**, 5385 (2016).

[63] G. V. Bennitt and B. Jupp, *Operational Assimilation of GPS Zenith Total Delay Observations into the Met Office Numerical Weather Prediction Models,* Monthly Weather Review **140**, 2706 (2012).

[64] J. Dousa and G. Bennitt, *Estimation and evaluation of hourly updated global GPS Zenith Total Delays over ten months,* GPS Solutions **17**, 453 (2013).

[65] P. Poli, P. Moll, F. Rabier, G. Desroziers, B. Chapnik, L. Berre, S. Healy, E. Andersson, and F.-Z. El Guelai, *Forecast impact studies of zenith total delay data from European near real-time GPS stations in Météo France 4DVAR,* Journal of Geophysical Research: Atmospheres **112** (2007).

[66] J. M. Agency, *Outline of the operational numerical weather prediction at the Japan Meteorological Agency*, techreport (JMA, 1-3-4 Otemachi, Chiyoda-ku, Tokyo 100-8122, Japan, 2013).

[67] T. Kawabata, H. Seko, K. Saito, T. Kuroda, K. Tamiya, T. Tsuyuki, Y. Honda, and Y. Wakazuki, *An assimilation and forecasting experiment of the nerima heavy rainfall with a cloud-resolving nonhydrostatic 4-dimensional variational data assimilation system,* Journal of the Meteorological Society of Japan. Ser. II **85**, 255 (2007).

[68] Y. Shoji, M. Kunii, and K. Saito, *Assimilation of Nationwide and Global GPS PWV Data for a Heavy Rain Event on 28 July 2008 in Hokuriku and Kinki, Japan,* SOLA **5**, 45 (2009).

[69] Y. Shoji, *Retrieval of Water Vapor Inhomogeneity Using the Japanese Nationwide GPS Array and its Potential for Prediction of Convective Precipitation,* Journal of the Meteorological Society of Japan. Ser. II **91**, 43 (2013).

[70] P. Benevides, J. Catalao, and P. Miranda, *On the inclusion of GPS precipitable water vapour in the nowcasting of rainfall,* Natural Hazards and Earth System Sciences **15**, 2605 (2015).

[71] C. Champollion, F. Masson, J. Van Baelen, A. Walpersdorf, J. Chéry, and E. Doerflinger, *GPS monitoring of the tropospheric water vapor distribution and variation during the 9 September 2002 torrential precipitation episode in the Cévennes (southern France),* Journal of Geophysical Research D: Atmospheres **109**, 1 (2004).

[72] H. Y. Inoue and T. Inoue, *Characteristics of the Water-Vapor Field over the Kanto District Associated with Summer Thunderstorm Activities,* SOLA **3**, 101 (2007).

[73] S. Choy, C.-S. Wang, T.-K. Yeh, J. Dawson, M. Jia, and Y. Kuleshov, *Precipitable water vapor estimates in the Australian region from ground-based GPS observations,* Advances in Meteorology **2015** (2015), 10.1155/2015/956481.

[74] C. Lu, X. Li, M. Ge, R. Heinkelmann, T. Nilsson, B. Soja, G. Dick, and H. Schuh, *Estimation and evaluation of real-time precipitable water vapor from GLONASS and GPS,* GPS Solutions **20**, 703 (2016).

[75] C. Cai and Y. Gao, *Modeling and assessment of combined GPS/GLONASS precise point positioning,* GPS Solutions **17**, 223 (2013).

[76] X. Li, X. Zhang, X. Ren, M. Fritsche, J. Wickert, and H. Schuh, *Precise positioning with current multi-constellation Global Navigation Satellite Systems: GPS, GLONASS, Galileo and BeiDou,* Scientific Reports **5**, 8328 (2015).

[77] C. Bruyninx, *Comparing GPS-only with GPS + GLONASS positioning in a regional permanent GNSS network,* GPS Solutions **11**, 97 (2007).

[78] R. Dach, R. Schmid, M. Schmitz, D. Thaller, S. Schaer, S. Lutz, P. Steigenberger, G. Wübbena, and G. Beutler, *Improved antenna phase center models for GLONASS,* GPS Solutions **15**, 49 (2011).

3

POTENTIAL OF COST-EFFICIENT SINGLE-FREQUENCY GNSS RECEIVERS FOR WATER VAPOR MONITORING

Dual-frequency Global Navigation Satellite System (GNSS) enable the estimation of Zenith Tropospheric Delay (ZTD) which can be converted to Precipitable Water Vapor (PWV). The density of existing GNSS monitoring networks is insufficient to capture small-scale water vapor variations that are especially important for extreme weather forecasting. A densification with geodetic-grade dual-frequency receivers is economically not feasible. Cost-efficient single-frequency receivers offer a possible alternative. This paper studies the feasibility of using low-cost receivers to increase the density of GNSS networks for retrieval of PWV. We processed one year of GNSS data from an IGS station and two co-located single-frequency stations. Additionally, in another experiment, the Radio Frequency (RF) signal from a geodetic-grade dual-frequency antenna was split to a geodetic receiver and two low-cost receivers. To process the single-frequency observations in Precise Point Positioning (PPP) mode, we apply the Satellite-specific Epoch-differenced Ionospheric Delay (SEID) model using two different reference network configurations of 50-80 kilometers and 200-300 kilometers mean station distance respectively. Our research setup enables distinguishing between the antenna, ionospheric interpolation and software related impacts on the quality of PWV retrievals. The study shows that single-frequency GNSS receivers can achieve a similar quality as geodetic receivers in terms of RMSE for ZTD estimations. We demonstrate that modeling of the ionosphere and the antenna type are the main sources influencing the ZTD precision.

This chapter has been published as: Krietemeyer, A.; ten Veldhuis, M.-C.; van der Marel, H.; Realini, E.; van de Giesen, N. Potential of Cost-Efficient Single Frequency GNSS Receivers for Water Vapor Monitoring. Remote Sens. **2018**, 10, 1493.

3.1. INTRODUCTION

WATER vapor plays an important role for atmospheric processes. It is the most abundant greenhouse gas [1] and is spatially and temporally highly variable [2]. Atmospheric water vapor is essential for convection in the lower atmosphere and hence crucial for the generation of clouds and rainfall. A relationship between water vapor fields and severe weather events has been observed e.g. by Seko *et al.* [3]. With regard to a warming climate, the amount of water vapor in the atmosphere increases and causes additional absorption of long-wave radiation and reflects it back to the ground [4]. Water vapor also transports latent heat through the atmosphere. Distribution of atmospheric water vapor is an important factor for weather models and its monitoring is crucial for weather research. The traditional method to measure water vapor in the air is by releasing radiosonde balloons. However, the releases are typically only performed a few times per week and are characterized by distances often greater than 100 km.

Another approach is to determine Precipitable Water Vapor (PWV) from the observed delay in Global Navigation Satellite System (GNSS) transmitted signals. The estimated Zenith Tropospheric Delay (ZTD) is the driving factor to obtain PWV and uncertainties in ZTD dominate the error budget of PWV [5]. Monitoring local inhomogeneities of water vapor that may be associated with deep convection is important for the prediction of severe weather events. One should note that existing weather radars can only detect clouds after the start of precipitation. Currently, PWV derived from globally, nationally and regionally distributed networks of dual-frequency receivers is used to improve existing numerical weather models [6]. The networks were originally designed for geodetic applications and are characterized by an inhomogeneous distribution and inter-station distances in the order of tens of kilometers or above. Due to their high inter-station distances, these networks are often not sufficiently dense to monitor small-scale water vapor fluctuations ([7] and [8]). Real-Time Kinematic (RTK) networks are already characterized by station distances below 30 km (e.g. Netherlands or Germany). Some networks, such as the Japanese GEONET even reach inter-station distances of about 20 km [9]. In our study, networks with average station distances of around 30 km are considered as dense. Regional networks in Europe with station distances between 70 - 100 km are considered as low density networks. However, even networks with inter-station distances of 20 km are not dense enough to properly detect water vapor variations associated to localized convective phenomena [10]. The cost of dual-frequency receivers exceeds several thousands dollars. Driven by these economic reasons, the use of dual-frequency receivers for water vapor monitoring is not feasible at high density. Instead, inexpensive single-frequency receivers already available at a cost of a hundred to a few hundred dollars offer an interesting alternative. Having been designed to be embedded into mass-market devices such as car navigation equipment and smartphones, these inexpensive receiver modules and antennas are more economical than their dual-frequency geodetic counterparts in terms of both money and power consumption (in case of off-grid application).

Currently, widespread application of single-frequency GNSS is limited by errors introduced by the ionosphere. Different strategies exist to obtain ZTD estimations, e.g. the network approach based on double differences or the Precise Point Positioning (PPP) based on undifferenced observations. A comprehensive analysis using different map-

ping functions, cutoff angle and utilizing different positioning methods has been performed by Baldysz *et al.* [11]. In their study the PPP performed better than the differential approach for PWV linear trend analysis. To account for the error caused by the ionosphere, we apply the Satellite-specific and Epoch-differenced Ionospheric Delay (SEID) model as proposed by Deng *et al.* [12]. This allows us to treat the single-frequency data as dual-frequency data and process it with well known PPP software [13]. The primary goal of this study is to investigate the feasibility of low-cost single frequency receivers to densify existing dual-frequency networks and examine the error sources that the receivers are prone to. The research is a first step to examine the potential wide-spread deployment of low-cost GNSS receivers in data sparse regions with limited investment budgets. It aims to highlight the trade-off between using cost-efficient devices compared to their expensive, geodetic-grade dual-frequency counterparts for water vapor monitoring. For this purpose we conducted a monitoring experiment alongside an International GNSS Service (IGS) station and compared our results with available reference datasets. Earlier studies e.g. by Deng *et al.* [12], Deng *et al.* [14] and Realini *et al.* [8] demonstrated the feasibility of applying single-frequency GNSS in PPP mode. In our study we used two different types of low-cost on-site single-frequency receivers and investigated their performance for monitoring water vapor. Durable, weather-proof stations incorporating low-cost GNSS receivers are a recent development and were not available on the market before 2015. Even today only a few startup and small- and medium sized enterprises produce them. One of the low-cost single frequency stations used in this study is the GeoGuard Monitoring Unit (GMU) designed by the Italian company GReD [15]. All components are Ingress Protection (IP) 66 or 67 certified and the first units operate since November 2015. Currently 70 GMU stations are continuously monitored by GeoGuard from which some are also deployed in harsh conditions like mountainous areas above 2000 m and near the sea. Even though our experimental setup could make use of an already dense RTK network for the ionospheric interpolation, we selected more challenging station distances and only a minimum of SEID reference stations. The study uses exclusively open source models and publicly available datasets to support applicability of the setup to other locations. By co-locating multiple different sensors and splitting the antenna signal of a calibrated geodetic-grade antenna to a geodetic-grade receiver, low-cost single- and dual-frequency devices we were able to make statements about the impact of receiver and antenna related errors. The study is organized as follows: Section 2 describes the basics of the GNSS meteorology, the SEID algorithm and the experimental setup and data processing methods. Section 3 illustrates the ZTD reference comparison, the experimental setup results using two different SEID constellations and the splitted antenna experiment results. Section 4 and 5 contain the discussion and conclusion part.

3.2. METHODOLOGY

3.2.1. WATER VAPOR FROM GNSS MEASUREMENTS

TRADITIONAL GNSS geodesy aims to obtain precise positioning information from the signal delay between a GNSS receiver and satellites in sight. The delay is affected by several error sources such as clock errors, antenna phase center variations and tropospheric and ionospheric delays. The tropospheric delay is further separated into a dry (hydrostatic) delay and a wet delay as result of atmospheric water vapor part. The Slant Total Delays (STDs) along each satellite-receiver line of sight are mapped to the zenith direction in order to estimate the ZTD. In GNSS meteorology, the ZTD can be directly assimilated in numerical weather models, or the ZTD can be converted into PWV using surface pressure data and a simple model of the atmosphere.

According to Thayer [16], the refractivity in the troposphere can be considered as the sum of a dry (hydrostatic) and wet component which can be related to the atmospheric temperature and partial pressure of water vapor and dry gases:

$$N = N_{dry} + N_{wet} = k_1 \frac{p_d}{T} + k_2 \frac{e}{T} + k_3 \frac{e}{T^2} \tag{3.1}$$

Where $k_1 \frac{p_d}{T}$ accounts for the dry part and the last two terms for the wet part. p_d is the combined partial pressure of dry gases in mbar, T the temperature in degree Kelvin and e the partial pressure of water vapor in mbar. The empirical constants $k_1 = (77.604 \pm 0.014) K\ mbar^{-1}$, $k_2 = (64.79 \pm 0.08) K\ mbar^{-1}$ and $k_3 = (3.776 \pm 0.004) 10^5 K^2\ mbar^{-1}$ were determined by Thayer [16]. The integrals of the refractivity N in the zenith direction are referred to as Zenith Hydrostatic Delay (ZHD) and Zenith Wet Delay (ZWD). The ZHD can be estimated using the Saastamoinen model [17]:

$$ZHD = \frac{0.0022768 P_0}{1 - 0.00266 \cos(2\Phi) - 0.00028 H} \tag{3.2}$$

Where P_0 is the total atmospheric pressure in mbar expected to be observed at the receiver position, Φ is the latitude in radians and H the orthometric height (i.e. above the reference geoid) in kilometers.

The approach to estimate the non-hydrostatic delay by taking the difference between ZTD and ZHD is preferred since the wet delay is much more variable than the hydrostatic delay and its predictive value is poor in comparison to the ZHD estimation. Bevis *et al.* [18] demonstrate how the ZTD observed from GPS measurements can be used to derive PWV with given pressure and temperature data. Using the ZWD, the PWV can be estimated with a non-dimensional ratio Π:

$$\Pi = \frac{10^6}{\rho R_v [(\frac{k_3}{T_m}) + k_2']} \tag{3.3}$$

With T_m being the weighted mean temperature of the atmosphere in degree Kelvin, ρ the density of liquid water in $kg\ m^{-3}$, R_v the specific gas constant of water vapor in $J\ (kg\ K)^{-1}$ and k_2' defined as $k_2' = k_2 - m k_1$ with m being the ratio of molar masses of water vapor ($18.015\ g\ mol^{-1}$) and dry air ($28.964\ g\ mol^{-1}$). The constants k_1, k_2 and k_3 are the same as proposed by Thayer [16]. The weighted mean temperature of the

atmosphere T_m is computed based on radiosonde measurements. However, a simplified model using surface temperature measurements is sufficiently accurate. In our analysis we use the T_m derived by Baltink *et al.* [19] based on 9129 radiosonde ascents in De Bilt, Netherlands:

$$T_m = 0.673\,T_s + 83.0 \tag{3.4}$$

With T_s defined as the surface temperature in Kelvin. The water vapor conversion factor Π ranges typically around 0.16 and varies up to 20% depending on the location, height and meteorological conditions [20]. The PWV is related to the Integrated Water Vapor (IWV) overlying the receiver, whereby the PWV is defined as the height of an equivalent column of liquid water. The PWV is obtained by:

$$PWV = \Pi \cdot ZWD \tag{3.5}$$

Since there are no on-site temperature and air pressure observations available at our experimental setup, we are using measurements from the nearest weather station at 5 km distance and negligible elevation difference. We utilize the EGM2008 geoid model [21] to convert between the ellipsoidal and orthometric height at the station position. The conversion between mean-sea-level atmospheric pressure to the station height is performed by applying a standard lapse rate formula in mbar per meter after the ideal gas law [22]:

$$\frac{\delta P}{\delta h} = -\frac{P\,M\,g}{R\,(T+273.2)} \tag{3.6}$$

With P being the pressure in mbar, T the temperature in degree Celsius, M the mean molar mass of atmospheric gases ($0.02896 kg\ mol^{-1}$), g the gravity acceleration ($9.807\ m\ s^{-2}$) and R the universal gas constant ($8.314 J\ K^{-1}\ mol^{-1}$) respectively. With P being the pressure in mbar and T the temperature in degree Celsius respectively. Accounting for the geoidal undulation is important since the height error will develop a pressure offset. Utilizing the Saastamoinen formula (equation 3.2) shows that a pressure error of one mbar results in an error of around 2.28 mm in ZHD at our station coordinates.

3.2.2. SEID IONOSPHERIC DELAY MODELING

SINCE it is not possible to obtain an ionosphere-free linear combination based on single-frequency receiver data, the ionosphere must be modeled. In order to process single-frequency receivers within a network of dual-frequency receivers with conventional GNSS processing engines Deng *et al.* [12] developed the SEID model. They use the geometry-free ionospheric observation L_4 [23], which is defined as:

$$L_4 = L_1 - L_2 = \lambda_1 A_1 - \lambda_2 A_2 - 40.28\left(\frac{1}{f_1^2} - \frac{1}{f_2^2}\right) \cdot STEC(\lambda, \theta) \tag{3.7}$$

For simplicity the noise and multipath errors are ignored in the equation. L_1 and L_2 denote the carrier-phase measurements. The term $40.28\left(\frac{1}{f_1^2} - \frac{1}{f_2^2}\right) \cdot STEC(\lambda, \theta)$ denotes

the ionospheric delay on the system-dependent frequencies f_1 and f_2. $STEC$ is the Slant Total Electron Content which is defined as the integral of the electron density along the signal path. λ and θ are latitude and longitude of the Ionospheric Pierce Points (IPPs) of the ray paths on the single-shell defined ionosphere layer at 350 km height. λ_1 and λ_2 are the wavelengths and A_1 and A_2 denote the phase ambiguities on the respective frequencies. [24] demonstrate that the epoch-differenced ionospheric delays are sufficiently accurate to remove the ionospheric delay under normal ionospheric conditions for ZTD estimations. Since the estimation of the ambiguity parameter remains a major obstacle in GNSS processing, the epoch-differences dL_4 are used:

$$dL_4(j+1) = L_4(j+1) - L_4(j) = 40.28(\frac{1}{f_1^2} - \frac{1}{f_2^2}) \cdot dSTEC(\lambda, \theta) \tag{3.8}$$

Utilizing this equation, the ambiguity parameters between two continuously tracked epochs is eliminated. One should note that cycle slips must be removed and phase center variations applied in advance. In small-scale networks, the $dSTEC$ can be modeled with a linear function with the latitude and longitude θ and λ of the IPPs. For each pair of epochs and for each satellite, equation 3.8 can be approximated by the linear function:

$$dL_4(j+1) = a_0 + a_1\lambda + a_2\theta \tag{3.9}$$

Where the model parameters a_0, a_1 and a_2 are to be estimated by means of least-squares from the epoch-differenced ionospheric delays of at least three the surrounding dual-frequency stations. Using this model, the epoch-differenced ionospheric correction $d\tilde{L}_4(j+1)$ of any receiver within the spanned network may be calculated. The sum of the continuously tracked ionospheric corrections from j_0 to j_n results in:

$$\tilde{L}_4(j_n) = \sum_{j_0}^{j_n} d\tilde{L}_4 + L_4(j_0) \tag{3.10}$$

As depicted in equation 3.10, the ionospheric delay at epoch j_0 is unknown (thus set to zero). Unfortunately, this destroys the integer nature of the phase ambiguity in the interpolated data, meaning it can never be fixed to integer. However, since in typical PPP the ambiguities are not fixed to integer (but estimated as float values), this has no impact on the data processing. The synthesized $\tilde{L}_2$ signal is constructed from the difference between L_1 and $\tilde{L}_4$:

$$\tilde{L}_2 = L_1 - \tilde{L}_4 \tag{3.11}$$

The synthesized observable provides the same information as L_1, except that the ionospheric delay is adjusted to the L_2 frequency. Employing the generated dual-frequency data allows utilizing the ionosphere-free linear combination in conventional PPP-mode.

3.2.3. EXPERIMENTAL SETUP AND DATA PROCESSING

THE GNSS data server at the TU Delft collects data from the Dutch Permanent GNSS Array (DPGA) which consists of up to 18 continuously operating dual-frequency receivers throughout the Netherlands. The regional network density is considered as low

since its stations are typically located at 50 - 100 km distance. The data is publicly available and mainly used for research, educational purposes and to provide data to the International GNSS Service (IGS), EUREF Permanent Network (EPN) and EUMETNET GNSS water vapour programme (E-GVAP).

To investigate the feasibility of low-cost single-frequency receivers for water vapor monitoring, we designed an experimental setup along the existing IGS station DLF1 in Delft, Netherlands. The setup consists of one dual-frequency receiver (IGS station DLF1) and two co-located low-cost single-frequency receivers. The IGS station DLF1 is equipped with a geodetic-grade calibrated choke ring antenna. The antenna type is the current state-of-the-art and serves in our experiment as a reference for the best available antenna observations. One single-frequency station is the GMU which consists of a u-blox LEA-M8T single-frequency receiver with a Tallysman TW3470 antenna. The device has been successfully validated and is currently used for operational deformation monitoring [15]. It is fully autonomous and equipped with a solar panel and wireless (3G) data communication. Additionally we co-located a u-blox NEO-M8T evaluation toolkit (UBX) equipped with its standard ANN-MS patch antenna.

To apply the SEID algorithm, we selected two SEID reference constellations. The first constellation (DPGA case) consists of 4 stations (VLIS, IJMU, KOS1 and APEL) from the Dutch permanent network. The stations KOS1 and APEL were chosen as a backup for each other, since both have data gaps during the observation period. These are, however, different dates and the SEID model is still functioning by using only 3 instead of 4 reference stations. The total area covered in this case is about 6400 km^2. To analyze the effect of the SEID reference network distances, we added a second SEID constellation (EUREF case) utilizing stations from the EUREF network to our study. The stations are HERT (Great Britain), BORJ (Germany) and DOUR (Belgium). They are located in approximately 305, 240 and 215 km distance from the experimental setup in Delft. The conversion from ZTD to PWV is performed by using data from an Automatic Weather Station (AWS) located at 5 km distance from Delft, operated by the Royal Netherlands Meteorological Institute (KNMI) for temperature and air pressure observations. The station locations are illustrated in Figure 3.1.

We selected the analysis period from 1 January until 31 December 2017 to cover both low (winter) and high (summer) water vapor activities. During winter the PWV at this location typically ranges between 1 to 30 mm, whereas the summer is characterized with PWV values between 10 and 50 mm. However, the single-frequency units GMU and UBX only provide data since September 2017. The IGS station DLF1 provides continuous high-rate data throughout the year with a temporal resolution of up to 1 second. For our analysis we use this dual-frequency data to perform PPP to obtain a reference ZTD dataset. In order to validate the SEID modeling we simulate a single-frequency unit (DLF1_SF) by removing the code and phase data from the second frequency (C2 and L2) with the teqc [25] software. Consequently, DLF1 in dual-frequency (DLF1_DF) and synthesized single-frequency mode (DLF1_SF) provide data throughout the year. For all sites (including the SEID network stations) we are using 30-second data in the Receiver Independent Exchange Format (RINEX).

The SEID processing and subsequent PPP processing are performed by using the open source MATLAB program goGPS version 0.4.3 [26]. This version is based on a for-

Figure 3.1: Positions of the SEID reference stations of the DPGA (red triangles) and EUREF (purple stars) constellations, the experimental setup in Delft (green square) and the AWS (orange cross). The sites DLF1, Geo Monitoring Unit (GMU) and u-blox NEO-M8T evaluation toolkit (UBX) are all co-located within a 10 m^2 area.

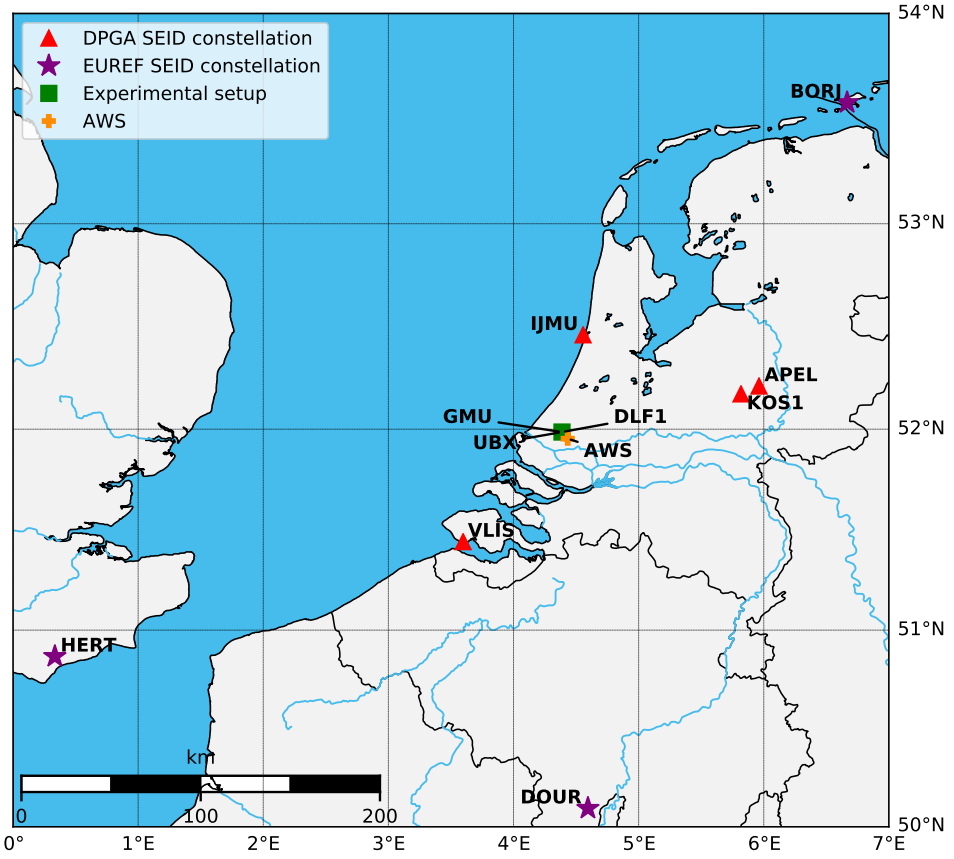

ward Kalman filter approach. During the pre-processing step, cycle-slips are corrected and antenna calibrations, if available, are applied to all stations. An epoch-by-epoch code-only least-squares adjustment is then executed to identify and remove outliers. Observation sets (i.e. code and phase observations for a given satellite) for which the configured residual code observation error threshold is exceeded, are flagged as outliers and removed. Entire epochs are removed if the number of available observation sets is equal or lower than 4, or if the standard deviation of the estimated error exceeds a given threshold. During the PPP processing, an additional outlier detection and removal algorithm is executed, based on a configured threshold on phase post-fit residuals. In this version of goGPS, the PPP Kalman filter is not reset at the day-boundary. This enables a seamless ZTD estimation without spikes at the beginning of each dataset. Both SEID constellation studies and the PPP estimations share the same configuration parameters.

Table 3.1: SEID and ZTD computation settings

Item	Processing strategies
Software	goGPS v. 0.4.3
Observations	GPS-only
Sampling interval	30-second
Processing mode	SEID-PPP
Antenna calibration	IGS (if available)
Troposphere modeling	Saastamoinen (with GPT model)
Troposphere mapping function	GMF
Elevation cutoff	10°
Ocean loading	FES2004
Observation weighting	same weight for all observations
Clock & orbits	IGS Final
Kalman filter reset	no (seamless)
Code observation error threshold	30 m
Phase observation error threshold	0.05 m
Code least-squares est. st. dev. threshold	40 m

Table 3.1 summarizes the settings of our analysis.

After the SEID interpolation on the single-frequency datasets we obtain dual-frequency RINEX files which we process in PPP mode in goGPS. We use data from GPS-only satellites, an elevation cutoff angle of 10 degrees and apply ocean loading effects obtained from the FES2004 model [27]. The IGS antenna calibration, final orbits, 30-second satellite clocks and earth rotation products were used [28]. One should note that the IGS final products are only available with a 12 to 18 day latency. Hence they can only be used for post-processing purposes.

The ZTD estimations are affected by the antenna type and the SEID model. The best possible references for these are calibrated choke ring antennas and dual-frequency PPP estimations. To verify the performance of the goGPS PPP engine, the ZTD estimations are compared to existing reference datasets respectively. The experimental setup provides these references and allows us to validate these aspects.

A first step in our analysis is the comparison of various available ZTD reference datasets from different analysis centers to results obtained for our experimental setup. Specifically, we compare the reference ZTD data from the IGS available from the Crustal Dynamics Data Information System (CDDIS) archive (IGS [29]), Nevada Geodetic Laboratory (NGL [30]) and EPN analysis center outputs [31] from the Federal Agency for Cartography and Geodesy (BKG), Federal Office of Topography (LPT) and Royal Observatory of Belgium (ROB).

3.3. RESULTS

3.3.1. INTER-COMPARISON OF DIFFERENT ZTD REFERENCE DATASETS

ANALYSIS Centers (ACs) provide ZTD estimations for IGS stations worldwide. However, only the IGS and NGL datasets have a 5-minute temporal resolution. The EPN products ROB, LPT and BKG are available in one hour intervals. The reference datasets IGS, BKG, LPT and ROB are based on the Bernese processing engine using the least-squares adjustment method. NGL provides GIPSY/OASIS II ZTD estimations in PPP using a modified Kalman filter. The IGS data is available from the CDDIS archive. The IGS AC updated their processing engine on DOY 29 in 2017 to Bernese 5.2. Table 3.2 summarizes the characteristics of each reference dataset.

Table 3.2: Characteristics of reference datasets of the IGS station DLF1. All products are post-processed results using the final satellite orbit and clock data.

AC	Processing engine	Processing method	Cutoff (°)	Resolution	Missing days
IGS	Bernese 5.0 & 5.2	PPP	7	5 min	10
NGL	GIPSY/OASIS II	PPP	7	5 min	10
BKG	Bernese 5.2	Double-Differences	3	60 min	1
LPT	Bernese 5.3	Double-Differences	3	60 min	4
ROB	Bernese 5.2	Double-Differences	3	60 min	4

Surprisingly not all analysis centers provide data for all dates, whereas the IGS station DLF1 recorded data throughout the selected observation period. As a result, our PPP processed dual- and simulated single-frequency data of DLF1 is characterized by no data gaps. The IGS and NGL datasets show 10 missing days whilst BKG, LPT and ROB only 1 and 4 respectively. It must be noted that these are for the major part not the same dates. We assess the performance of the ZTD estimations by comparing the various reference datasets to each other. The scatter plots of all reference datasets, their corresponding root mean square errors (RMSE), mean biases and standard deviations are depicted in Figure 3.2.

The scatter plots show an RMSE of about 3 mm between the post-processed datasets IGS, NGL, BKG, LPT and ROB. No remarkable bias is observed. The best agreement is found between the 1 hour datasets BKG, ROB and LPT. This is explained by the fact that for the 1 hour datasets individual estimates are based on more measurements compared to the 5-minute datasets, and the fact that the three ACs use a similar processing method. For the comparison with IGS and NGL, we used the timestamps of the 1 hour datasets. The precision of the ZTD estimations between the analysis center outputs are very similar, in the order of 2-4 mm. For this reason we only use the IGS data as a reference to compare the results from our experimental setup. The advantage of the IGS estimations is the 5 minute sampling interval and the high data availability.

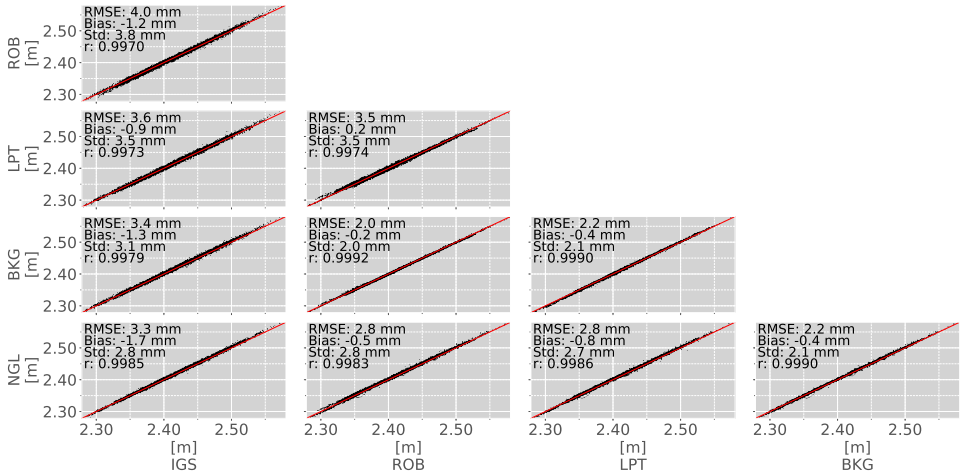

Figure 3.2: ZTD Scatter plots of all post-processed reference datasets at DLF1 in 2017. The solid red line depicts the regression line. RMSE, bias and std values are in millimeter. The r-value depicts the correlation.

3.3.2. SEID-PPP PROCESSED ZTD ESTIMATIONS

AFTER validating the reference data we analyze the results of the goGPS PPP estimations at the experimental setup location for both SEID constellations. Figure 3.3 shows the ZTD scatter plots between the DLF1 dual- (DLF1_DF) and single-frequency (DLF1_SF), GMU, UBX and the selected IGS reference dataset using the DPGA SEID constellation.

The column on the left in Figure 3.3 demonstrates the goGPS PPP software error by comparing the estimations to the IGS reference ZTD dataset. Compared to the IGS reference dataset the goGPS PPP dual-frequency dataset (DLF1_DF) shows an RMSE of 7 mm and bias of 4 mm over the whole year. A bias in the range of 3 - 9 mm is present in the goGPS processed results and negatively influences the RMSE. The scatter plots on the right show the comparisons of the goGPS estimated results among each other. The dual-frequency data (DLF1_DF) and the simulated SEID processed single-frequency data (DLF1_SF) show an RMSE of 4 mm. The GMU yields an RMSE of 6 mm and no notable bias. The UBX dataset is largely characterized by a negative 5 mm bias but similar (5 mm) standard deviation and slightly higher RMSE (7 mm). All goGPS processed datasets yield standard deviations between 4 and 5 mm using the DPGA SEID constellation. Figure 3.4 presents the scatter plots utilizing the EUREF SEID constellation with stations characterized by distances of about 200 - 300 km.

Similar to the layout in Figure 3.3, Figure 3.4 depicts the software error on the left and the experiment results on the right. The bias introduced by the goGPS software remained the same. The RMSE and standard deviation increased to 13/12, 12/12 and 16/13 mm respectively for DLF1_SF, GMU and UBX. A higher scattering effect of the single-frequency datasets (DLF1_SF, GMU and UBX) is evident after the SEID interpolation. Compared to the DLF1_DF reference, both GMU and DLF1_SF are now characterized by an RMSE of 10 mm. UBX shows an RMSE of 12 mm. The bias of the dataset has not changed and is

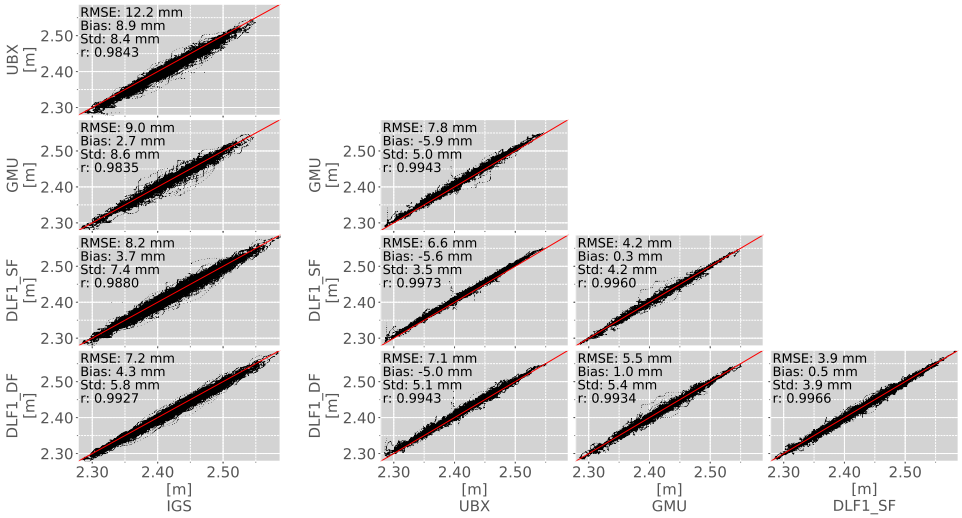

Figure 3.3: ZTD Scatter plots of the IGS reference dataset, the dual-frequency PPP processed DLF1 dataset (DLF1_DF) and the SEID processed single-frequency data from UBX, GMU and DLF1_SF utilizing the DPGA SEID reference network. The plots on the left depict the comparison of the goGPS estimations to the IGS reference dataset. The scatter plots on the right show the SEID and instrument errors. The observation period is from 1 January 2017 (DLF1_DF & DLF1_SF) and 1 September 2017 (GMU & UBX) until 31 December 2017. The solid red line depicts the regression line.

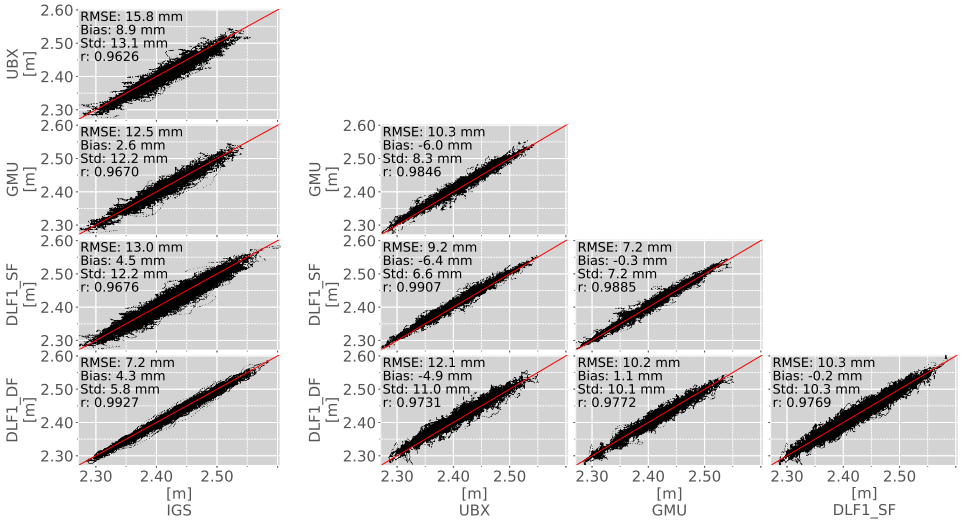

Figure 3.4: ZTD Scatter plots of the reference dataset IGS, the dual-frequency PPP processed DLF1 dataset and the SEID processed single-frequency data from UBX, GMU and DLF1_SF utilizing the EUREF SEID constellation. The plots on the left depict the comparison of the goGPS dual-frequency estimation to the IGS reference dataset. The scatter plots on the right show the SEID and instrument errors. The observation period is from 01 September 2017 until 31 December 2017. The solid red line depicts the regression line.

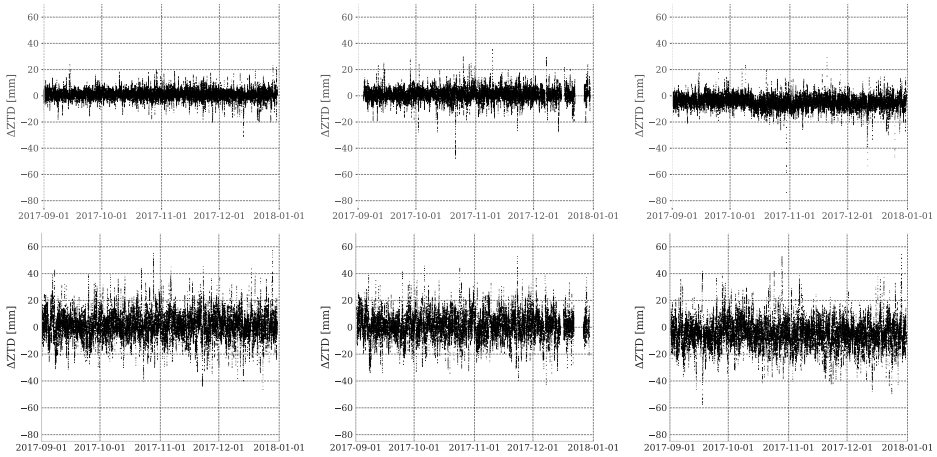

(a) DLF1_SF (b) GMU (c) UBX

Figure 3.5: ZTD differences between the goGPS processed dual-frequency reference dataset and the SEID-processed single-frequency estimations DLF1_SF, GMU and UBX. The Figures at the top depict the DPGA SEID constellation results whilst the ones on the bottom are from the EUREF SEID constellation respectively. DLF1_SF (a) is the synthesized single-frequency dataset obtained from the IGS stations DLF1. GMU (b) and UBX (c) are the two cost-efficient single-frequency receivers utilizing different antenna types but sharing the same receiver type. The comparison period 1 September 2017 - 31 December 2017 was selected since all receivers provide observations during this period.

still present. Among each other the single-frequency datasets yield standard deviations between 7 and 8 mm. Compared to the dual-frequency reference, the standard deviation increased to 10 - 11 mm. Figure 3.5a, b and c show the ZTD differences of the SEID processed (DLF1_SF), GMU and UBX data compared to the reference dual-frequency dataset for the comparison period 1 September 2017 - 31 December 2017.

The differences using the DPGA SEID constellations (top plots in Figure 3.5) generally range between 0 and 10 mm in the DLF1_SF and GMU case. More outliers are visible and generally increased by about 10 mm for the GMU (b) compared to the DLF1_SF (a) case. As depicted in the scatter plots, a clear negative bias is seen for the UBX differences. Contrary to the synthesized dataset (DLF1_SF), the GMU and UBX datasets show an increased amplitude and amount of outliers. The results utilizing the larger SEID reference station distances (bottom plots in Figure 3.5) demonstrate an increased dispersion throughout the comparison period for all sites. Except slightly higher outliers and the previously mentioned bias in the UBX data, no performance decrease is visually evident. Figure 3.6 shows the boxplots to indicate the variability of the single-frequency dataset differences compared to the DLF1_DF reference utilizing both SEID constellations.

The Figure demonstrates that the scattering effect is about the same for all stations using the same SEID constellation. Regarding only the DPGA SEID case (blue boxes), DLF1_SF shows the smallest errors. The scattering effect is also marginally decreased compared to the GMU and UBX case. However, higher outliers in the GMU and UBX datasets are evident. Consistent to the negative UBX bias, the amount of outliers are

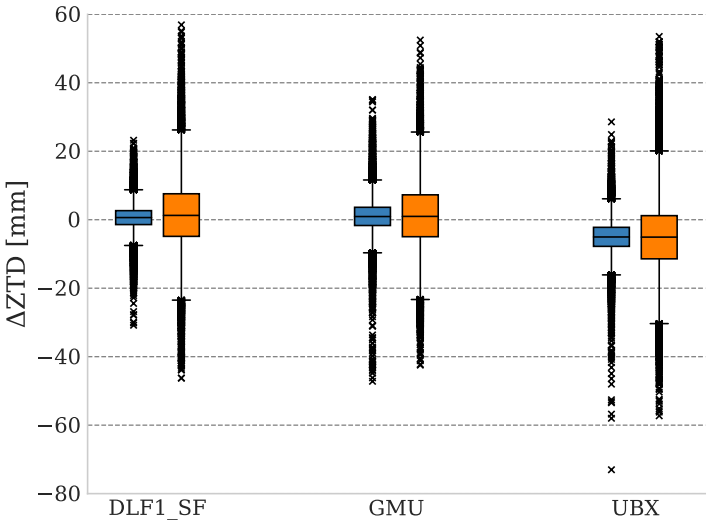

Figure 3.6: Boxplots of the SEID-single frequency ZTD differences to the DLF1_DF reference using the DPGA SEID constellation (blue) and the EUREF reference stations (orange).

predominately negative. Regarding the EUREF SEID case (orange boxes) the variation is rather equivalent for all stations. The bias and slightly increased outliers remain for the UBX case. However, comparing the two SEID cases among each other, a higher variation and more outliers are present. Figure 3.7 shows the ZTD cumulative error distributions of the single-frequency datasets (DLF1_SF, GMU and UBX) to the dual-frequency reference dataset for both SEID cases.

The cumulative error distribution of the DPGA SEID case datasets is depicted in Figure 3.7a. The Figure shows that about 95 % (DLF1_SF) and about 90 % (GMU) of the data points are within 10 mm precision. About 85 % of the UBX data shows an error below 10 mm. Using the larger EUREF SEID station network (Figure 3.7b), a clear degradation is evident. Only 70 % (DLF1_SF, GMU) and 60 % (UBX) of the data show an error below 10 mm compared to the dual-frequency reference. About 95 % of the ZTD estimations from DLF1_SF and GMU are below a 20 mm error range which applies to about 90 % of the UBX data.

To match a PWV quality requirement of 1 - 3 mm precision for application in NWP models [32], we select the threshold of 10 mm ZTD (results in 1 - 2 mm PWV) difference as a valuable input for meteorological applications. Table 3.3 summarizes the statistics of the sites compared to the dual-frequency reference dataset for both SEID cases. Apart from the RMSE, mean bias, correlation, the percentage of datapoints exceeding the 3σ limit and greater than 10 mm ZTD differences are listed. Another quality measure is the amount of data points that were not available, either because they were removed during data processing as outliers, or because they were not recorded by the measuring station.

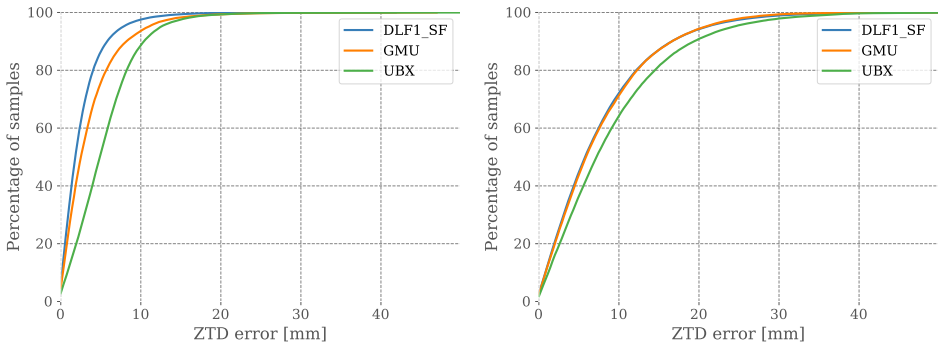

(a) DPGA SEID case

(b) EUREF SEID case

Figure 3.7: Cumulative error distribution plots of the single-frequency ZTD estimations DLF1_SF, GMU and UBX compared to the DLF1_DF reference dataset. The Figure at the left (a) depicts the DPGA SEID constellation results while (b) is from the EUREF SEID case respectively.

Table 3.3: Statistics on the experimental setup data using dual-frequency ZTD estimations as reference. Units of the RMSE, bias and standard deviation σ are depicted in mm.

Case	Site	RMSE [mm]	Bias [mm]	σ [mm]	Corr	%>=3σ
DPGA	DLF1_SF	3.93	0.52	3.90	0.9967	1.64
	GMU	5.55	0.99	5.46	0.9938	1.44
	UBX	7.10	-4.96	5.08	0.9945	2.63
EUREF	DLF1_SF	10.32	-0.20	10.32	0.9769	0.92
	GMU	10.20	1.11	10.14	0.9772	0.62
	UBX	12.09	-4.93	11.04	0.9731	1.38

Case	Site	%>=Δ10 mm	%Missing
DPGA	DLF1_SF	2.61	0.46
	GMU	6.77	7.10
	UBX	12.68	0.87
EUREF	DLF1_SF	29.04	0.28
	GMU	29.87	6.89
	UBX	37.12	0.86

For the DPGA case, the SEID processed DLF1_SF data shows 2.61 % of their data points that exceed the 10 mm threshold. The GMU yields 6.77 % and UBX 12.68 % respectively. The simulated dataset DLF1_SF shows the best performance compared to its dual-frequency counterpart. It shows the lowest RMSE (3.93 mm), bias (0.52 mm) standard deviation (3.90 mm) and yields the highest correlation (0.9967). The GMU is

characterized by a smaller RMSE (5.55 mm) compared to the UBX station (7.10 mm). However, the correlation and standard deviation of UBX slightly outperforms the ones from the GMU. The differences are marginal and may be a coincidence. Different antenna types were used and the GMU is also characterized by more data gaps that are probably the driving factor behind this effect. Another quality decline is observed for the percentage of points exceeding the 3σ limit comparing the GMU and the UBX data. Even though the σ values are about the same, about twice the amount exceeds the 3σ limit at the latter one. A similar effect can be seen by the amount of points that exceed the 10 mm threshold (12.68%). However, this effect is mainly caused by the identified UBX bias. For the UBX dataset, 0.87 % of all data has been rejected as outliers. The GMU site demonstrated a 7.1 % loss of data. Except the bias in the UBX dataset, the UBX site shows a similar standard deviation as the GMU (5.08 and 5.46 mm respectively).

Regarding the EUREF SEID case, the 10 mm threshold is exceeded for about 29 % - 30 % of the data points at the DLF1_SF and GMU datasets. The UBX dataset is not only characterized by the highest RMSE (12.09 mm) and bias (-4.93 mm) but consists also more than 37 % of data that are above the 10 mm threshold. The amount of discarded epochs (NaN values) are almost in the same range as in the first SEID case study. Expectedly, the σ values are higher, in the range of 10 - 11 mm, for all single-frequency solutions. However, the amount of data above the 3σ limit decreased.

3.3.3. PWV COMPUTATION

UTILIZING equation 3.3, a surface temperature error of 10 Kelvin will result into an error of approximately 0.34 percent from the original ZWD (results into an error of up to 1 mm in PWV). Since sea level air pressure is rather homogeneous over a distance of 5 km, we also use the recorded observation at the AWS as input for the ZHD computation. The extrapolation from sea level pressure to the station height is performed using equation 3.6. After subtracting the computed hydrostatic delay from the estimated ZTD, the remaining ZWD is multiplied by the conversion factor. Since the conversion to PWV is performed with the same temperature and air pressure data on the reference ZTD as on the goGPS ZTD estimations, it results into a linear relationship and does not contain any additional information than the original ZTD. Hence, the PWV plots are not shown here. Instead, the PWV RMSE, biases and standard deviations utilizing observations from the nearby AWS for both SEID cases are summarized in Table 3.4.

The PWV estimations from the DPGA (smaller SEID network) show comparable results. The single-frequency stations yield RMSE values of 0.6 mm (DLF1_SF), 0.85 mm (GMU) and 1.05 mm (UBX). The PWV estimations from the EUREF SEID constellation stay below 2 mm RMSE. The priorly identified UBX bias results into about -0.7 mm PWV bias. To distinguish between the receiver, antenna and SEID introduced error, we set up an additional experiment in Italy where we split the signal from a geodetic-grade antenna to three different receiver types.

3.3.4. SPLITTING OF A GEODETIC ANTENNA TO DIFFERENT RECEIVER TYPES (ITALY)

FROM GNSS basics we know that the receiver itself and the antenna quality introduces an error to the estimations. Calibrated antennas to correct for the phase center er-

Table 3.4: RMSE, bias and standard deviation (σ) on the PWV estimation from the SEID processed solutions using the two SEID constellations DPGA and EUREF utilizing temperature and air pressure measurements from the AWS at the Rotterdam airport (5 km distance) compared to the dual-frequency reference.

Case	Site	RMSE [mm]	Bias [mm]	σ [mm]
SEID (DPGA)	DLF1_SF	0.60	0.08	0.59
	GMU	0.85	0.17	0.84
	UBX	1.05	-0.72	0.77
SEID (EUREF)	DLF1_SF	1.61	-0.03	1.61
	GMU	1.60	0.20	1.59
	UBX	1.86	-0.70	1.72

ror improve the obtained results. To further elaborate the influence of the receiver and distinguish between the SEID-introduced and the antenna error, we set up an experiment consisting of a Trimble Zephyr antenna splitted to a GMU (ublox LEA-M8T single-frequency receiver), a Trimble BD930 receiver (geodetic dual-frequency) and an experimental low-cost dual-frequency receiver, developed by Saphyrion Sagl, capable of tracking L1 and L2C signals. The observation period was selected from 9 February 2018 - 17 February 2018. The location of the experimental setup and the SEID-reference stations we are using are depicted in Figure 3.8.

GRTR is the dual-frequency reference station, GRED is the u-blox LEA-M8T single-frequency receiver (same as GMU from the prior experiments) and SAPH is the experimental low-cost dual-frequency receiver. All units obtain the same antenna input signal from the geodetic GRTR antenna, through a GPS Source 4-way splitter. For our analysis we are utilizing the SEID reference stations LUIN, PAV2 and CATU. They are part of the NetGEO [33] network and are located within 10 - 50 km from the experimental setup. After synthesizing a single-frequency dataset from GRTR (GRTR_SF), we apply the SEID algorithm to the single-frequency datasets (GRTR_SF and GRED). On all datasets the PPP is performed to obtain ZTD estimations at the locations. Contrary to the previous computations, this analysis is using goGPS version 0.6.0 which is based on a joint least-squares adjustment. Figure 3.9 depicts the differences between selected time series.

Figure 3.9a shows the differences between the synthesized dataset GRTR_SF and its dual-frequency counterpart GRTR_DF. A bias of 1.99 mm and an RMSE of 2.40 mm is present. The comparison between the geodetic grade GRTR_DF and the experimental cost-efficient dual-frequency receiver (Figure 3.9b) yields an RMSE of 1.58 mm. No significant bias is visible. Figure 3.9c shows the differences between the SEID-generated single-frequency ZTD estimations (GRTR_SF and GRED_SF). The comparison yields an RMSE of 0.20 mm.

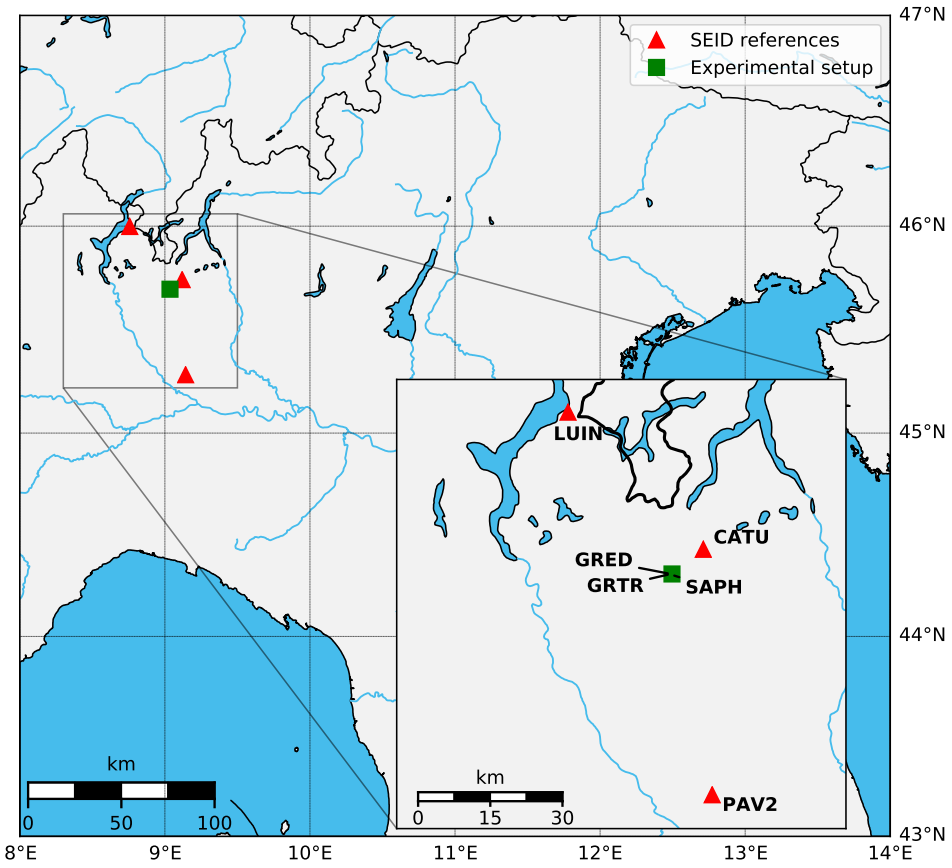

Figure 3.8: Positions of the Italy-experiment SEID reference stations constellation (red triangles) and experimental setup (green square). The sites GRTR, GRED and SAPH use the same Trimble Zephyr 2 antenna (TRM55971.00). GRTR is the dual-frequency receiver reference (Trimble BD930 receiver), GRED the cost-efficient single-frequency device (u-blox) and SAPH a low-cost experimental dual-frequency receiver.

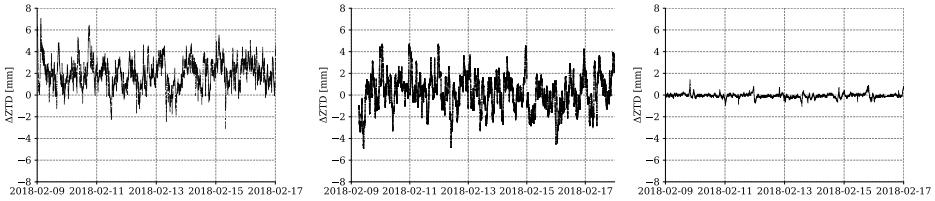

(a) GRTR_SF - GRTR_DF (b) GRTR_DF - SAPH_DF (c) GRTR_SF - GRED_SF

Figure 3.9: ZTD differences between GRTR_SF and GRTR_DF (a), GRTR_DF and SAPH_DF (b) and GRTR_SF - GRED_SF (c). The GRTR_SF and GRED_SF estimations are based on the SEID algorithm whilst GRTR_DF and SAPH_DF use PPP-only.

3.4. DISCUSSION

INTER-COMPARISON OF REFERENCE DATASETS AND ANALYSIS OF THE SOFTWARE RELATED ERROR

FOR the IGS network stations, various ZTD reference datasets from different providers are available. In our experiment we conducted an inter-comparison between 5 analysis center outputs. The results depict a very good agreement between these yielding standard deviations between 2 and 4 mm. The variation between the reference datasets corresponds well to the uncertainty of 4 mm of the IGS troposphere products compared to other independent measurement techniques like radiosondes or numerical weather models [28]. However, the goGPS processed results highlight differences between the goGPS PPP estimations and the available ZTD reference datasets. In our experiment, the goGPS PPP version introduced a 4 mm ZTD bias to the dual-frequency PPP solution. A part of this error may be caused by using a 10 degree elevation cut-off angle instead of 7 degrees as used in the IGS reference dataset. The comparison between the PPP-only (DLF1_DF) and the IGS dataset demonstrated an RMSE of 7 mm. This effect is mainly caused by the software-introduced bias and exceeds the 4 mm error range by the IGS troposphere products. It suggests that there is still room for improvements to the processing engine. However, the software is continuously developing and the results are constantly improved by implementing additional model functions. In the upcoming release, the processing will switch from using a Kalman filter to a joint least-squares adjustment. This version is currently in an experimental phase. However, initial results (see subchapter 3.3.4) from the least-squares version suggest a significant improvement of the ZTD estimation accuracy. Even though the original dual-frequency ZTD estimations are subject to be improved by utilizing another PPP analysis tool, driven by the observed ZTD variation the results suggest that the goGPS estimations can be used to representatively compare the ZTD estimations among each another. Using a different processing engine will not significantly influence the investigated variations.

SEID DPGA EXPERIMENT AND ANTENNA IMPACT

THE conducted SEID experiment using the DPGA constellation with distances between 50 and 80 km demonstrate the successful application to our domain. The RMSE of 4 mm between the DLF1_SF and its dual-frequency counterpart validate the results from prior studies by e.g. Deng *et al.* [14]. DLF1_DF and DLF1_SF use the same geodetic-grade antenna and antenna phase center corrections. Since they share the same receiver, antenna and configuration parameters, the error between these two is entirely introduced by the SEID network interpolation and demonstrates a reasonable accuracy. The error may be introduced by loss of lock, cycle-slips or the irregular nature of the ionosphere. The ZTD results from the newly placed single-frequency stations GMU and UBX are generally more noisy. The GMU, being equipped with a Tallysman antenna and u-blox LEA-M8T receiver, demonstrated a slight performance decrease compared to the synthesized dataset. The GMU contains less data points than the UBX device, because especially at the end of the year, the GMU suffered of some technical problems caused by the insufficient power supply generated by the solar panels during winter. GMU and UBX are equipped with a similar receiver type (respectively u-blox LEA-M8T

and u-blox NEO-M8T), are co-located and use the same ionosphere correction sources. However, the UBX site is affected by a systematic bias (about 6 mm) which is presumably caused by an increased multipath effect due to the lower quality antenna. This suggests that the antenna type and placement has a major influence on the precision. Pesyna *et al.* [34] report that patch antennas are characterized by a less effective signal reception and suffer more from multipath effects than geodetic-grade antennas. The antenna is a simple patch antenna and shielded by a metal plate on the ground. The horizontal placement on the rooftop may be a reason for this effect. The DPGA SEID experiment demonstrated a successful application of the SEID model to single-frequency receivers with standard deviations of the ZTD error between 4 and 5 mm. A decrease of the outer network station distance using an even denser network (e.g. the Japanese GEONET or using commercial existing GNSS networks) could even further improve the results. However, not all regions of the Earth provide such a dense network of dual-frequency GNSS receivers such as Europe, North America or Japan. Areas that will benefit most by a densification with cost-efficient single-frequency receivers are often characterized by a much coarser reference network.

SEID EUREF Experiment

Utilizing the EUREF stations with distances between 200 and 300 km as SEID references allowed us to experimentally investigate the impact of significantly longer station distances on the ZTD estimations. The comparison between DLF1_DF and DLF1_SF depicts the ionospheric error and yields an RMSE of 10 mm. The overall character of the data shows more variation, which results in less outliers. The results also suggests that the GMU reaches a similar precision as the DLF1_SF dataset. However, the GMU and UBX stations have data only available from 01.09.2017 onwards whereas the DLF1_SF provides data throughout the year. The higher ZTD values in summer are missing for GMU and UBX. A decrease of these stations performance may apply if the full observation period is considered. The majority of the outliers at the experimental setup are presumably caused by hardware errors, inconsistencies during the pre-processing (e.g. undetected cycle-slips during the SEID processing), re-initializations of the Kalman filter after missing epochs and by the interpolation of the ionospheric component. The higher outliers are especially present at epochs with higher re-initialization rates that are caused by power-problems of the GMU. The GMU shows a slightly reduced removal of epochs (6.89 %) compared to the DPGA case, which is presumably caused by less abrupt changes in ZTD estimations. For this large reference network, it demonstrates that the limiting factor of the precision of the ZTD estimations is rather the ionospheric interpolation than the hardware quality. We expect that the GMU will provide comparable results with almost the same precision as the synthesized dataset since the noise introduced by the SEID model will dominate the estimations. This experiment shows that the SEID algorithm is able to provide ZTD estimations even over a SEID network with distances between 200 and 300 km to the single-frequency setup in a mid-latitude region. However, the ZTD RMSE of 10 - 12 mm compared to the dual-frequency estimation is just barely acceptable for the post-processed water vapor estimation.

PWV ESTIMATIONS

AN additional error is introduced by the conversion from ZTD to PWV by utilizing temperature and pressure data. Without co-located temperature and air pressure measurements, data from weather models may be used (e.g. Jiang *et al.* [35]). In this study we use observations from a nearby weather station. Due to the small distance of about 5 km and almost negligible height differences, a linear interpolation of the temperature is sufficient. However, the heterogeneous character of surface temperature caused e.g. by effects like the urban heat island will result in an additional PWV uncertainty. Having achieved PWV RMSE values between 0.6 - 1.05 mm (DPGA case) and 1.61 - 1.86 mm (EUREF case) compared to the dual-frequency reference, it must be highlighted that especially the errors from GMU and UBX are subject to increase since the summer period is missing in the analysis. The results show that cost-efficient single frequency devices may provide beneficial PWV estimations over areas with up to 300 km SEID reference station distances. Such an application may be especially interesting for regions with limited investment capabilities and areas that show a high PWV variability and no or only very few available PWV in-situ data. Extending existing tropical GNSS monitoring networks like the Continuously Operating Caribbean GPS Observational Network (COCONet) or the Amazon Dense Network [36] could potentially improve the monitoring and forecasting of deep tropical convection. However, especially the geomagnetic anomaly over South America and equatorial regions are characterized by a stronger and more turbulent ionosphere than mid-latitudes. Additional research is required to evaluate the applicability of the SEID algorithm for such regions.

ANTENNA SPLITTING

THE conducted antenna splitting experiment allowed us to distinguish between the SEID-introduced and the hardware errors. The results suggest that the experimental goGPS version (version 0.6.0) overall improved the ZTD estimation and the introduced bias was reduced. Initialization times at the day-boundaries are smoothed by buffering 3 hours before and after each daily file. Figure 3.9a demonstrates that the bias in this case is introduced by the SEID implementation. The differences illustrate entirely the error that is introduced by the SEID implementation. Compared to the DPGA and EUREF experiments, the reduced variation of the ZTD estimations results partly from the version change and partly by the decreased SEID station distances. However, correcting the mean bias will improve the RMSE significantly. The cost-efficient dual-frequency SAPH_DF station yields an RMSE of 1.58 mm. The most notable characteristic about the SAPH_DF station is that it is only able to track up to 8 GPS satellites simultaneously since it is limited by the amount of concurrent receiving channels. The ZTD deviation is introduced by the decreased receiver quality and by a less optimal satellite geometry due to the fact that only up to 8 satellites on two frequencies may be observed. Difficult environmental conditions e.g. increased multipath may even further decrease the quality. Since the same ionosphere correction, antenna data and pattern correction is used for GRTR_SF and GRED_SF, the Figure 3.9c illustrates the receiver clock and phase ambiguity error. It clearly demonstrates that low-cost single-frequency receivers are capable to track satellite signals with almost identical precision to geodetic-grade receivers. This suggests that the precision of the single-frequency units for ZTD estimations is foremost

dependent on the correct modeling of the ionosphere and the antenna type.

3.5. CONCLUSION

HIGHER spatial resolution of water vapor measurements is required for the observation of smaller scale convective events [37]. Prior studies e.g. by [10] demonstrate a positive impact using a high resolution GNSS-based PWV network on the rainfall forecast accuracy. The objective of this work was to evaluate the feasibility of a densification of existing GNSS networks with cost-efficient single-frequency GNSS receivers. In this study we analyzed one year of GNSS data. We first compared the available ZTD reference datasets with each other at the experimental setup location. Secondly, we validated the ZTD estimations at our experimental setup using two different SEID reference networks and indicated the potential for PWV monitoring. Furthermore, we conducted an additional observation campaign to distinguish between the hardware and the SEID introduced errors.

We experimentally verified that the applied SEID model is able to successfully be used for water vapor estimations using cost-efficient single-frequency receivers. A clear precision degradation linked to the increasing outer network station distances was found. The SEID processed synthesized dataset (DFL1_SF) demonstrated a ZTD RMSE of 3.93 and 10.32 mm for station distances of up to 80 and 300 km respectively. The cost-efficient unit (GMU) indicates comparable results with RMSE values of 5.55 and 10.20 mm. The precision further decreased by the utilization of a simple patch antenna (station UBX) to 7.10 and 12.09 mm RMSE. A clear bias of -4.96 mm presumably caused by the antenna type or an increased multipath effect has been observed for this receiver. Our analysis also highlighted a systematic ZTD bias of about 4 mm caused by the used goGPS version 0.4.3 compared to existing ZTD reference datasets. However, apart from the bias, the precision of the PPP ZTD estimations are found reliable.

The additional antenna splitting experiment conducted in Italy using the newest goGPS version 0.6.0 demonstrated a significant improvement to the ZTD estimation. However, the decreased SEID reference station distance also positively affected the ZTD errors. A ZTD RMSE of 2.40 mm has been found for the synthesized single-frequency dataset (GRTR_SF) compared to its dual-frequency counterpart. A cost-efficient dual-frequency receiver that tracks only a limited number of satellites showed an RMSE of 1.58 mm in ZTD. Using only few satellites, the satellite geometry deteriorates and the ZTD estimation may be negatively influenced. The experiment demonstrated that using the SEID model, cost-efficient single-frequency receivers are able to provide ZTD estimations with almost negligible differences.

The study demonstrated that cost-efficient single-frequency receivers can serve as a promising complement to the presently available GNSS networks in mid-latitude regions. Cost-efficient single-frequency stations like the GMU used in this analysis are in operational use since the end of 2015. Historical data about the longevity for these recently designed units is not yet available. However, fulfilling certified industrial standards for protection against sand, dust and water provide the best conditions for a long durability of the stations. In the framework of the TWIGA project [38], a network of such GMUs will be deployed in equatorial regions in Africa. The aim is to investigate the durability in more challenging environments and how the SEID model will perform in the

equatorial region with more turbulent ionospheric conditions. The conducted experiments also demonstrate that the ZTD precision from single-frequency receivers is foremost dependent on the modeling of the ionosphere and the antenna type than on the internal hardware. However, the application of other ionospheric correction models is not discussed in detail in this analysis and a comparison to different ionospheric models must be considered for future studies.

Further work is required to utilize the multi-GNSS ability of the receivers for the SEID approach. Additional satellites combined with a denser network of GNSS receivers may be useful for GNSS-based 3D tomography. Especially GNSS tomography can be improved by using a multi-GNSS approach [39]. It has to be highlighted that all shown results are post-processed PPP-solutions available with a temporal delay of at least two weeks. For an effective weather forecasting, the data needs to be available in near-real time (NRT). The use of multi-GNSS PPP utilizing NRT data from the IGS has been studied by Lu *et al.* [40]. Compared to the GPS-only mode, they were able to improve the accuracy of ZTD estimations by up to 22.2 %.

Densified PWV networks may be used to improve the long-term accuracy of weather models, for climate analysis or improving model calibrations. They can be beneficial to study particular weather events at particular sites or on a regional scale. In the framework of BRIGAID, the Rotterdam study area (Netherlands) allows us to make use of additional existing dual-frequency stations within the city borders. The decreased reference station distances are expected to improve the ionospheric modeling and to result into better PWV estimations. The target of our future work is to study the spatial variability of single-frequency based PWV estimations and to analyze its impact on monitoring and forecasting of convective events in that area. For this purpose, we installed a follow-up experimental single-frequency network consisting of four additional receivers.

REFERENCES

[1] J. T. Kiehl and K. E. Trenberth, *Earth's Annual Global Mean Energy Budget,* Bulletin of the American Meteorological Society **78**, 197 (1997).

[2] D. Andrews, *An Introduction to Atmospheric Physics*, International geophysics series (Cambridge University Press, 2000).

[3] H. Seko, H. Nakamura, Y. Shoji, and T. Iwabuchi, *The meso-y scale water vapor distribution associated with a thunderstorm calculated from a dense network of GPS receivers,* Journal of the Meteorological Society of Japan **82**, 569 (2004).

[4] R. D. Cess, G. L. Potter, J. P. Blanchet, G. J. Boer, A. D. Del Genio, M. Déqué, V. Dymnikov, V. Galin, W. L. Gates, S. J. Ghan, J. T. Kiehl, A. A. Lacis, H. Le Treut, Z.-X. Li, X.-Z. Liang, B. J. McAvaney, V. P. Meleshko, J. F. B. Mitchell, J.-J. Morcrette, D. A. Randall, L. Rikus, E. Roeckner, J. F. Royer, U. Schlese, D. A. Sheinin, A. Slingo, A. P. Sokolov, K. E. Taylor, W. M. Washington, R. T. Wetherald, I. Yagai, and M.-H. Zhang, *Intercomparison and interpretation of climate feedback processes in 19 atmospheric general circulation models,* Journal of Geophysical Research: Atmospheres **95**, 16601 (1990).

[5] T. Ning, J. Wang, G. Elgered, G. Dick, J. Wickert, M. Bradke, M. Sommer, R. Querel, and D. Smale, *The uncertainty of the atmospheric integrated water vapour estimated from GNSS observations,* Atmospheric Measurement Techniques **9**, 79 (2016).

[6] Y.-H. Kuo, X. Zou, and Y.-R. Guo, *Variational assimilation of precipitable water using a nonhydrostatic mesoscale adjoint model. Part I: Moisture retrieval and sensitivity experiments,* Monthly Weather Review **124**, 122 (1996).

[7] K. Sato, E. Realini, T. Tsuda, M. Oigawa, Y. Iwaki, Y. Shoji, and H. Seko, *A high-resolution, precipitable water vapor monitoring system using a dense network of GNSS receivers,* Journal of Disaster Research **8**, 37 (2013).

[8] E. Realini, K. Sato, T. Tsuda, M. Oigawa, Y. Iwaki, Y. Shoji, and H. Seko, *Local-scale precipitable water vapor retrieval from high-elevation slant tropospheric delays using a dense network of GNSS receivers,* in *IAG 150 Years* (2015) pp. 485–490.

[9] GNSS Earth Observation Network System, *GEONET,* `http://datahouse1.gsi.go.jp/terras/terras_english.html` (2018), accessed: 2018-09-12.

[10] M. Oigawa, T. Tsuda, H. Seko, Y. Shoji, and E. Realini, *Data assimilation experiment of precipitable water vapor observed by a hyper-dense GNSS receiver network using a nested NHM-LETKF system,* Earth, Planets and Space **70**, 74 (2018).

[11] Z. Baldysz, G. Nykiel, M. Figurski, and A. Araszkiewicz, *Assessment of the Impact of GNSS Processing Strategies on the Long-Term Parameters of 20 Years IWV Time Series,* Remote Sensing **10**, 496 (2018).

[12] Z. Deng, M. Bender, G. Dick, M. Ge, J. Wickert, M. Ramatschi, and X. Zou, *Retrieving tropospheric delays from GPS networks densified with single frequency receivers,* Geophysical Research Letters **36** (2009), 10.1029/2009GL040018.

[13] J. Zumberge, M. Heflin, D. Jefferson, M. Watkins, and F. Webb, *Precise point positioning for the efficient and robust analysis of GPS data from large networks,* Journal of Geophysical Research B: Solid Earth **102**, 5005 (1997).

[14] Z. Deng, M. Bender, F. Zus, M. Ge, G. Dick, M. Ramatschi, J. Wickert, U. Lhnert, and S. Schön, *Validation of tropospheric slant path delays derived from single and dual frequency GPS receivers,* Radio Science **46** (2011), 10.1029/2011RS004687.

[15] GeoGuard Earth Monitoring Services, *GeoGuard earth monitoring services,* `http://www.geoguard.eu/` (2018), accessed: 2018-05-16.

[16] G. Thayer, *An improved equation for the radio refractive index of air,* Radio Science **9**, 803 (1974).

[17] J. Saastamoinen, *Contributions to the theory of atmospheric refraction,* Bulletin Géodésique **46**, 279 (1972).

[18] M. Bevis, S. Businger, T. A. Herring, C. Rocken, R. A. Anthes, and R. H. Ware, *GPS meteorology: Remote sensing of atmospheric water vapor using the global positioning system,* Journal of Geophysical Research: Atmospheres **97**, 15787 (1992).

[19] H. K. Baltink, H. Van Der Marel, and A. G. van der Hoeven, *Integrated atmospheric water vapor estimates from a regional GPS network,* Journal of Geophysical Research: Atmospheres **107** (2002).

[20] M. Bevis, *GPS meteorology: mapping zenith wet delays onto precipitable water,* Journal of Applied Meteorology **33**, 379 (1994).

[21] N. K. Pavlis, S. A. Holmes, S. C. Kenyon, and J. K. Factor, *An earth gravitational model to degree 2160: EGM2008,* EGU General Assembly **10**, 13 (2008).

[22] M. N. Berberan-Santos, E. N. Bodunov, and L. Pogliani, *On the barometric formula,* American Journal of Physics **65**, 404 (1997).

[23] S. Schaer, *Mapping and predicting the Earth's ionosphere using the Global Positioning System.* Geod.-Geophys. Arb. Schweiz, Vol.59 **59** (1999).

[24] E. Araujo-Pradere, T. Fuller-Rowell, P. Spencer, and C. Minter, *Differential validation of the US-TEC model,* Radio Science **42** (2007).

[25] L. H. Estey and C. M. Meertens, *Teqc: The multi-purpose toolkit for gps/glonass data,* GPS Solutions **3**, 42 (1999).

[26] A. M. Herrera, H. F. Suhandri, E. Realini, M. Reguzzoni, and M. C. de Lacy, *gogps: open-source matlab software,* GPS Solutions **20**, 595 (2016).

[27] F. Lyard, F. Lefevre, T. Letellier, and O. Francis, *Modelling the global ocean tides: modern insights from FES2004,* Ocean dynamics **56**, 394 (2006).

[28] J. Dow, R. Neilan, and C. Rizos, *The International GNSS Service in a changing landscape of Global Navigation Satellite Systems,* Journal of Geodesy **83**, 191 (2009).

[29] C. E. Noll, *The Crustal Dynamics Data Information System: A resource to support scientific analysis using space geodesy,* Advances in Space Research **45**, 1421 (2010).

[30] G. Blewitt, *Ftp archive of ngl troposphere delay products,* `ftp://gneiss.nbmg.unr.edu/trop` (2018), accessed: 2018-05-16.

[31] EUREF Permanent GNSS Network, *Routine Zenith Path Delay archive,* `http://epncb.eu/_productsservices/troposphere/` (2018), accessed: 2018-05-16.

[32] S. de Haan, *National/regional operational procedures of GPS water vapour networks and agreed international procedures,* Tech. Rep. (World Meteorological Organization, 2006).

[33] Topcon Positioning Italy, *NetGEO,* `http://www.netgeo.it/` (2018), accessed: 2018-05-28.

[34] K. M. J. Pesyna, W. H. J. Robert, and T. E. Humphreys, *Centimeter positioning with a smartphone-quality GNSS antenna,* in *Proceedings of the ION GNSS+ Meeting* (2014).

[35] P. Jiang, S. Ye, D. Chen, Y. Liu, and P. Xia, *Retrieving precipitable water vapor data using GPS zenith delays and global reanalysis data in China,* Remote Sensing **8**, 389 (2016).

[36] D. K. Adams, R. M. Fernandes, E. R. Kursinski, J. M. Maia, L. F. Sapucci, L. A. Machado, I. Vitorello, J. F. G. Monico, K. L. Holub, S. I. Gutman, *et al.*, *A dense GNSS meteorological network for observing deep convection in the Amazon,* Atmospheric Science Letters **12**, 207 (2011).

[37] S. Barindelli, E. Realini, G. Venuti, A. Fermi, and A. Gatti, *Detection of water vapor time variations associated with heavy rain in northern Italy by geodetic and low-cost GNSS receivers,* Earth, Planets and Space **70**, 28 (2018).

[38] Transforming Weather Water data into value-added Information services for sustainable Growth in Africa, *TWIGA,* `http://twiga-h2020.eu/` (2018), accessed: 2018-09-12.

[39] Z. Dong and S. Jin, *3-D Water Vapor Tomography in Wuhan from GPS, BDS and GLONASS Observations,* Remote Sensing **10**, 62 (2018).

[40] C. Lu, X. Chen, G. Liu, G. Dick, J. Wickert, X. Jiang, K. Zheng, and H. Schuh, *Real-Time Tropospheric Delays Retrieved from Multi-GNSS Observations and IGS Real-Time Product Streams,* Remote Sensing **9**, 1317 (2017).

4

High Quality Zenith Tropospheric Delay Estimation Using a Low-Cost Dual-Frequency Receiver and Relative Antenna Calibration

The recent release of consumer-grade dual-frequency receivers sparked scientific interest into use of these cost-efficient devices for high precision positioning and tropospheric delay estimations. Previous analyses with low-cost single-frequency receivers showed promising results for the estimation of Zenith Tropospheric Delays (ZTDs). However, their application is limited by the need to account for the ionospheric delay. In this paper we investigate the potential of a low-cost dual-frequency receiver (U-blox ZED-F9P) in combination with a range of different quality antennas. We show that the receiver itself is very well capable of achieving high-quality ZTD estimations. The limiting factor is the quality of the receiving antenna. To improve the applicability of mass-market antennas, a relative antenna calibration is performed, and new absolute Antenna Exchange Format (ANTEX) entries are created using a geodetic antenna as base. The performance of ZTD estimation with the tested antennas is evaluated, with and without antenna Phase Center Variation (PCV) corrections, using Precise Point Positioning (PPP). Without applying PCVs for the low-cost antennas, the Root Mean Square Errors (RMSE) of the estimated ZTDs are between 15 mm and 24 mm. Using the newly generated PCVs, the RMSE is reduced significantly to about 4 mm, a level that is excellent for meteorological applications. The standard U-blox ANN-MB-00 patch antenna, with a circular ground plane, after correcting the phase pattern

This chapter has been published as: Krietemeyer, A.; van der Marel, H.; van de Giesen, N.; ten Veldhuis, M.-C. High Quality Zenith Tropospheric Delay Estimation Using a Low-Cost Dual-Frequency Receiver and Relative Antenna Calibration. Remote Sens. **2020**, 12, 1393.

yields comparable results (0.47 mm bias and 4.02 mm RMSE) to those from geodetic quality antennas, providing an all-round low-cost solution. The relative antenna calibration method presented in this paper opens the way for wide-spread application of low-cost receiver and antennas.

4.1. INTRODUCTION

THE use of Global Navigation Satellite Systems (GNSS) data is well established for a range of professional and scientific applications, including atmospheric research. Precipitable Water Vapor (PWV) can be derived from radiosonde measurements, but also estimated with GNSS phase measurements processing techniques [1]. Zenith Tropospheric Delays (ZTDs) are estimated along with other parameters, such as the station position and receiver clock offset. The estimated ZTD is related to the refractive index of air, it can be used directly in atmospheric models, or ZTD can be used to estimate PWV. These values are of essential interest for accurate short-term weather forecasts.

The use of cost-efficient GNSS equipment is of great scientific interest to meteorology and atmospheric research. Traditionally, atmospheric research and meteorology made use of already existing GNSS infrastructures which were set-up for surveying and geodetic applications. Therefore, low-cost GNSS equipment can be a good solution for regions where (commercial) high grade equipment is not readily available.

Analysing ZTDs or PWV from GNSS receivers has proven to be a valuable tool for analysing and forecasting extreme rainfall events [2]. Nowadays Numerical Weather Prediction (NWP) models exist that use these parameters in their data assimilation schemes to improve their rainfall predictions [3]. To estimate ZTD at existing GNSS receivers on the ground, numerous Analysis Centers (ACs) apply techniques such as Double-Differenced (DD) processing of large GNSS networks, or, the stand-alone Precise Point Positioning (PPP) technique [4]. In contrast to network or relative positioning strategies in general, PPP uses undifferenced GNSS observations and relies on precise satellite clock and positions to be available from the International GNSS Service (IGS). Dual-frequency observations are used to form the ionosphere-free linear combination, which removes the majority of the error associated with the delay in the ionosphere layer, but increases the noise by a factor of 3 [5]. In the past, estimating ZTD for meteorological purposes using cost-efficient equipment was only possible with single-frequency receivers, which required interpolation of the ionospheric delay from a network of dual frequency receivers (e.g. [6], [7]). Recently, also low-cost dual-frequency receivers became available, which in combination with low-priced antennas, inspired the experiment in this paper. This experiment aims to investigate the potential use of low-cost dual-frequency receivers for ZTD estimation, something that was formerly only possible using expensive receiver equipment, or relying on existing geodetic networks to perform corrections. For this experiment different quality antennas, ranging from geodetic to mass-market, are deployed consecutively on a short-baseline. The new low-cost design of the receiver supplemented by a low-cost antenna may enable the cost-efficient estimation of high-quality tropospheric delays.

For high-precision applications both satellite and receiver antenna corrections need to be applied [8]. These corrections are not only frequency dependent, but they also depend on the azimuth and elevation of the transmitting satellite. The delay caused by the antenna and the near field environment is not the same in every direction. Neither is it possible to find, for a specific frequency, a single point in the antenna for which the delay is the same for every direction. Therefore, a geometric center is something that does not really exists, and concepts like Antenna Phase Center (APC) are only approximate. These variations in antenna delay cause errors in the horizontal and vertical

position, but also in the ZTD estimation. In order to correct the carrier phase signals for this effect, antenna calibrations are performed. The result of an antenna calibration is represented by a Phase Center Offset (PCO) with respect to a chosen Antenna Reference Point (ARP), and azimuth- and elevation dependent Phase Center Variations (PCV) with respect to the PCO. PCV and PCO corrections are provided per frequency. They are not independent, and should always be used together in high-precision positioning applications. Applications that require less precision can use only PCO values. On the other hand, for ZTD estimation, the PCO values are not important, and only the PCV values matter.

To obtain PCO and PCV corrections, relative and absolute antenna calibrations can be used. Absolute calibrations are typically expensive and involve sending the antenna to a calibration facility, while a relative calibration can be performed more easily by yourself. The relative calibration is performed over a short baseline, with on one side the antenna to be calibrated, and on the other side a reference antenna that has already been calibrated before (see e.g. [9]). Double-differenced carrier phase residuals are used to compute the relative pattern between the antenna's. It uses the fact that over short baselines for DD observations most errors (e.g. satellite clock and atmospheric delays) are eliminated. The drawback of this calibration method is that it is a relative calibration. Since 2006 [10] it is common for geodetic applications to use absolute antenna calibrations. Therefore, to obtain an absolute calibration for our antenna, we must add the absolute calibration for the reference antenna to the relative calibration. Absolute calibrations are typically obtained from measurements in an anechoic chamber (see e.g. [11] or [12]) or robotic field calibrations (see [13]). Robotic calibrations have the advantage that they are not affected by multipath effects as in a relative correction.

While high quality geodetic antennas are typically manufactured with highest precision to enable the repetition of phase patterns on the receiving phase center, this is only partially the case for low-cost antennas. Companies specialized in antenna calibrations, such as Geo++ [14] in Germany, generate individual absolute antenna calibrations for geodetic antennas. Absolute antenna calibrations are typically supplied in an Antenna Exchange Format (ANTEX) file [15] that contains PCO as well as azimuth- and elevation dependent PCV for different frequencies and satellite systems. Various individual calibrations of the same antenna type are averaged to type mean calibrations and distributed, such as by the IGS. Using these antenna patterns is a standard practice in geodesy and essential for high precision positioning and also for tropospheric delay estimations. Several studies were performed that compare the differences between type mean and individual antenna phase center calibrations e.g. by Araszkiewicz and Völksen (2016) [16], Schmid et al. 2005 [17] and Sidorov and Teferle 2016 [18]. They found a typical difference of only 2 mm horizontal and up to 4 mm vertical between type mean and individual antenna calibrations. For one antenna an offset of up to 17 mm in the vertical and 10 mm in the horizontal direction was observed. The vertical positioning performance gives an indication about the accuracy of the troposphere estimations since both parameters are correlated [19]. Only few studies were performed that analyze the impact of the antenna PCV on tropospheric parameter estimations. Ejigu et al. 2018 [20] investigated the impact of individual and type mean calibrations on Zenith Wet Delays (ZWDs) and tropospheric gradients [21]. They report a mean ZWD bias of 1.8 mm. A

study by Pacione et al. 2017 [22] demonstrate similar results with ZTD errors in the mm range between utilizing individual and type mean calibrations.

The low-cost GNSS chips, being affordable and produced for the mass-market, are also of interest for scientific applications, but this only makes sense if also a low-cost antenna can be used. Geodetic antennas are generally characterized by special manufactured designs (e.g. choke ring) to suppress multipath induced effects. With low-cost antennas this is typically not the case. An analysis of low-cost antennas is especially important since they are expected to be particularly prone to multipath effects that are reflected in the antenna phase patterns.

In this paper we investigate the PPP ZTD performance of a recently introduced low-cost dual-frequency receiver connected to antennas of ranging quality (geodetic to mass-market) with and without applying relative antenna calibrations. Additionally, using L1-only data we investigate how well the (un-)corrected single-frequency data from the dual-frequency receiver can be used for meteorological applications. This is achieved by trimming the original data to L1-only datasets and generating a second frequency observation with the Satellite-specific Epoch-differenced Ionospheric Delay (SEID) model which is adjusted to the ionospheric delay based on a surrounding dual-frequency network. The paper is structured as follows: Section 2 describes the methodology, experimental setup and data analysis, Section 3 illustrates the PPP-derived ZTD results, Section 4 the discussion and 5 the conclusion.

4.2. METHODS

OUR experiment includes several steps to estimate the impact of different quality antennas on the ZTD performance using a low-cost dual-frequency receiver. The fundamental step upon which our investigation is based on is a short-baseline analysis to perform a relative antenna calibration. Thereafter, different relative antenna calibration results are evaluated using the ZTD from two different PPP experiments. The experimental setup and overview of the data analysis procedure are described in Subsections 2.1 and 2.2. The antenna calibration procedure is explained in Subsection 2.3. Subsection 2.4 describes the evaluation of the ZTD estimations with dual-frequency data in more detail. The antenna calibration impact on single-frequency data is covered in Subsection 2.5.

4.2.1. EXPERIMENTAL SETUP

This subsection describes the test site, instrument setup, data handling as well as the receivers and antennas that were used in the experiment.

Our experiment consists of a series of consecutive short-baseline experiments using the International GNSS Service (IGS) station DLF1 as a base station and a U-blox ZED-F9P as rover. The DLF1 station is located on the rooftop of the Nederlands Metrology institute (NMi) in Delft. The station uses a Trimble NetR9 receiver, capable of tracking most GNSS signals, with a Leica AR25.R3 (LEIAR25.R3) chokering antenna with LEIT radome. The antenna has been calibrated by Geo++. The antenna is installed on the permanent marker with DOMES number 13502M009.

The rover receiver is an engineering sample of recently released low-cost dual-

frequency receivers, that was obtained from the manufacturer for testing purposes. It covers the following frequencies: GPS L1C/A, L2C, GLONASS L1OF, L2OF, Galileo E1, E5b and BeiDou B1I, B2I and QZSS L1C/A, L2C. Notably missing GNSS signals are GPS L2P/Y, GPS L5 and Galileo E6. However, with the new generation GPS satellites, the L2C signal becomes rapidly available on almost all satellites and enables obtaining dual-frequency measurements from an increasing number of available GPS satellites. With up to 184 channels available, the receiver is capable of tracking two frequencies on each of the described satellite constellations and is still able to receive correction service data from augmented GNSS (e.g. [23]).

The antennas of the rover are placed on a geodetic marker at a horizontal distance of approximately 10 meter and 1.5 m height difference from DLF1. Different antenna types have been installed during consecutive periods from 15.02.2019 onwards. The investigated rover antennas cover a range of prices, starting with the lowest cost antennas U-blox ANN-MB-00 and Taoglas AQHA50 between about 50 and 100 euros, the middle price segment antennas Trimble AV28 and Trimble GA530 and antennas with a price of above 1,000 euros, LEIAR25.R3 LEIT and TRM55971.00 NONE (also known as Trimble Zephyr 2 Geodetic). For these antennas, the mount point DOMES 13502M003 (GPS Mark 15) is used (Figure 4.1 b). The antennas with hole-mount design (Trimble AV28) and without screw-hole at the bottom (U-blox ANN-MB-00) are mounted on top of a metallic rectangular extension bracket and also with a circular metallic ground plane with 10 cm diameter. For the other tested antennas, a tribrach with an adjustable circular level is used. The receiver itself is placed in a pelican case in the proximity and data logging is performed with a Raspberry Pi Zero on a local SD card (Figure 4.1 a). Depending on weather conditions and observation time, antennas are switched after at least having recorded three full days of raw data. Data is transferred manually from the SD card for post-processing purposes.

The installation environment (regarding near-field effects and multipath) can be regarded as relatively clean. Both antenna positions (DLF1 and GPS Mark 15) are characterized by an unobstructed view over the full horizon. The time frame of antenna placements is depicted in Table 4.1. All antennas are active and, depending on the type, require different voltage as input. The antennas GA530, LEIAR25.R3 and TRM55971.00 require 12V input voltage which cannot be supplied by the Raspberry Pi. Instead, the antennas are powered by a Septentrio receiver and the antenna signal is split to the U-blox ZED-F9P. The other antennas are working with voltage at or below 5V that is supplied via the USB port of the Raspberry Pi and is considered as stable.

The GA530 lost satellite tracking on L1 on 15.03.2019 17.23 UTC and one day later also L2 data was lost, presumably due to moisture in the antenna connector. Data from 15.03.2019 onwards is therefore discarded from the GA530 observations. The AQHA50 data was not processed due to very low Signal-to-Noise (SNR) ratio, despite free-sky conditions, which we were unable to resolve. After quick and uncomplicated communication with the manufacturer the antenna could be returned and a replacement was provided. It was, however, not examined further in this experiment because of time limitations and practical considerations. A power outage in the Delft region, in the morning of Monday 25.03.2019, ended the data tracking for the LEIAR25.R3 antenna. Except for the AQHA50 antenna, sufficient data have been recorded for the remaining antennas for

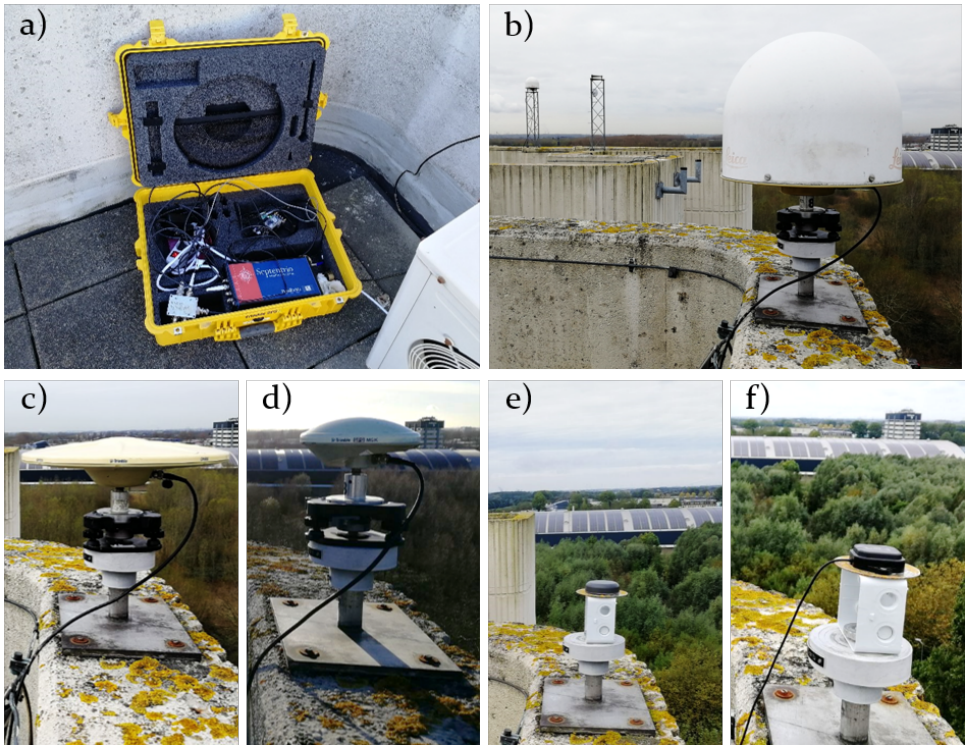

Figure 4.1: Waterproof pelican box rover equipment on the ground next to the marker (a). The pelican box contains the U-blox ZED-F9P, a Raspberry Pi Zero for data logging, power and a Septentrio receiver. The Septentrio receiver is used to provide power, through an antenna splitter, to the antennas: LEIAR25.R3 (b), Zephyr2 (c) and GA530 (d). No data collection or processing is performed with the Septentrio receiver. The verification setup is depicted in (b). It shows the baseline setup with two LEIAR25.R3 LEIT antennas. The antenna in the foreground is at the marker that is used for the investigation. In the background the radome and antenna of the base station DLF1 is visible. Both antennas are oriented North. The subfigures (b-f) illustrate the marker used for the investigation with different installed antennas. The antennas AV28 (e) and ANN-MB-00 (f) are depicted with a circular plane.

Table 4.1: Time frame and antenna descriptions of the antenna placements on GPS Mark 15 for the short-baseline experiments.

Start	End	DOYs	Antenna, description
15.02.2019	20.02.2019	046-051	Trimble AV28 (stacked patch), rectangular bracket
20.02.2019	26.02.2019	051-057	Taoglas AQHA50 (stacked patch), rectangular bracket
26.02.2019	05.03.2019	057-064	U-blox ANN-MB-00 (stacked patch), rectangular bracket
05.03.2019	19.03.2019	064-078	Trimble GA530 (radome)
19.03.2019	26.03.2019	078-085	LEIAR25.R3 LEIT (choke ring)
26.03.2019	02.04.2019	085-092	Trimble TRM55971.00 NONE (resistive plane)
11.10.2019	15.10.2019	284-288	Trimble AV28 (stacked patch), circular plane
15.10.2019	18.10.2019	288-291	U-blox ANN-MB-00 (stacked patch), circular plane

the analysis. Details about the data logging and conversion can be found in appendix A.

The data is analysed in post-processing, with DLF1 as base station, and the antennas under investigation as rover. The rover data is available as 1-second daily RINEX 3 observation files. For the base station data, high-rate (1Hz) RINEX3 data from the IGS station DLF1 were downloaded. High-rate 15-minute RINEX 3 DLF1 observations were merged into daily files. Broadcast navigation data from the satellites were collected from the Crustal Dynamics Data Information System (CDDIS) [24]. For simplicity reasons and driven by the fact that most antenna calibrations are available for GPS, we used GPS-only data for our analysis.

4.2.2. ANTENNA CALIBRATION AND ZTD EVALUATION PROCEDURE

This subsection aims to provide a general overview of the antenna calibration and ZTD evaluation procedure. The experiment basically follows the steps illustrated in Figure 4.2. First, the antenna calibration is performed by retrieving residuals in a short baseline experiment, for which errors caused by the troposphere and ionosphere delays can be safely neglected. The original L1+L2 RINEX data of base and rover were processed in RTKLIB, in static mode, to obtain the carrier phase residuals for each frequency, as well as azimuth (az) and elevation (el) angles of the corresponding satellites. The residuals, that can be considered as relative PCVs, together with IGS ANTEX type mean PCVs of the base station antenna (LEIAR25.R3 LEIT), were processed to create absolute PCVs which are saved in new ANTEX entries for each rover antenna. Details on the antenna types used in the experiment are provided in Table 4.1.

Subsequently, the L1+L2 RINEX data from the rover antennas, with the new ANTEX entries, were processed in goGPS (PPP-mode) to obtain absolute ZTD estimations. The obtained set of ZTD estimations for the low-cost receiver and different antennas was

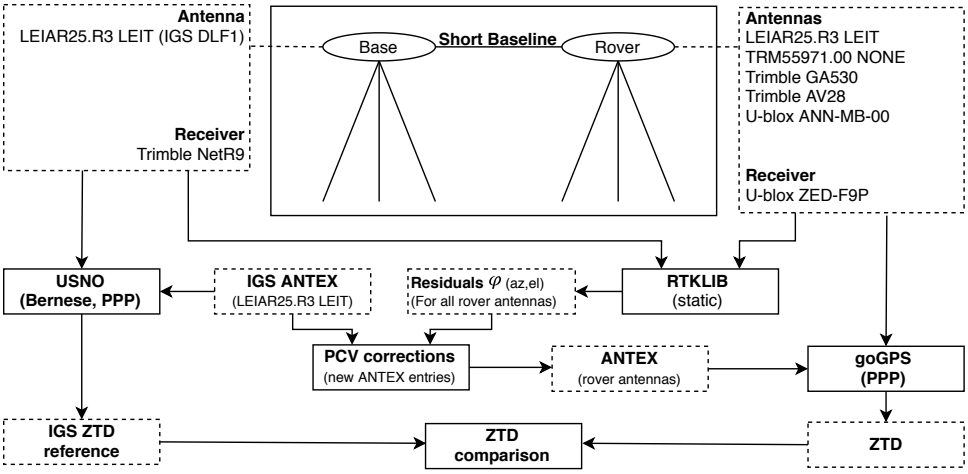

Figure 4.2: Steps in the ZTD evaluation procedure. The top central box illustrates the short baseline with base station (DLF1) on the left and rover on the right. The base station DLF1 uses a Trimble NetR9 receiver and LEIAR25.R3 LEIT antenna, which did not change during the time frame of our experiment.The rover is illustrated on the right, with an U-blox ZED-F9P receiver and five antenna types applied consecutively.

compared against the IGS final ZTD estimations by the US Naval Observatory (USNO) based on Bernese 5.2 in PPP mode from the IGS station DLF1. Further details on the antenna calibration and ZTD estimation procedures can be found in the following subsections.

4.2.3. ANTENNA CALIBRATION AND RETRIEVAL OF NEW ANTEX ENTRIES

This subsection details the antenna calibration process. It is a fundamental step in our experiment and consists of an elevation-only and an azimuth and elevation dependent correction.

Near-field, multipath and antenna PCVs, summed up as multipath, affect all estimated parameters and residuals in the processing. Objects that are close to the antenna (near-field) affect the antenna patterns especially in the antenna PCO and azimuth- and elevation dependent PCVs. This effect cannot be covered in existing antenna calibrations without conducting the calibration procedure at the same location where the observation is taking place.

The main part of the antenna calibration consists of obtaining satellite phase residuals and is performed using RTKLIB. For each frequency, in our case GPS L1 and L2, the residuals are 'stacked' into elevation and azimuth bins. Two types approaches are used: 1) an elevation-only correction by averaging over all azimuth directions and 2) an azimuth and elevation dependent correction.

The GNSS processing engine RTKLIB [25] is open source and contains a range of Application Programs (APs) to perform real-time and post-processing precise positioning with GNSS data. It employs an Extended Kalman Filter (EKF) to obtain final differen-

Table 4.2: RTKLIB RNX2RTKP command line options

Option	Command-line parameter
Positioning solution: static	-p 3
Elevation cut-off: 5 degree	-m 5
AR: fix-and-hold	-h
AR validation threshold: 3	-v 3.0
Output: residuals	-y 2
Output: East, North, Up baseline	-a
Satellite systems: GPS-only	-sys G
Time format: YYYY/MM/DD hh:mm:ss	-t
Kalman filter: forward + backward	-c

tial solutions. In our analysis, the baseline processing was performed using the RTKLIB 2.4.3 Command-line User Interface (CLI) RNX2RTKP. Its functions are equivalent to the Graphical User Interface (GUI) program RTKPOST. In its standard configuration the program uses the highest elevation satellite as reference to obtain DDs. The residuals are written to a file for each satellite in view, with a zero value for the reference satellite, actually using a single difference (SD) format to store the DD residuals. For the analysis of the phase center variation we need however SD residuals. To obtain the SD residuals the average of the DD residuals (reference satellite included) must be subtracted from the DD residuals (again reference satellite included). This is the same as using the average DD residuals as reference. In order to use the average DD residuals as a reference, the source code was modified and recompiled. The observed measurement errors now had an expected zero mean of all satellite residuals on each frequency and not only for the highest elevation satellite. In our version the residuals were computed as in previous (legacy) RTKLIB releases. To avoid unintended behavior, the changes were discussed and changed in correspondence with the author of the package on github (see github issue: [26]).

Table 4.2 shows the processing settings used for the baseline analysis. Important processing options are the positioning solution to static (-p 3), elevation cut-off 5 degrees (-m 5), AR fix-and-hold (-h) and output residuals (-y 2). For Ambiguity Resolution (AR), the LAMBDA algorithm [27] is used within RTKLIB. The basic strategy in RTKLIB is to fix the ambiguities to integer after a float solution has been obtained. In our analysis we decided to use the fix-and-hold method. Further details on a conducted sensitivity case study can be found in Appendix B. The static processing option will strictly constrain the receiver movements for the observation period. It is preferred over a kinematic solution for the residual analysis since the rover antenna position does not change and the measurement errors should reflect this in the residuals and not in the estimated position. Driven by uncertainty about the implementation of applying ANTEX PCV corrections in RTKLIB, the antenna calibrations were not applied directly in the processing. Instead, their influence was analyzed separately. Each observation file of each antenna was processed and the generated output consisted of East, North and Up (ENU) components as well as frequency and azimuth and elevation dependent satellite residuals on code and

phase measurements. For the relative antenna calibration, only the phase residuals were utilized.

To reduce noise and avoid outliers in the data, the residuals of each antenna are stacked over generally three selected DOYs (LEIAR25.R3: 79, 81, 83; TRM55971.00: 87, 88, 90; GA530: 65, 66, 70; AV28 with rectangular bracket: 47, 48, 49; AV28 with circular plane: 285, 286, 287; ANN-MB with rectangular bracket: 58, 61, 62) which were selected after a visible inspection. Only the ANN-MB-00 circular plane data is stacked over two days (DOYs 289 and 290) driven by the short observation period and evident outliers in the observed residuals.

In the first approach, the elevation-only phase patterns are visualised based on a first stacking, by taking the mean from all observations within 0.5 degree elevation bins. Afterwards, to correspond to the ANTEX standard, the stacked elevation-only phase residuals were averaged to 5 degree elevation bins using a moving-average filter. The resulting smoothed curve is shifted and start and end point (5 and 85 degrees) are substituted with the fitted data from a 10th order polynomial that was fitted over the 0.5 degree data. The resulting smoothed residual curve is the relative antenna calibration PCV (see also Figure 4.5).

For the second approach, the azimuth and elevation dependent calibration, the number of residuals in each bin is not very large, and there will be many bins that are empty. To obtain meaningful azimuthal PCVs one should typically use longer observation time spans and rotate the antenna during the experiment in order to sample all azimuth directions. Since our experiment did not include rotating the antenna, and the observation period is only a few days, we don't expect very reliable azimuth corrections. To obtain azimuth dependent antenna patterns, the observed residuals were averaged over 5 degree elevation and azimuth bins and stacked over selected days. Since these measurements are generally noisy, the binned residuals are looped through the elevation bins and smoothed by fitting a 10th order polynomial to the data. To avoid evident outliers by fitting a polynomial to the data, gaps and missing data (especially in the North direction, see also Figure 4.6) are filled by the nearest value from the current elevation bin. The 5 degree binned data used for the PCV calibration are taken from the resulting fitted polynomial curves.

For both approaches, to obtain absolute PCVs for each tested antenna, the estimated relative PCVs (averaged residuals) must be added to the absolute PCV of the base station antenna. For the absolute PCV of the base station antenna (LEIAR25.R3 LEIT) we used the IGS type mean azimuth and elevation dependent PCVs. Equation 4.1 shows how the rover antenna PCV is created:

$$\varphi_i^r(az,el) = \varphi_i^b(az,el) + \widetilde{\varphi}_i^{br}(az,el) \tag{4.1}$$

The superscripts b and r denote the base and rover, the subscript i the frequency, az and el the azimuth and elevation angles. By adding the estimated relative PCV of the rover ($\widetilde{\varphi}^{br}$) to the absolute base antenna PCV (φ^b), we obtained the absolute PCVs (φ^r) for the tested antenna. To use the newly generated PCVs in PPP tests, a new entry for each antenna was added to, or replaced in, the ANTEX file. Though individual calibrations are available for our base station antenna, we use the IGS I14.ATX ANTEX file that contains type mean calibrations for the base antenna PCV. A recent study by Araszkiewicz et al.

Table 4.3: goGPS settings for PPP ZTD estimation

Type	Parameter
Observations	GPS-only
Elevation cutoff	10°
Ocean loading	FES2004
Observation weighting	same weight for all observations
Code observation error threshold	30 m
Phase observation error threshold	0.05 m
Code least-squares estimation error st. dev. threshold	40 m
Clock & orbits	IGS Final
Troposphere modeling	Saastamoinen (with GPT model)
Troposphere mapping function	GMF
Sampling interval	30-second
Antenna calibration	IGS, own, none
Kalman filter reset	no (seamless)

2019 [28] investigated the height variation on the LEIAR25.R3 antenna with type mean and individual calibrations. They conclude that both methods show similar results.

For each approach (elevation-only and azimuth-elevation), a new ANTEX file is created with one new entry for each antenna that can be used for ZTD estimation using PPP. In this way, the antenna names given in the RINEX files do not have to be modified by instead supplying a respectively differently generated ANTEX file.

4.2.4. EVALUATION OF ZTD ESTIMATES FROM DUAL-FREQUENCY PPP

This subsection describes the PPP processing configuration and ZTD evaluation procedure with dual-frequency GNSS measurements.

To estimate absolute ZTD values and to evaluate the newly obtained antenna PCVs, the open source tool goGPS [29] was used. Its ZTD estimations are comparable to existing reference datasets [6], [7]. The ZTD results are computed for all available DOYs and compared to IGS final ZTD estimations from the IGS station DLF1 [24] in approximately 10 meter distance. The closest available data point from the high rate ZTD estimations was used to match the IGS reference (5-minutes) interval.

We used goGPS PPP with the same configuration for all runs but with different ANTEX file configurations for the different antennas. The goGPS configuration used for our comparisons can be found in Table 4.3. The concept of the ZTD evaluation is summarized in Figure 4.3.

For all goGPS ZTD estimations, data from GPS-only satellites were used. An elevation cutoff angle of 10 degrees and ocean loading effects obtained from the FES2004 model [30] were applied. The IGS antenna calibration, final orbits, 30-second satellite clocks and earth rotation products were used [31].

The ZTD analysis consisted of up to five different cases. Two of our tested rover antennas, the LEIAR25.R3 LEIT and TRM55971.00 NONE, had already calibration entries in the IGS ANTEX file. This provided another set of PCVs for testing with PPP and serves

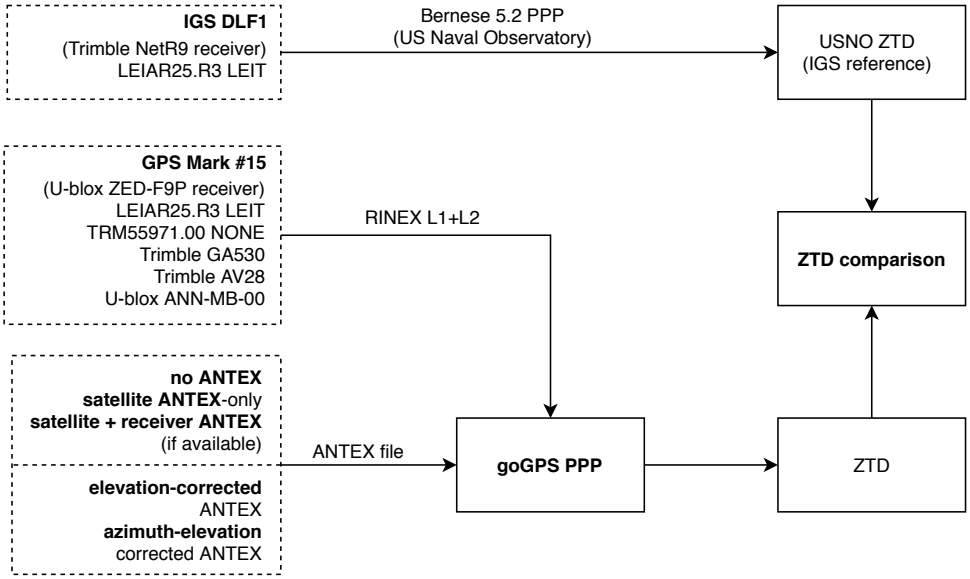

Figure 4.3: PPP ZTD evaluation concept. Original dual-frequency RINEX files are utilized as file input. Several runs with different antennas and ANTEX configurations are tested. The absolute ZTD estimations are evaluated against IGS final ZTD estimations from DLF1.

as a verification of our estimations. The first case consists of the verification antennas (LEIAR25.R3 LEIT and TRM55971.00 NONE antennas). For this, a goGPS PPP run is performed using the original IGS I14.ATX ANTEX file. To investigate the impact of not using an ANTEX file at all, another run without the ANTEX file was performed in a second run. The third case applies only satellite PCO/PCV corrections by removing the receiver antenna-specific entries. The last two cases evaluate the elevation-only and azimuth-elevation corrected ANTEX entries obtained from the calibration step. One has to note that the full observation period (up to ten days observed data) is used as RINEX input for the ZTD estimation, while only two or three days are utilized to compute the PCVs.

If one runs PPP software, e.g. goGPS, over which one has full control, one can use the newly generated ANTEX entries directly in the software. However, when PPP is performed in a server environment, one does not have the possibility to modify the ANTEX files. In these cases it is more convenient to correct the original RINEX phase data for the antenna patterns. To achieve this, we corrected the original RINEX phase data for the PCV estimations retrieved from the calibration step by the following formula:

$$\tilde{L}_i = L_i - \frac{\varphi_i^r(el, az)}{\lambda_i} \tag{4.2}$$

Where $\tilde{L}_i$ is the corrected phase data on frequency i and L_i the original RINEX phase observation. $\varphi_i^r(el, az)$ is the azimuth and elevation dependent antenna phase pattern on frequency i. λ_i denotes the wavelength on each frequency.
A comparison between ANTEX-corrected and RINEX-corrected PPP ZTD comparisons

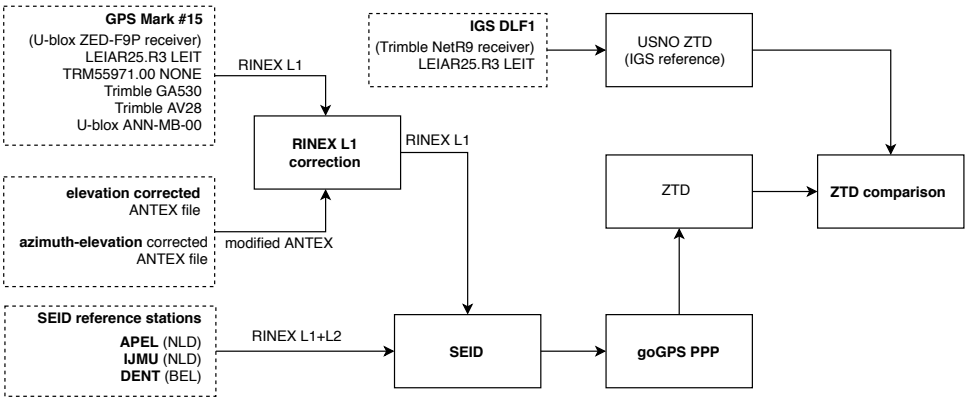

Figure 4.4: SEID PPP methods. The original (dual-frequency) RINEX data is trimmed to L1-only observations and the RINEX correction after eq. 4.2 is utilized. SEID is applied with the stations APEL, IJMU and DENT. The subsequent PPP process is conducted once with the original I14.ATX file and once without the LEIAR25 and TRM55971.00 entries, hence providing satellite PCO/PCV corrections only. The resulting absolute ZTD estimations are evaluated against final IGS ZTD estimations from DLF1.

resulted in no or negligible differences.

4.2.5. EVALUATION OF ZTD ESTIMATES FROM SINGLE-FREQUENCY PPP

This subsection illustrates the single-frequency ZTD evaluation using the Satellite-specific Epoch-differenced Ionospheric Delay model (SEID) from a surrounding dual-frequency network. PPP uses the ionosphere-free linear combination to eliminate the first order effect of the ionospheric delay error. The drawback of this method is that the errors and multipath on L1 is increased by a factor 2.546, and on L2 by a factor 1.546. The effect is that, when the errors are not correlated, the noise of the ionosphere free linear combination is increased by a factor 3. Also for antennas that are sensitive to multipath, or are placed in a multipath-prone environment, this effect may cause the performance to decrease significantly. In these cases the performance of using L1-only measurements may outperform the dual-frequency ionosphere-free linear combination results (see also [32]).

Instead, the SEID algorithm [33], combined with L1 data, generates a synthesized L2 measurement by utilizing data from a network of existing dual-frequency receivers. The synthesized signal contains in principle the same information as L1 but is adjusted to the ionospheric delay on that frequency based on the dual-frequency measurements from the surrounding network. This effectively reduces the noise effect. As part of the evaluation, we apply the SEID model on L1-data using a network of three receivers. By removing the second frequency observations from the RINEX data and correcting the L1 data for elevation and azimuth-elevation patterns, we also investigate the performance of the SEID algorithm on L1-corrected data. Though stations in the close proximity to DLF1 are available, the outside station network distances are chosen between 55 and 130 km to simulate a more realistic scenario to densify existing networks. The SEID evaluation process is depicted in Figure 4.4.

Table 4.4: Mean and RMSE of code and phase residuals from the static solutions of the short baseline experiments. The phase mean is zero for all antennas since the mean of the single-differenced residuals are used as reference for the DD analysis in the modified RTKLIB application.

Antenna	Code RMSE [mm]		Code mean error [mm]		Phase RMSE [mm]	
	L1	L2	L1	L2	L1	L2
LEIAR25.R3 LEIT	508.36	522.46	-0.02	0.00	3.61	4.14
TRM55971.00 NONE	513.57	551.96	0.01	0.14	4.22	5.25
Trimble GA530	540.35	541.41	0.00	-0.02	3.99	5.42
Trimble AV28 (rectangular bracket)	644.51	578.63	0.08	0.11	7.70	8.93
Trimble AV28 (circular plane)	473.30	494.89	0.00	0.00	3.94	5.70
U-blox ANN-MB-00 (rectangular bracket)	632.60	599.06	-0.02	0.00	7.00	9.13
U-blox ANN-MB-00 (circular plane)	515.49	492.47	0.00	0.07	4.28	6.32

The following section describes the results of the experiment by analyzing the satellite phase residuals and ZTD estimations.

4.3. RESULTS

4.3.1. RESIDUALS ANALYSIS AND PCV ESTIMATION TO OBTAIN CORRECTED ANTEX ENTRIES

FIRST, we analyzed the residuals as a crucial step to correct for existing phase patterns caused by the receiving antenna. The residuals are derived from the static RTKLIB solution. The RTKLIB output contains the residuals for each satellite, epoch and frequency on code and phase. Table 4.4 shows the mean residuals and their respective RMSE.

The LEIAR25.R3 LEIT antenna demonstrated the lowest phase RMSE on both frequencies. It is also evident that the L2 phase residuals are generally higher than the L1 residuals for all antennas. The Trimble AV28 and U-blox ANN-MB-00 show generally higher phase RMSE values on both frequencies compared to the other antennas. The phase RMSE is considerably smaller when using a circular metallic ground plane. The antennas in Table 4.4 are ordered by approximated acquisition costs. A quality difference with generally lower phase residuals for the upper price category antennas compared to the less expensive ones is evident. As known from GNSS basics, the code residuals have higher deviations than the phase measurements. The mean code error is not zero because they are less precise and the mean single-difference phase residuals are utilized as reference in computing the double-differences. Though interesting, the code residuals are less important for the analysis because precise applications employ phase measurements. L1 and L2 mean phase residuals averaged over the elevation angle are shown in Figure 4.5.

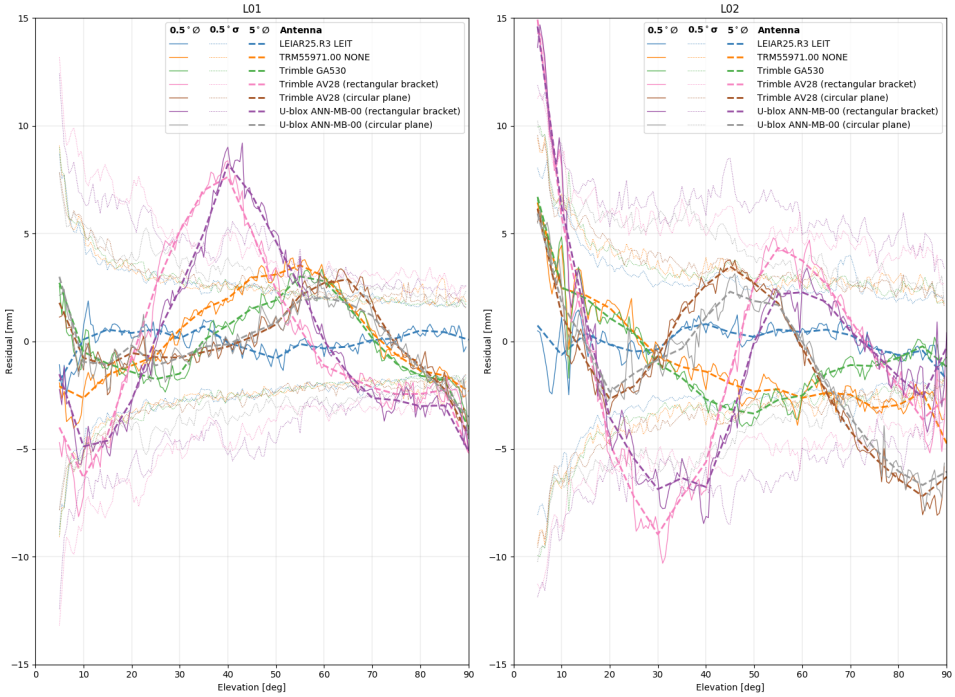

Figure 4.5: Elevation based antenna pattern on the phase residuals. L1 residuals are depicted left and L2 on the right. The continuous lines ($0.5°\emptyset$) show the mean residual over 0.5 degree elevation bins, the dotted lines ($0.5°\sigma$) in the background its respective standard deviation and the dashed line ($5°\emptyset$) the smoothed 5 degree bins corresponding to the ANTEX format.

Figure 4.5 shows the averaged elevation-based pattern for L1 and L2 observations with all tested antennas using a bin size of 0.5 degrees (continuous line), its standard deviations (thin dotted line in the background) and the residuals smoothed over 5 degree bins to correspond to the ANTEX format (thick dashed line). Generally apparent are higher variations at lower elevation angles for all antennas and a higher standard deviation of L2 compared to L1. A clear signal is evident for the Trimble AV28 and U-blox ANN-MB-00 antennas using the rectangular metal bracket as base. This effect can be seen on L1 with satellites between 30 and 50 degrees and on L2 at about 25 and 40 degrees. Since these results evoked further investigation, the experiment was repeated with a circular ground plane. The identified pattern could be reduced when using a circular ground plane. However, on L2 the observed variations above 60 degrees are noticeable greater compared to the other antennas. Evident is that both antennas, although being produced by a different manufacturer and having an inherently different design, demonstrate a comparable elevation-based pattern. The reference antenna LEIAR25.R3 LEIT demonstrated no clear elevation-based phase bias at any elevation angle since both, base and rover antenna are of the same model and the resulting residual error in differential analysis mostly cancels out. The antennas GA530 and TRM55971.00 also demonstrate a slightly visible mean phase pattern.

Typically, azimuth dependent residuals are stacked over several weeks or months of data or over several days by rotating the antenna by some degree. This was not performed in this study. Instead, with the limited observation days available we stacked the azimuth and elevation dependent residuals over the selected observation days. Since the antenna phase residuals of AV28 and ANN-MB-00 with different mountings evokes additional attention, figure 4.6 compares the elevation and azimuth dependent L1 and L2 phase residuals for the reference antenna LEIAR25.R3 LEIT and the antennas Trimble AV28, U-blox ANN-MB-00 with rectangular bracket and circular plane.

The figure demonstrates the performance of a reference antenna (LEIAR25.R3 LEIT) compared to the two low-cost antennas Trimble AV28 and U-blox ANN-MB-00 with a rectangular bracket and a circular plane as base. Note that the zenith angle is used instead of elevation angle to correspond with the ANTEX format and more intuitive interpretation of the polar plots. Generally noteworthy are the fewer satellite tracks on L2 which is caused by not all GPS satellites yet transmitting the L2C signal. As previously illustrated in the elevation based residuals, the LEIAR25.R3 antenna (4.6 a) depicts generally low residuals over the full horizon with only a few higher values close to the ground. The patterns from the antennas AV28 and ANN-MB-00 are characterized by negligible differences between them. Noticeable differences are slightly lower residuals at low elevation in South-West (225°) direction on L1 for the AV28 (Figure 4.6 (b) left) compared to the ANN-MB-00 (Figure 4.6 (d) left) antenna using a rectangular bracket. Evident are also the strong negative residuals on L1 at low elevation in North (0°) direction and the stronger positive residuals on L2 in the same direction. The described L1 pattern at about 45 degree elevation (AV28 rectangular and ANN-MB-00 rectangular in Figure 4.5) is also visible with the strongest signal in East and West direction. The errors using a circular plane are generally smoother for both antennas. Regions with increased residuals are, however, still evident. For further processing, the elevation and azimuth dependent residuals were averaged in 5 degree bins to comply with the ANTEX standard. To overcome possible outliers in the data and since only limited observation days were used, we also applied a polynomial fit over the azimuth dependent signal. Based on the base antenna's (LEIAR25.R3 LEIT) ANTEX PCV entries, the elevation and azimuth-elevation dependent phase residuals were used to generate absolute PCVs to append or replace existing ANTEX entries for the tested antennas.

4.3.2. EVALUATION OF ZTD ESTIMATES FROM LOW-COST DUAL-FREQUENCY RECEIVER AND DIFFERENT QUALITY ANTENNAS

Table 4.5 shows the ZTD bias and RMSE values, computed without supplying an ANTEX file (no ANTEX), applying only satellite PCO and PCV corrections (Only satellite PCO/PCV), using the original IGS ANTEX entries (IGS ANTEX), elevation-only corrected ANTEX entries (El. corrected) and azimuth-elevation dependent corrected ANTEX entries (Az.-el. corrected). For the latter two runs, the existing ANTEX entries from the original IGS ANTEX file were removed and replaced with the generated antenna corrections from our experiment. For all evaluations, the IGS final ZTD estimations from the IGS station DLF1 located at approximately 10 meter distance served as reference.

The PPP runs without supplying an ANTEX file yielded high RMSE of about 15 mm for both antennas and a bias of 7.5 mm for the LEIAR25.R3 LEIT antenna. No significant

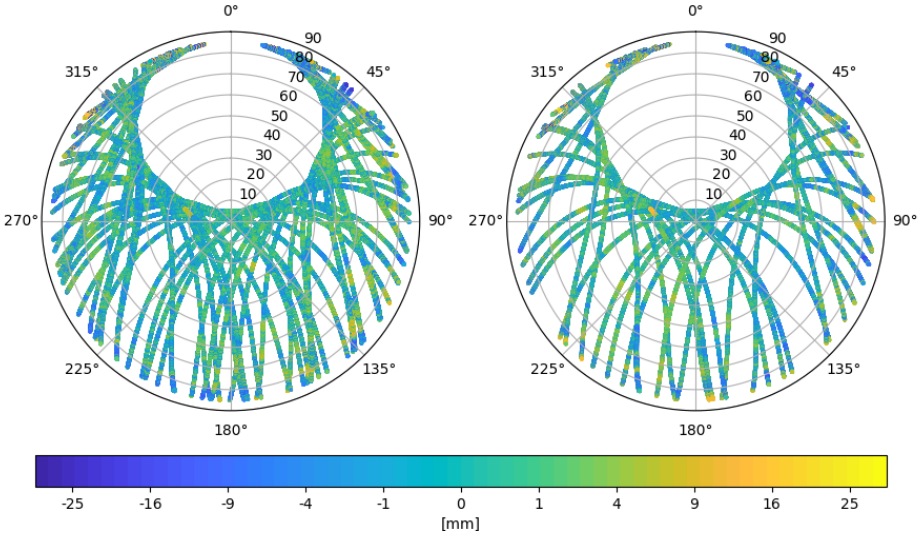

(a) Satellite phase residuals on L1 (top left) and L2 (top right) for the reference antenna LEIAR25.R3 LEIT.

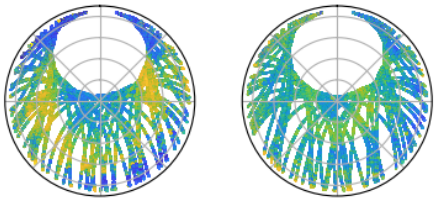

(b) AV28 L1 with a rectangular bracket (left) and a circular plane (right)

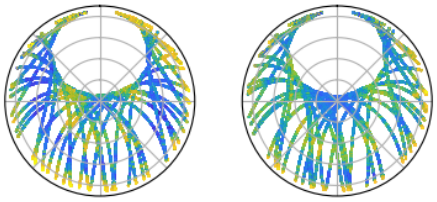

(c) AV28 L2 with a rectangular bracket (left) and a circular plane (right)

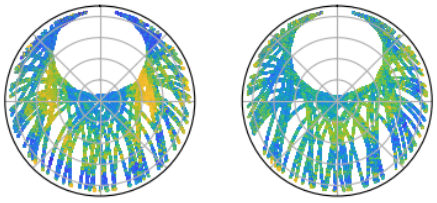

(d) ANN-MB-00 L1 with a rectangular bracket (left) and a circular plane (right)

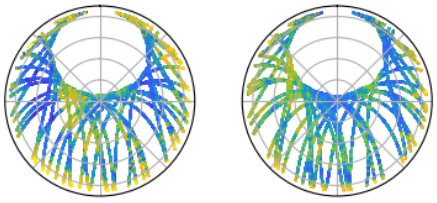

(e) ANN-MB-00 L2 with a rectangular bracket (left) and a circular plane (right)

Figure 4.6: Satellite phase residuals on L1 (left) and L2 (right) for the selected antennas a) LEIAR25.R3 LEIT (top frame), b) AV28 L1, c) AV28 L2, d) ANN-MB-00 L1 and e) ANN-MB-00 L2. The figures b, c, d and e depict on the left the phase residuals using a rectangular metallic bracket as base and on the right with a circular metallic plane of 10 cm diameter.

Table 4.5: ZTD estimation based on antenna PCV corrections with no ANTEX corrections, only satellite PCO/PCV corrections, original IGS type mean ANTEX, elevation corrected ANTEX and azimuth-elevation corrected ANTEX entries on the reference antennas LEIAR25.R3 LEIT and TRM55971.00 NONE. Bias and RMSE refer to the PPP ZTD estimations compared to the IGS ZTD reference.

Antenna	[mm]	No ANTEX	Only satellite PCO/PCV	IGS ANTEX	El. corrected	Az.-el. corrected
LEIAR25.R3 LEIT	Bias	7.50	5.96	1.15	1.08	1.59
	RMSE	15.86	8.02	4.77	4.67	4.64
TRM55971.00 NONE	Bias	-0.89	-1.30	-0.98	-1.17	-2.26
	RMSE	14.20	3.83	3.58	3.59	3.85

Table 4.6: ZTD estimation based on antenna corrections with no ANTEX corrections, only satellite PCO/PCV corrections, elevation corrected ANTEX and azimuth-elevation corrected ANTEX entries on the antennas Trimble GA530, Trimble AV28 and U-blox ANN-MB-00. Bias and RMSE refer to the PPP ZTD estimations compared to the IGS ZTD reference.

Antenna	[mm]	No ANTEX	Only satellite PCO/PCV	El-corrected	Az-el-corrected
Trimble GA530	Bias	3.65	-0.93	-2.21	-3.65
	RMSE	13.79	5.05	4.31	5.06
Trimble AV 28 (rectangular bracket)	Bias	-19.35	-24.04	-3.91	-2.86
	RMSE	23.59	24.82	6.13	5.10
Trimble AV 28 (circular plane)	Bias	12.14	9.54	2.61	2.83
	RMSE	18.02	10.86	5.01	4.79
U-blox ANN-MB-00 (rectangular bracket)	Bias	-14.54	-19.55	-3.34	-3.58
	RMSE	20.19	20.59	6.64	5.44
U-blox ANN-MB-00 (circular plane)	Bias	6.47	5.26	-0.47	-0.52
	RMSE	15.32	7.23	4.02	3.77

bias is evident for the TRM55971.00 NONE antenna. Applying only the satellite PCO and PCV corrections, the bias of the LEIAR25.R3 antenna slightly decreased to about 6 mm and the RMSE to about 8 mm. The bias of the TRM55971.00 antenna remained at about the same level while the RMSE decreased drastically to about 4 mm which already agrees well with the expected standard deviation of about 4 mm from the official IGS ZTD final product ([34], [3]). Both reference antennas performed well using the original IGS ANTEX file resulting in no significant biases. The RMSE is in an expected range of about 4 mm. Replacing the existing ANTEX entries with the generated ANTEX entries resulted in a similar performance to the IGS reference results with RMSE values between 3 and 5 mm. Remarkably, compared to the LEIAR25.R3 antenna, the bias of the TRM55971.00 antenna increased up to about -2.3 mm in the azimuth- elevation corrected results.

The same evaluation is done for the antennas without official ANTEX entries, yet without the IGS receiver antenna corrections that are unavailable for this case. Table 4.6 shows the results for the ANTEX corrected PPP-based ZTD estimations with the antennas GA530, AV28 and ANN-MB-00.

By supplying no ANTEX file or only correcting for the satellite antenna PCO and PCV, the results in Table 4.6 depict a generally better ZTD quality for the Trimble GA530 antenna compared to the Trimble AV28 and U-blox ANN-MB-00 antennas. A considerable difference is evident when using a circular ground plane and a rectangular bracket for the latter two. While the bias and RMSE of the data with rectangular brackets remained at a constant high level (>20 mm), employing a circular plane reduced the errors down to about 7 and 10 mm RMSE. Remarkably, applying the elevation-only or azimuth-elevation dependent ANTEX entries for these antennas resulted in a significant improvement for both antennas and mounting types. The offsets are lowered to between -0.47 and -3.91 mm and the ZTD RMSE are between 3.77 and 6.64 mm. Whilst the RMSE of the Trimble GA530 remained at the same level of about 5 mm, the bias increased slightly compared to the satellite-only PCO and PCV corrections.

4.3.3. ZTD EVALUATION USING SINGLE-FREQUENCY PPP WITH SEID MODELLING

Table 4.7 shows ZTD results using L1 data combined with SEID modelling of L2. The Table shows results for using the original RINEX L1 data, elevation-corrected L1 data and azimuth-elevation corrected L1 data as input. The IGS ANTEX file is used to provide the satellite PCO/PCVs. In case of the original RINEX L1 data, the receiver PCO/PCV is used as well in case there is an entry in the IGS ANTEX file. In case of the elevation and/or azimuth corrected data the RINEX L1 data is modified for the L1 PCV (no receiver entries from ANTEX are used).

Applying SEID and using the original RINEX L1 data and IGS ANTEX file, the overall performance of the geodetic quality antennas (LEIAR25.R3 LEIT and TRM55971.00 NONE) remained at a high level. It is also evident that noise and bias were significantly decreased for the antennas Trimble AV28 and U-blox ANN-MB-00 for both mounting types compared to the satellite-only PCO and PCV corrected results from Table 4.6. The bias was almost zero for the U-blox ANN-MB-00 (circular plane) and -6 mm for the rectangular bracket dataset. The AV28 data were slightly more biased with values of about 3 mm for the circular plane data and -5 mm using the rectangular bracket. The RMSE values were between about 4 mm and 7.5 mm. Notably, the ANN-MB-00 (circular plane) dataset is already comparable to the reference results from Table 4.6. Applying elevation and azimuth-elevation dependent corrections to the RINEX L1 observations further improved the results with biases between almost zero and 4 mm and RMSE values of about 4 to 6 mm ZTD. The performance of the higher grade antennas (LEIAR25.R3 LEIT, TRM55971.00 NONE and Trimble GA530) remained at a stable level which is similar to the results from Table 4.6.

The results from all conducted evaluations are summarized in the boxplots are shown in Figure 4.7.

The boxplots in Figure 4.7 show the differences between the IGS ZTD reference data and the obtained goGPS PPP ZTD estimations. The boxplots on the left depict the results using the original L1+L2 RINEX data with the original IGS ANTEX, without supplying ANTEX corrections and using only satellite PCO and PCV. One should note that these graphs in the left box illustrate the ZTD results with the original recorded dual-frequency data and different IGS ANTEX constellations. It is evident that supplying the

Table 4.7: ZTD PPP results using original L1 data, elevation-corrected L1 data and azimuth-elevation corrected L1 data together with the original IGS ANTEX type mean entries using SEID. For the reference target antennas only satellite PCO/PCV ANTEX corrections were utilized. For the SEID processing, the DPGA stations APEL (Apeldoorn, Netherlands) and IJMU (IJmuiden, Netherlands) as well as the EUREF station DEUT (Dentergem, Belgium) were used. The stations are located approximately 110, 55 and 130 km from the experimental setup.

Antenna	[mm]	Original L1 and IGS ANTEX	El-corrected L1 and IGS ANTEX	Az-el-corrected L1 and IGS ANTEX
LEIAR25.R3 LEIT	Bias	2.20	2.22	2.67
	RMSE	5.14	5.10	5.31
TRM55971.00 NONE	Bias	1.72	1.69	1.69
	RMSE	4.68	4.66	4.66
Trimble GA530	Bias	1.41	1.55	0.94
	RMSE	4.08	4.13	3.91
Trimble AV 28 (rectangular bracket)	Bias	-5.08	2.26	0.75
	RMSE	7.58	5.96	5.42
Trimble AV 28 (circular plane)	Bias	3.38	3.85	2.89
	RMSE	5.27	5.56	4.90
U-blox ANN-MB-00 (rectangular bracket)	Bias	-6.02	-0.36	-1.84
	RMSE	7.34	4.16	4.44
U-blox ANN-MB-00 (circular plane)	Bias	-0.40	0.22	-0.78
	RMSE	4.23	4.19	4.28

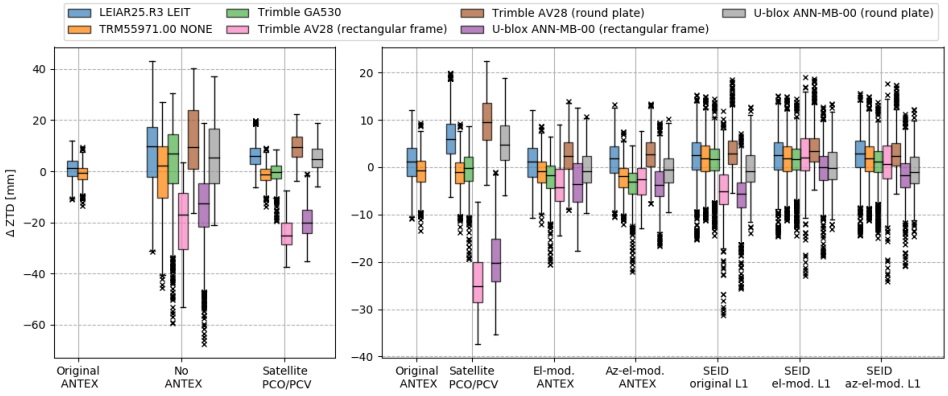

Figure 4.7: Boxplots of goGPS PPP ZTD estimations against IGS reference data from DLF1. The figure on the left depicts the combinations with the original dual-frequency RINEX data using the original IGS ANTEX file, supplying no ANTEX file at all, or only satellite PCO/PCV corrections. The boxplots on the right illustrate the references (original ANTEX, only satellite PCO/PCV), the results with original RINEX L1+L2 and modified ANTEX entries (elevation modified ANTEX, azimuth-elevation modified ANTEX) and SEID results with original, elevation corrected and azimuth-elevation corrected L1 data.

original IGS ANTEX corrections resulted in the smallest errors, but these are not available for the low cost antennas. It also shows that applying no ANTEX corrections to the data yield high standard deviations and offsets in the ZTD estimations. Supplying only satellite PCO/PCV corrections provide reasonable results for the antennas TRM55971.00 NONE and GA530. The antennas LEIAR25.R3 LEIT, AV28 (circular) and ANN-MB-00 (circular) are at a comparable level. Although the standard deviation decreased for the data from the ANN-MB-00 and AV28 antennas, a significant bias was still present for the rectangular ground plate datasets.

The boxplots on the right in Figure 4.7 depict the reference data (original ANTEX and satellite PCO/PCV) and summarize the results for the corrected datasets (the first four groups) and applied SEID experiments (the rightmost three groups). One can note that the corrected data illustrate values in the range between -30 and 20 mm compared to -70 and 45 mm when not using the IGS ANTEX file. The presented results demonstrate a similar performance of all antennas with their most significant differences being the biases. Notably, the biases of the rectangular and circular mounting types are of opposite sign using only satellite PCO/PCV corrections. After correction, the biases are significantly reduced for the LEIAR25.R3 LEIT antenna as well as for the low-cost antennas AV28 and ANN-MB-00 using both, rectangular bracket and circular plane. It also shows that results for the single frequency SEID experiments are comparable to the dual frequency results.

4.4. DISCUSSION

4.4.1. RESIDUAL ANALYSIS

THE presented residual analysis provides elevation- and azimuth-elevation phase patterns on both frequencies for each rover antenna. The analysis proves that antenna dependent residual phase patterns are present, and certain anomalies, e.g. multipath signals presumably caused by the rectangular plate (AV28 and ANN-MB-00), can be exposed. The phase patterns can be modelled to provide corrections and/or a relative antenna calibration for our further investigations. The relative calibrations can be turned into absolute antenna calibrations in the international ANTEX format by averaging over 5 degree elevation and azimuth bins, and adding the relative calibration to the absolute calibration of the reference antenna. An important point of discussion is whether the full azimuth-elevation pattern should be used, or the elevation only pattern. The elevation only pattern is more robust and less sensitive to possible outliers than the azimuth-elevation pattern, it is also computationally less expensive to compute. Three days of data is enough to compute the elevation only pattern. To compute the azimuth-elevation pattern we advise to use more days, and/or rotate the antenna, to fill the gaps in the azimuth patterns. Additional satellite tracks over the horizon can also be obtained by utilizing multiple satellite constellations sharing the same center frequency (e.g. Galileo E1 and GPS L1). However, it introduces additional unknowns (i.e. estimation of an additional clock term) and, in the latitude of the executed experiment, still leaves the gap in the North. Consequently, a carefully conducted rotation of the antenna and accounting for it during the processing can be used to fill gaps in the azimuth pattern and at the same time average potential multipath effects. The result we obtained for the elevation only patterns were comparable to our limited azimuth-elevation patters, thus,

for three days calibration time, we recommend to use the elevation only patterns. The procedure for azimuth-elevation patterns needs some further investigation.

4.4.2. ABSOLUTE ZTD ESTIMATIONS

In order to evaluate the performance of our antenna calibrations on the absolute ZTD estimation several PPP computations were performed. The rover antennas were divided in two groups. The first group is formed by the LEIAR25.R3 LEIT and TRM55971.00 NONE from which we know the antenna patterns from existing type mean IGS ANTEX entries, and which provide an excellent reference for our own calibrations, as well as scenarios in which no or satellite-only antenna calibrations would be available. The results are summarized in Table 4.5 and Figure 4.7. Using no ANTEX file at all, the ZTD RMSE compared to the IGS reference is about 15 mm for both antennas in contrast to about 4 mm with applying the IGS PCO and PCV corrections. Supplying only satellite antenna corrections decreases the ZTD RMSE to 8 mm (LEIAR25.R3 LEIT) and to about 4 mm (TRM55971.00 NONE). It also shows that the LEIAR25.R3 LEIT antenna, caused by the antenna design and radome, has a phase pattern that deviates significantly from a sphere, resulting in a bias of about 6 mm when applying only satellite antenna corrections (and ignoring the receiver corrections). This makes it particularly important to correct for this error with this antenna type. The TRM55971.00 NONE antenna pattern suggests to have only little impact on the ZTD estimation with almost identical results comparing the original IGS ANTEX data results. It suggests that the PCV of this antenna has a spherical pattern. Applying the antenna PCV corrections from the conducted short baseline analysis demonstrated comparable results for the elevation-based ANTEX correction and slightly less precise results for the azimuth-elevation corrections. Especially the bias increased which suggests that more outliers are present in the azimuth analysis which is presumably caused by the lack of observing days to perform an azimuthal correction with the utilized calibration method. Except for the minor bias, the ZTD RMSE with self-calibrated antenna pattern entries are comparable to the results using the IGS ANTEX calibrations, and comparable to the IGS reference ZTD estimations.

The second group of antennas consisted of the GA530, AV28 and ANN-MB-00. Since no official antenna calibrations are available for these antennas, the performance could not be evaluated directly against official calibrations. However, the IGS supplies official ZTD estimations from DLF1 to which the results can be compared. Since the PPP processing scheme is not changed except for the supplied ANTEX files, the results demonstrate the antenna phase variation impact on the tropospheric delay. They are shown in Table 4.6 and Figure 4.7. The results of the GA530 antenna are comparable to the performance of the LEIAR25.R3 and TRM55971.00 antennas. Supplying no ANTEX file at all, high ZTD biases in the order of -20 mm and -15 mm for the AV28 and ANN-MB-00 antennas are evident with the rectangular bracket. Using a circular plane reduced them to about 12 mm and 6.5 mm, respectively, while maintaining similar RMSE. When applying satellite PCO and PCV corrections, the boxplots in Figure 4.7 (Satellite PCO/PCV column) demonstrate that the standard deviation decreased notably. The presented offsets and consequently RMSE values limit the application of the data for meteorological purposes. After applying the elevation-only antenna corrections to the data, the bias and RMSE decreased significantly for the antennas AV28 and ANN-MB-00. Remarkably, the applied

corrections did not only increase the performance of the antennas with a circular plane, but also significantly decreased the error from using the rectangular bracket as base. Applying the azimuth-elevation dependent corrections to the data slightly increased the performance of the low-cost antennas. The bias increased slightly for the GA530 antenna and is presumably caused by the short observation time and outliers present in the residuals. The results are encouraging and demonstrate that the applied corrections for low-cost antennas make the data more attractive for tropospheric analysis. Particularly, the performance of the patch antenna ANN-MB-00 with a circular ground plane after correcting the phase pattern yields comparable results (0.47 mm bias and 4.02 mm RMSE) to those from geodetic quality antennas. To confirm these findings, longer observation times are recommended. The utilized IGS I14.ATX ANTEX file consisting of the elevation-only calibrations (without PCO estimations) for the antennas LEIAR25.R3 LEIT, TRM55971.00 NONE, Trimble GA530 and Trimble AV28 and U-blox ANN-MB-00 using a circular plane is attached as supplementary material.

4.4.3. DUAL- VERSUS SINGLE-FREQUENCY

The ionosphere-free linear combination, which is applied to dual-frequency data in PPP to eliminate the ionospheric delay, almost triples the noise in the data. Considering that noise in the data, including the noise in the antenna calibrations, is the major contributor to the bias and RMSE in the ZTD estimation, it can be useful to use L1 data only. Also, although this could change in the future, single frequency receivers are more readily available than cheap dual-frequency receivers. By applying the SEID algorithm to L1-only observations, an artificial second frequency is generated from the L1 data using the interpolated ionospheric delay from a network of dual-frequency reference receivers. We apply this method to investigate if L1-only measurements may be favorable for ZTD estimations. The results are shown in Table 4.7. Using the original L1-only data and IGS ANTEX file, the SEID results indicate a similar performance for the high-quality antennas LEIAR25.R3, TRM55971.00 and GA530 compared to the L1+L2 processing using the original IGS ANTEX file (Tables 4.5 and 4.6). Compared to results obtained using only satellite PCO/PCV corrections, the performance of the AV28 and ANN-MB-00 antennas increased significantly after applying SEID on the original data. The lowest bias (-0.40 mm) and RMSE (4.23 mm) is observed with the ANN-MB-00 using a circular plane as base. The results with rectangular brackets demonstrate a ZTD RMSE of about 7 mm and a bias of -5 to -6 mm. Especially the bias of the datasets with rectangular brackets could be reduced to -0.36 mm (ANN-MB-00) and 2.26 mm (AV28) after applying elevation corrections to the L1 data. Applying the azimuth-elevation dependent corrections to the L1 input data resulted in minor improvements for the AV28 data and slight degradation of the ANN-MB-00 data.

These results suggests that the original L1+L2 data is considerably affected by noise amplified by the ionosphere-free linear combination. Provided that a network of high quality surrounding stations exists, the approach demonstrates the strong advantage of the SEID algorithm to generate L2, which drastically reduces the noise on the target receiver data. There is, however, a trade-off between smoothing the true signal and the underlying noise. Utilizing this method almost eliminates the ZTD bias that was present in the data and the RMSE decreased to a level that is comparable to high-quality mea-

surements which makes it attractive for meteorological applications such as water vapor estimation.

4.5. CONCLUSION

IN this paper we investigated the PPP ZTD performance of a recently introduced low-cost dual-frequency receiver (U-blox ZED F9P) in combination with different antennas, ranging from geodetic to mass-market devices, with and without applying relative antenna calibrations. The conducted experiments demonstrated that the U-blox ZED-F9P dual-frequency receiver is very well capable to produce high-quality results, with the limiting factor being the quality of the receiving antenna. However, our results show that, using a simple-to-apply method to correct for the PCV of cost-efficient receiver antennas, high quality results are achievable even for low-cost antenna. This is demonstrated by a field experiment, resulting in ZTD estimations of similar quality as with high-grade antennas.

The phase residuals with different antenna types were analyzed over a short baseline. The aim was to do a relative antenna calibration. The absolute antenna calibration pattern can then be computed from the absolute antenna calibration of the reference antenna and the relative calibration result from the short baseline experiment. For two of the tested antennas, the AV28 and ANN-MB-00 antennas, when used with a rectangular bracket as mounting point, very prominent elevation-based patterns were found (see Figure 4.5). These cases result in the highest RMSE phase residuals when compared to other antennas. Figure 4.6 indicates azimuth dependent patterns with strongly fluctuating amplitudes. The rectangular bracket presumably caused high residuals for L2 close to the horizon, but also in East and West direction for L1. Smaller residuals were obtained after repeating the experiment with a circular ground plane. These results showed that our approach is working, regardless of the size of the residual patterns. This suggests that our approach is feasible for even more challenging, multipath-prone environments. Additional uncertainty may be introduced by the smoothing technique we used to obtain PCVs in the 5-degree bin size required by the ANTEX standard. A lower binning size may further improve the results. Considering that only three days of data were used for the calibration, and that the antenna was not rotated, many of the azimuth-elevation bins were without data or had only few observations. For this reason the elevation-only based calibration is preferred over the azimuth-elevation based calibration.

The impact of the different antenna PCV corrections on PPP ZTD estimations has been analyzed for the tested antennas. Our results confirm that antenna pattern corrections are essential for PPP ZTD estimations. Applying satellite PCO/PCV corrections significantly decreases the standard deviation in the ZTD error compared to using no ANTEX corrections at all. Without applying receiver antenna corrections, the ANN-MB-00 and Trimble AV28 antennas with a rectangular bracket, resulted in a ZTD bias between -20 and -24 mm and similar standard deviations. With a circular plane the effect could be partially mitigated, but biases in the order of about 9.5 mm and 5.3 mm remained. The results suggest that a phase pattern is present for the low-cost antennas which we address by applying a relative antenna calibration. Applying elevation or azimuth-elevation dependent corrections to the data reduced the ZTD bias significantly and lowered the standard deviation. For example, when using the azimuth-elevation

dependent corrections on the ANN-MD-00 antenna, the bias in the ZTD was reduced to -0.52 mm and an RMSE to only 3.77 mm. Results for other low-cost antenna, and using elevation only patters, were similar. This shows that the ZTD estimations achieve an error level that is comparable to high-grade antennas. Though the biases for ANN-MB-00 (rectangular bracket), AV28 (circular plane) and AV28 (rectangular bracket) could not be completely removed, they were reduced significantly to a level that makes the observations useful for tropospheric analysis.

The ionosphere-free linear combination used by the PPP solutions is very noisy. The noise in the L1 and L2 data, including the errors in the relative calibration, is basically tripled. For this reason we also looked at only using the L1 data in combination with the SEID algorithm to generate L2 data from an existing network of geodetic-grade receivers. In case no PCV correction is done for the receiving antenna, the bias and standard deviation in ZTD for the GA530, AV28 and ANN-MB-00 antennas, were smaller using L1 with SEID generated L2 data, than for the original dual frequency data. This is a clear indication that the ionosphere-free linear combination on the original L1+L2 data is considerably amplifying the noise present in the datasets. Using SEID in combination with the elevation or azimuth-elevation based L1 corrected data removed the biases almost entirely. The results are of comparable quality to ZTD estimations derived from the dual-frequency results.

This experiment uses exclusively GPS observations. As many of the low-cost receivers can track multiple GNSS systems, expanding the antenna calibrations to include multi-GNSS may further increase the application of the presented approach. An other interesting experiment would be to perform an absolute antenna calibration by a specialized company on low-cost antennas and compare their calibrations to our results. Further work is needed to investigate, if the observed pattern is reproduced (or differs) from other antennas of the same model, so that the observed elevation-based phase pattern of an antenna can be applied to other antennas of the same model. This will be subject of future experiments.

REFERENCES

[1] M. Bevis, S. Businger, T. A. Herring, C. Rocken, R. A. Anthes, and R. H. Ware, *GPS meteorology: Remote sensing of atmospheric water vapor using the global positioning system,* Journal of Geophysical Research: Atmospheres **97**, 15787 (1992).

[2] S. Bonafoni, R. Biondi, H. Brenot, and R. Anthes, *Radio occultation and ground-based GNSS products for observing, understanding and predicting extreme events: A review,* Atmospheric Research , 104624 (2019).

[3] G. Guerova, J. Jones, J. Douša, G. Dick, S. d. Haan, E. Pottiaux, O. Bock, R. Pacione, G. Elgered, H. Vedel, and M. Bender, *Review of the state of the art and future prospects of the ground-based GNSS meteorology in Europe,* Atmospheric Measurement Techniques **9**, 5385 (2016).

[4] J. Zumberge, M. Heflin, D. Jefferson, M. Watkins, and F. Webb, *Precise point positioning for the efficient and robust analysis of GPS data from large networks,* Journal of Geophysical Research B: Solid Earth **102**, 5005 (1997).

[5] A. Hauschild, *Combinations of observations,* in *Springer Handbook of Global Navigation Satellite Systems* (Springer International Publishing, 2017) pp. 583–604.

[6] S. Barindelli, E. Realini, G. Venuti, A. Fermi, and A. Gatti, *Detection of water vapor time variations associated with heavy rain in northern Italy by geodetic and low-cost GNSS receivers,* Earth, Planets and Space **70**, 28 (2018).

[7] A. Krietemeyer, M.-c. ten Veldhuis, H. van der Marel, E. Realini, and N. van de Giesen, *Potential of cost-efficient single frequency GNSS receivers for water vapor monitoring,* Remote Sensing **10**, 1493 (2018).

[8] J. Kouba, F. Lahaye, and T., *Precise point positioning,* in *Springer Handbook of Global Navigation Satellite Systems* (Springer International Publishing, 2017) pp. 723–751.

[9] G. L. Mader, *GPS antenna calibration at the National Geodetic Survey,* GPS solutions **3**, 50 (1999).

[10] G. Gendt, *IGS switch to absolute antenna model and ITRF2005,* IGSMAIL-5438, IGS Central Bureau, Pasadena (2006).

[11] B. Görres, J. Campbell, M. Becker, and M. Siemes, *Absolute calibration of GPS antennas: laboratory results and comparison with field and robot techniques,* GPS solutions **10**, 136 (2006).

[12] B. R. Schupler, R. L. Allshouse, and T. A. Clark, *Signal characteristics of GPS user antennas,* Navigation **41**, 276 (1994).

[13] G. Wübbena, M. Schmitz, G. Boettcher, and C. Schumann, *Absolute GNSS antenna calibration with a robot: repeatability of phase variations, calibration of GLONASS and determination of carrier-to-noise pattern,* in *Proceedings of the IGS Workshop* (2006) pp. 8–12.

[14] Geo++, *GNSS technologies,* http://www.geopp.de/ (2019), accessed: 2019-09-23.

[15] IGS, *ANTEX: The Antenna Exchange Format,* `http://www.igs.org/assets/txt/antex14.txt` (2019), accessed: 2019-09-23.

[16] A. Araszkiewicz and C. Völksen, *The impact of the antenna phase center models on the coordinates in the EUREF Permanent Network,* GPS Solutions **21**, 747 (2017).

[17] R. Schmid, G. Mader, and T. Herring, *From relative to absolute antenna phase center corrections,* in *In: Meindl M.(Ed.) Proceedings of the IGS Workshop and Symposium 2004, Bern, Astronomical Institute, University of Bern* (2005) pp. 209–219.

[18] D. Sidorov and F. N. Teferle, *Impact of antenna phase centre calibrations on position time series: preliminary results,* in *IAG 150 Years* (Springer, 2015) pp. 117–123.

[19] M. Rothacher, *Estimation of station heights with gps,* in *Vertical Reference Systems*, edited by H. Drewes, A. H. Dodson, L. P. S. Fortes, L. Sánchez, and P. Sandoval (Springer Berlin Heidelberg, Berlin, Heidelberg, 2002) pp. 81–90.

[20] Y. G. Ejigu, A. Hunegnaw, K. E. Abraha, and F. N. Teferle, *Impact of GPS antenna phase center models on zenith wet delay and tropospheric gradients,* GPS Solutions **23**, 5 (2018).

[21] Y. E. Bar-Sever, P. M. Kroger, and J. A. Borjesson, *Estimating horizontal gradients of tropospheric path delay with a single GPS receiver,* Journal of Geophysical Research: Solid Earth **103**, 5019 (1998).

[22] R. Pacione, A. Araszkiewicz, E. Brockmann, and J. Dousa, *EPN-Repro2: A reference GNSS tropospheric data set over Europe,* Atmospheric Measurement Techniques **10**, 1689 (2017).

[23] R. Loh, V. Wullschleger, B. Elrod, M. Lage, and F. Haas, *The US Wide-Area Augmentation System (WAAS),* Navigation **42**, 435 (1995).

[24] C. E. Noll, *The Crustal Dynamics Data Information System: A resource to support scientific analysis using space geodesy,* Advances in Space Research **45**, 1421 (2010).

[25] T. Takasu, *RTKLIB: An Open Source Program Package for GNSS Positioning,* https://github.com/tomojitakasu/RTKLIB (2019), accessed: 2019-06-03.

[26] T. Takasu, *RTKLIB github issue tracker,* `https://github.com/tomojitakasu/RTKLIB/issues/457#issuecom\ment-473523905` (2019), accessed: 2019-06-03.

[27] P. J. Teunissen, P. De Jonge, and C. Tiberius, *Performance of the LAMBDA method for fast GPS ambiguity resolution,* Navigation **44**, 373 (1997).

[28] A. Araszkiewicz, D. Kiliszek, and A. Podkowa, *Height Variation Depending on the Source of Antenna Phase Centre Corrections: LEIAR25. R3 Case Study,* Sensors **19**, 4010 (2019).

[29] A. M. Herrera, H. F. Suhandri, E. Realini, M. Reguzzoni, and M. C. de Lacy, *goGPS: open-source MATLAB software,* GPS solutions **20**, 595 (2016).

[30] F. Lyard, F. Lefevre, T. Letellier, and O. Francis, *Modelling the global ocean tides: modern insights from FES2004,* Ocean dynamics **56**, 394 (2006).

[31] J. Dow, R. Neilan, and C. Rizos, *The International GNSS Service in a changing landscape of Global Navigation Satellite Systems,* Journal of Geodesy **83**, 191 (2009).

[32] H. Van Der Marel and P. De Bakker, *Single- versus Dual-Frequency Precise Point Positioning,* Inside GNSS **1**, 30 (2012).

[33] Z. Deng, M. Bender, G. Dick, M. Ge, J. Wickert, M. Ramatschi, and X. Zou, *Retrieving tropospheric delays from GPS networks densified with single frequency receivers,* Geophysical Research Letters **36** (2009), 10.1029/2009GL040018.

[34] IGS, *IGS Products,* http://www.igs.org/products (2019), accessed: 2019-09-23.

5

A Field Calibration Solution to Achieve High-Grade Level Performance for Low-Cost Dual-Frequency Receiver and Antennas

The use of calibrated GNSS receiver antennas is crucial to achieving high precision results. These calibrations are generally not available for low-cost antennas. Here we present a simple-to-apply antenna calibration method especially targeted for the use-case of low-cost antennas. It is made available as an online web service (gnss-antcal.citg.tudelft.nl). Users can calibrate rover antennas directly in the field over a short baseline, provided that a base antenna with a known antenna calibration is used. Performance of the calibration method is demonstrated for a range of antennas of different quality and price in combination with a low-cost dual-frequency receiver. Carrier phase residuals of the low-cost antennas are reduced between 11.4% - 34% on L_1 and 19.5% - 38.7% on L_2, depending on the antenna type and ground plane used. The best performances, but the smallest improvements, are achieved when circular ground planes are used. For the cheapest antenna, when using a circular ground plane, the L_1 residual is reduced from 3.85 mm before to 3.41 mm after calibration, and for L_2 from 5.34 mm to 4.3 mm. The calibration reduced the Median Absolute Deviations (MADs) of the low-cost antennas in the vertical direction using Post Processed Kinematic (PPK) by 20.4% - 23.9%. For the cheapest antenna, the MAD was reduced from 5.6 to 3.8 mm, comparable to a geodetic-grade antenna (3.5 mm MAD). The calibration also had a positive impact on Precise Point Positioning (PPP) results, delivering more precise results and reducing height biases.

This chapter is submitted as: Krietemeyer, A.; van der Marel, H.; van de Giesen, N.; ten Veldhuis, M.-C. A field calibration solution to achieve high-grade level performance for low-cost dual-frequency receiver and antennas. GPS Solutions (2021)

5.1. INTRODUCTION

THE antenna is a crucial part of the Global Navigation Satellite System (GNSS) ground receiver setup. It is responsible for receiving the signals transmitted by GNSS satellites, transforming the electromagnetic energy into electric currents, and forwarding it to the GNSS receiver. In the case of phase observations, the estimated satellite range refers to an imaginary mean Antenna Phase Center (APC, Figure 5.1). To relate this phase center to a physical reference point on the antenna, the Antenna Reference Point (ARP) is used. It is typically defined as the intersection of the vertical symmetry axis with the bottom of the antenna ([1]). Figure 5.1 illustrates the antenna definitions. The offset between the ARP and the mean APC is called Phase Center Offset (PCO). In an ideal scenario, the phase pattern of an antenna is constant which introduces the same phase delay or advance in all directions. In reality, this phase pattern is irregular and depends on the antenna characteristics, environment and frequency ([2]). By fitting a sphere to the lines of constant phase, a phase center can be defined. The variations from this sphere to the line of constant phases are called Phase Center Variations (PCVs). Their magnitude typically ranges from several mm to a few cm ([3]) and are defined as a function of frequency and elevation- and azimuth angles. Apart from the antenna characteristics and environmental factors (multipath), also the cutoff angle and processing strategy influence the PCO and PCVs ([4]). It is common practice to define a phase center for each frequency, however it is also possible to use the same PCO for L_1 and L_2 by matching the PCV on the respective frequency accordingly.

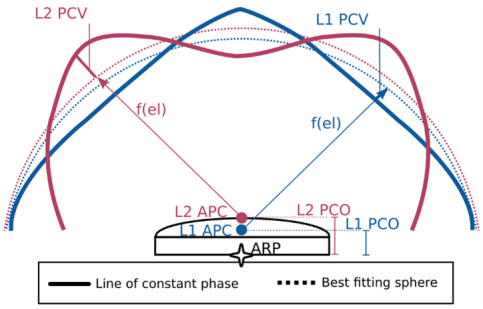

Figure 5.1: Schematic illustration of Antenna Reference Point (ARP), Antenna Phase Center (APC), lines of constant phase (solid lines) and best fitting spheres (dashed lines) on L_1 (blue) and L_2 (red). The Phase Center Variations (PCVs) are shown as functions of the elevation f(el) on the respective frequency.

To specify antenna characteristics, individual antennas need to be calibrated. One distinguishes between relative calibrations obtained from a base-rover setup and absolute calibrations obtained in the field with a robotic arm ([5], [6], [7]) or in an anechoic chamber ([8]) using artificial GNSS signals. By combining multiple individual calibrations of the same antenna model, type-mean calibrations can be generated. These calibrations are publicly available for an increasing number of geodetic antennas, e.g., by the International GNSS Service (IGS; [9]). With the advent of low-cost receiver and antenna setups for positioning or tropospheric delay analysis, there is a need for calibration of low-cost antennas. A recent study by Darugna *et al.* [10] found high PCVs of up to 2 cm on L_1 and 4 cm on L_5 after performing an absolute antenna calibration with a robotic arm

using a Huawei Mate20X dual-frequency smartphone. Hamza *et al.* [11] designed a 3D displacement detection test with a u-Blox ZED F9P receiver with ANN-MB-00 low-cost antennas and found minimum detectable displacements of 10 mm upwards. Calibrating low-cost antennas is essential to improve their performance, yet individual calibrations, e.g., by a robot, are costly and contradict the idea of low-cost solutions.

A low-cost solution is needed to fully exploit the potential of high-precision positioning applications using low-cost receiver and antenna setups for users of different disciplines (surveying, mapping of rivers, ground control points or atmosphere monitoring). This study uses a low-cost dual-frequency receiver (u-Blox ZED F9P) together with antennas of ranging quality and price (from 50 to 1000+ Euros). A relative antenna calibration ([4]) is performed. The assumption is that if two antennas with the same antenna phase pattern are used, these effects cancel over a short baseline. The differences are reflected in the estimated residuals by using different antennas for the base and rover. The obtained relative calibrations are converted to absolute ones by using a base station antenna with known antenna calibration. Performance of in-field calibrated low-cost receiver and antenna setups is demonstrated using static Precise Point Positioning (PPP) and Post Processed Kinematic (PPK) processing. The presented solution can be particularly interesting for areas where high-precision positioning is not available or application remains limited due to high costs. The implemented antenna calibration tool is made available online under gnss-antcal.citg.tudelft.nl. It allows users to calibrate their own antenna in the field, provided that a base antenna with known calibration is utilized.

In the next section, we describe the calibration procedure and performance. Then, we present the online tool, followed by a discussion of the obtained positioning results. Finally, we draw the conclusion and propose directions for future work.

5.2. CALIBRATION

THE main objective of this work is to develop a field calibration method for rover antennas. This section describes the experimental setup, the applied calibration method and analyzes the residual performance before and after calibration.

A series of short baseline experiments, consisting of a U-blox ZED-F9P receiver connected to different quality and type antennas (rover) together with the IGS station DLF1 (base), was conducted at the rooftop of the Netherlands Metrology Institute (NMi) in Delft. The rover antennas are installed consecutively on the mount point DOMES 13502M003 (GPS Mark 15) in about 10 m horizontal and 1.5 m vertical distance from the base station antenna. The installation situation is characterized by an almost unobstructed view over the full horizon and can be regarded as relatively clean regarding multipath and near-field effects. With a baseline length of approximately 10 meters, delays caused by the troposphere and ionosphere can be regarded as equal for base and rover. These effects can be considered canceled in the differential processing.

The base station consists of a Trimble NetR9 receiver connected to a Leica AR25.R3 (LEIAR) antenna with LEIT radome. The investigated rover antennas are the low-price antenna U-blox ANN-MB-00 (ANN-MB), the medium-priced antennas Trimble AV28 (AV28) and Trimble GA530 (GA530) and the geodetic quality antennas Trimble TRM55971.00 NONE, also known as Zephyr 2 Geodetic (TRM5) and Leica AR25.R3 LEIT

(same model as base station antenna). The antennas cover a price range from low (<$100) to high cost (>$1000). All rover antennas are connected to a U-blox ZED-F9P receiver. Because of the ANN-MB antenna designs (antenna without screw mount) and Trimble AV28 (screw-in hole mount), antenna mounting adaptors were constructed. One is a metallic, rectangular bracket, and the second one is a plastic bracket with a metallic circular disk of 10 cm diameter on top. Consequently, two datasets exist for these two antennas. Official IGS ANTEX type mean antenna calibrations exist for the highest quality rover antennas (LEIAR and TRM5).

The rover and base are operated with a 1 Hz logging interval. Base station data is obtained from the Dutch Permanent GNSS Array (DPGA) in 15-minute high-rate RINEX files and converted to daily 1 Hz data. Rover data is logged on a local SD card and converted to daily RINEX files for post-processing. Since not all antennas use the same antenna adaptor, the heights from the GPS mark to the antenna ARPs are measured manually. With exception of the circular adaptor which is off by 10 mm North and 8 mm East, only height offsets are introduced by the antenna adaptor. Though measured with care, the manual measurements have a precision error of about 1 mm.

The site-dependent factors (multipath) are unique for each installation and will influence the estimated parameters. They cannot be covered fully in absolute antenna calibrations except if the calibration is performed in the same spot as the experimental location. Apart from the residuals, only the positioning components and clock parameters are estimated. The residuals are therefore not sensitive to changes in position and clock drift.

The data processing is primarily realized using the open source tool RTKLIB ([12]). The applied processing options can be found in Table A1 in the supplementary file. To obtain Single Difference (SD) residuals, which are required to analyze the PCVs, the source code is modified to subtract the average of the Double Difference (DD) residuals from the DD residuals (see Github issue: [13]). We use GPS L_1 and L_2 observations exclusively to keep it simple and because most existing antenna calibrations to date are available for these frequencies. The ambiguity fixed residuals over three full observation days for all antennas, except ANN-MB with a circular adaptor which uses only two, are selected and stacked over 0.1° bins. The days were manually selected based on a visual inspection of the ambiguity fixed phase residuals. To investigate the effect of different averaging widths, the mean of the stacked residuals is applied to obtain elevation-only averages in the resolutions 0.1°, 1° and 5°. Beginning and end of the observations are filled with values from a 10th degree polynomial fitted to the 0.1° data. The order of the polynomial was chosen after tests with lower order polynomials. The elevation-only approach is preferred over an azimuth- and elevation dependent approach since the observation period is short and no antenna rotation was performed to cover all parts of the antenna. A previously conducted test with both methods also revealed a slight performance decrease in the ZTD estimation ([14]) using the latter. A figure illustrating the elevation-only phase residuals can be found in the supplementary material.

To apply the antenna corrections, the averaged relative residuals could be added directly to the rover observations. However, this would limit the application to the analyzed baseline and could not be applied to other locations. By adding the known base station antenna (LEIAR25.R3 LEIT) PCVs, the relative residuals are converted to absolute

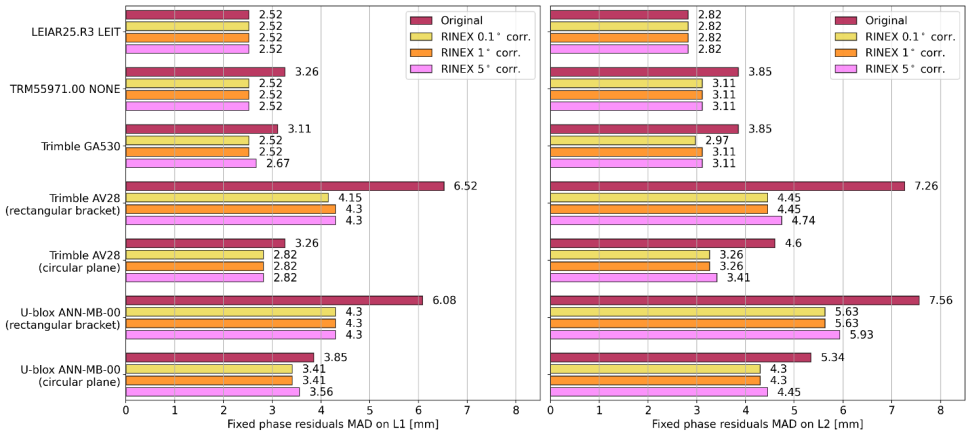

Figure 5.2: Ambiguity fixed phase residuals on L_1 (left) and L_2 (right) before and after the calibration using 0.1°, 1° and 5° binning widths

5

ones. We use the IGS type mean ANTEX entry file (I14.ATX) for this purpose. A new ANTEX entry for each investigated antenna is generated. Since three different resolutions are investigated, a new ANTEX file is created for each of them. To further generalize the presented method and since not all processing engines allow to supply own ANTEX files to their processing chain, the base and rover RINEX files are manipulated according to the PCVs of their respective antennas. We adjust the phase data using the following formula:

$$\tilde{L}_i = L_i - \frac{\varphi_i^r(el, az)}{\lambda_i} \tag{5.1}$$

with $\tilde{L}_i$ being the corrected phase data on frequency i and L_i the original RINEX phase observation. The azimuth and elevation-dependent ANTEX PCV correction $\varphi_i^r(el, az)$ is scaled by the wavelength λ_i.

To investigate the performance of the antennas after applying the corrections to the base and rover RINEX files, another PPK run over the same short baseline is performed. As metric for the comparison, we use a robust estimator of the standard deviation, the Median Absolute Deviation (MAD):

$$MAD = 1.4826 \cdot median(|x_i - \tilde{x}|) \tag{5.2}$$

The variables x_i and $\tilde{x}$ depict the observations and the median of the data. The scale factor of 1.4826 is constant and is multiplied by the median of the absolute deviations. The scale relates to the underlying assumption of normal distributed data. Compared to the standard deviation, the MAD is more resistant to outliers and, therefore, our preferred measure in this study. The MADs of the ambiguity fixed phase residuals before and after calibration is illustrated in Figure 5.2.

The MAD of the ambiguity fixed phase residuals are generally lower for the more expensive antennas and higher for the lower cost antennas. The highest quality antenna

(LEIAR) results in the lowest phase residuals (MAD of 2.52 mm on L_1 and 2.82 mm on L_2) which also remain unchanged after correcting the input data. Compared to LEIAR, which was also used by the base, the TRM5 and GA530 have before correction a MAD on L_1 that is 29% and 23% higher, and 36% higher on L_2. After correction, the MAD on L_1 is of the same level and just slightly above on L_2. For the lower cost antennas AV28 and ANN-MB with a circular ground plane, the MAD on L_1 before correction is respectively 29% and 53% above the reference antenna, and on L_2 respectively 63% and 89%. After adjusting the phase data, these numbers are reduced to a difference of 12% and 35% on L_1 and 16% and 52% on L_2. The results with a rectangular adaptor demonstrate the highest deviations but also the highest improvements (from about 150% down to 60-100%). Though considerably improved, the performance is clearly below its counterparts utilizing a circular ground plane. Interestingly, the different resolutions of the applied PCV corrections only marginally affect the outcome. Compared to the results without calibrations and depending on the antenna type and ground plane, the residuals of the low-cost antennas were reduced by 11.4% - 34% on L_1 and 19.5% - 38.7% on L_2.

The results suggest that, even after correction, noise is still present in the data, due to effects not captured by the elevation-only based calibration. To further examine the effectiveness of the elevation-only averaging, we calculate the semivariance $\hat{\gamma}$ (see e.g. [15]) for each antenna before and after calibration over the full elevation and azimuth horizon to determine if only white noise is left in the residuals:

$$\hat{\gamma}(d) = \frac{1}{2N(d)} \sum_{||u_i - u_j||} (z(u_i) - z(u_j)^2 \tag{5.3}$$

where $N(d)$ is the number of data pairs belonging to the data bin d and z are the paired observations at spatial locations u separated by the euclidean distance $||u_i - u_j||$. We conduct the grouping by separating the data points into bins of distinct distances using the 1° resolution averages. Figure 5.3 2D variogram maps of the antennas TRM5 and AV28 with circular and rectangular adaptor using L_1 observations before and after applying the corrections. Each pixel shows the averaged semivariance over 4° and covers the spatial variance over up to 30° azimuth and 30° elevation difference.

All antennas have in common that the semivariance generally decreases after removing the elevation pattern. However, the residuals are still correlated (low semivariance) over short distances, independent of removing the antenna pattern. This is an indication that remaining errors are not just white noise. After removal of the elevation pattern (calibration), the semi-variance for the TRM5 antenna is the smallest, with reduced correlation in both elevation and azimuth direction, especially in elevation. This is followed by the AV28 antenna with circular ground plane. For the AV28 antenna, with a rectangular adaptor, azimuth- and elevation specific artifacts remain that could only partially be covered by the calibration. The semivariogram maps of all antennas can be found in the electronic supplementary file.

5.3. ONLINE WEB SERVICE

THE presented calibration method is implemented as an online web tool (gnss-antcal.citg.tudelft.nl). An antenna calibration can therefore be directly performed

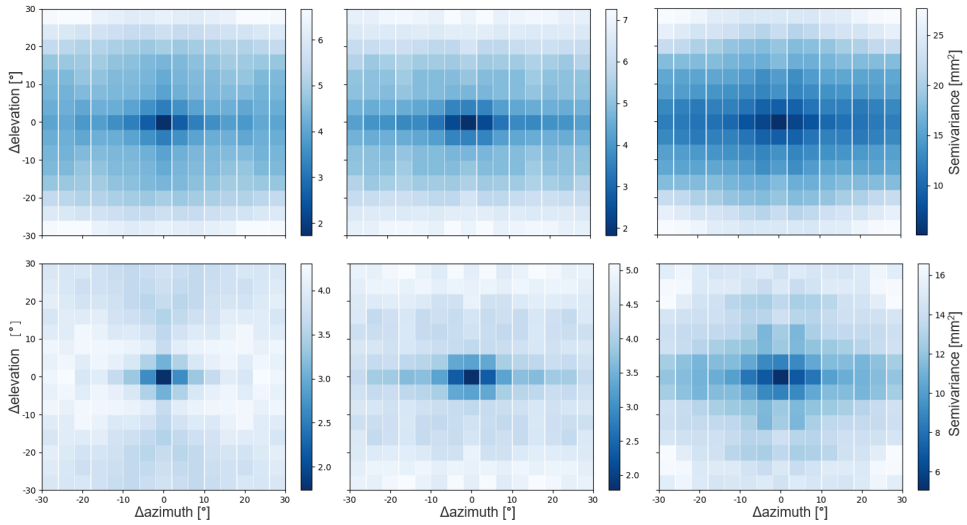

Figure 5.3: 2D variogram maps of the residuals for the antennas TRM5 (left), AV 28 circular ground plane (middle) and AV28 rectangular adaptor (right), before (top) and after (bottom) removing the elevation pattern

by the user in the field.

To calibrate a rover antenna with the online calibration tool, a simple base-rover setup is required. The base station antenna must be an already calibrated antenna with available calibration patterns in the current type mean IGS ANTEX file or in an external ANTEX file. For the best results, both antennas are placed over a very short baseline and the rover antenna is installed at the location as it is intended to stay after the calibration. In any way, both antennas should be installed in a preferably multipath-free environment with no or only small height differences between them. The tool in its current state only accepts RINEX3 files that cover a maximum of one full day. The user is advised to format the input data accordingly to avoid rejection of the input data by the software. On the website, an explanation page highlighting the requirements is provided. The basic specifications and features of the tool are illustrated in Figure 5.4.

The user can provide the base antenna name separately or specify it in the RINEX header. If no custom ANTEX file is supplied, the currently available IGS ANTEX I14.ATX is used. The name of the base antenna must be in the ANTEX file. The user is also required to supply the rover RINEX header with an antenna name. The recommended maximum sampling frequency should not exceed 1Hz. The user is encouraged to upload GPS-only observations with L_1 and L_2 observations as these are the only frequencies that are currently supported by the tool. However, also multi-GNSS observations can be uploaded but will not be utilized by the current processing scheme. The program will output the computed baseline between base and rover antenna in local coordinates (North, East, and Up) as well as an ANTEX entry containing the PCVs. To be consistent with the ANTEX notation, an averaging of 5° is chosen. If the height difference between the ARP of the base antenna and the ARP of the rover antenna is provided by the user (mm level), the estimated median height offset will be reported as PCO in the ANTEX entry on both

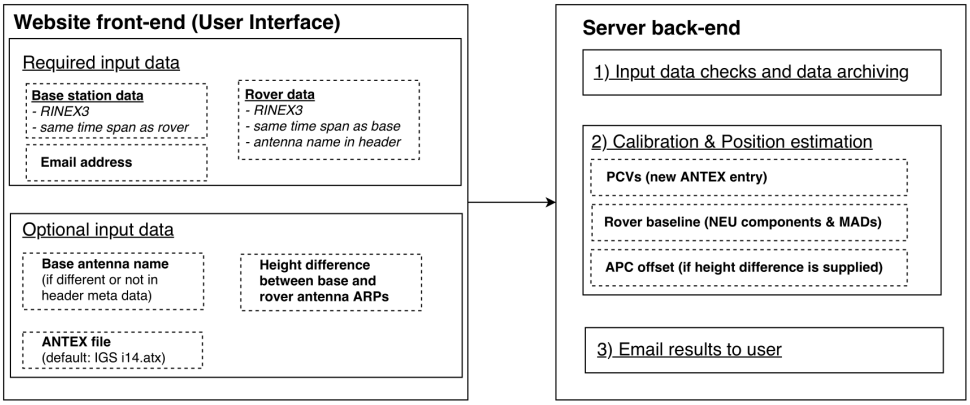

Figure 5.4: Overview of the web-tool requirements and functions

supported frequencies.

5.4. POSITIONING ANALYSIS

To evaluate the performance of the calibration method, this section analyzes the positioning results from the investigated antennas using static PPP and kinematic PPK, with and without applying the antenna calibrations. The main focus is set to the height estimation. Results for the horizontal components can be found in the supplementary document. As mentioned before, only GPS L_1 and L_2 observations are used. The high-quality LEIAR25.R3 LEIT antenna serves as a reference for our analysis. The same model is also used as base station antenna which eliminates antenna-induced effects in the differential PPK processing. Unless mentioned otherwise, 1° resolution.

5.4.1. NRCAN PPP RESULTS

With the online service NRCan PPP ([16]), the ionosphere-free linear combination of L_1 and L_2 phase observations (L_IF) is applied. The resulting mean phase center is consequently adjusted to the linear combination of the L_1 and L_2 phase centers. This experiment allows us to estimate the L_IF PCO and the impact of the PCVs on the height estimations. The NRCan service uses IGS products and applies the type mean antenna phase center corrections from the current IGS ANTEX file. The estimated height of the rover LEIAR antenna, with antenna corrections from the IGS ANTEX file applied by the PPP engine, is used as the reference value for the height. Also for the TRM5 antenna, which has an entry in the IGS ANTEX file, the PPP engine applies antenna corrections automatically. This antenna serves as an additional reference. With the known L_1 and L_2 PCOs, the L_IF PCO can be calculated:

$$PCO_{L_{IF}} = C_1 \cdot PCO_{L1} + C_2 \cdot PCO_{L2} \tag{5.4}$$

$$C_1 = \frac{f_1^2}{f_1^2 - f_2^2}, C_2 = -\frac{f_2^2}{f_1^2 - f_2^2} \tag{5.5}$$

Antenna/Case	LEIAR	TRM5
No receiver PCO/PCVs [mm]	183	71
Automatic IGS PCO and PCV [mm]	0	-8
Manual IGS PCV-only [mm]	167	72

Table 5.1: PPP height estimation differences to the automatically applied IGS ANTEX corrections of the LEIAR antenna in mm, using 5° angular resolution

with f_1 and f_2 being the L_1 and L_2 frequencies.

The PPP analysis is done by submitting several dual-frequency RINEX files of one full day. Since the high-rate (1Hz) data sampling rate is not required for the static PPP processing, the data is down-sampled to 30-second interval. Ocean loading parameters for the station location from the FES2004 model ([17]) are provided in an external file. Final GPS orbit and clock parameters are used by the engine. Suppose the antenna name is given in the RINEX header metadata and an entry for this antenna (and radome) exists in the IGS ANTEX file. In that case, the antenna corrections (PCO and PCVs) are automatically applied to the receiver antenna. The engine also applies the satellite antenna corrections. Except for the input RINEX data, all conducted tests use the same configuration parameters.

To verify the implementation of the corrections to the RINEX data, the reference antennas LEIAR and TRM5 are processed by the PPP engine using different input data configurations. The results can be found in Table 5.1.

The first line shows the offsets using the original RINEX data without antenna metadata. No receiver antenna correction is applied and therefore yields the position of the mean phase centers of the L_IF of the combined PCO and PCV effects. The resulting offsets are 183 and 71 mm. The second line shows the height differences with automatically applied IGS PCO and PCV corrections. Obviously, no height error is found for the LEIAR antenna since it serves as our reference measurement. A difference of -8 mm compared to the LEIAR ARP position is observed for the second antenna. Though the same mounting adaptor was used for both antennas, this antenna could not be fully screwed into the screw hole and the height offset was measured manually and corrected by 10 mm. The higher uncertainty of the manually measured height could play a role in this observed offset, but another, more likely reason is that because the LEIAR and TRM5 were mounted on different days, the difference is simply due to noise in the data. The third line shows the height differences after manually applying the IGS ANTEX PCV (but no PCO) corrections to the RINEX files according to equation 5.1. The RINEX modification is necessary since it is not possible to supply your own ANTEX file to the NRCan online service. To be consistent with the IGS ANTEX resolution, this analysis is performed using an angular resolution of 5°. The resulting offsets respect the PCVs and return an estimate of the L_IF PCOs. The result of the LEIAR antenna is equal to the IGS ANTEX L_IF PCO of 167 mm. In the case of the TRM5 antenna, the L_IF PCO according to the ANTEX entries is 80 mm. Compared to the manually PCVs applied result of 72 mm, a bias of 8 mm persists, which is consistent with the result on the second row. Except for the 8 mm difference in the TRM5 due to using data from different days, the agreement of the L_IF

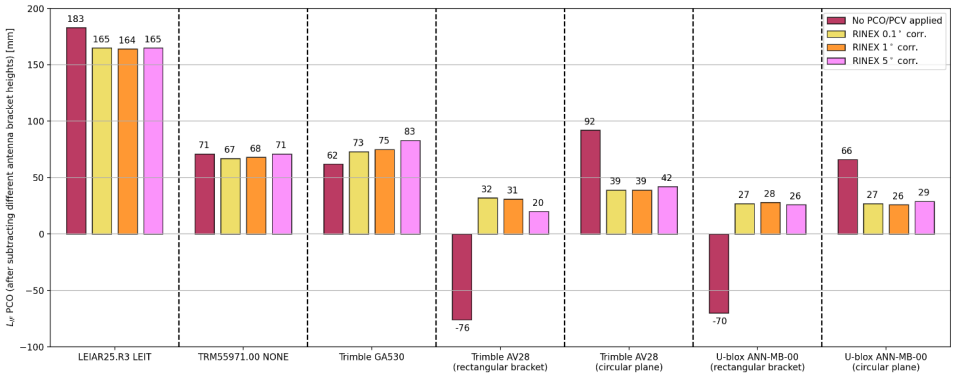

Figure 5.5: PPP height differences to the reference height before and after applying the PCV corrections

5

PCOs indicate the successful implementation of the manual PCV correction to the input RINEX observations.

Since no official calibrations are freely available for the remaining antennas, they could not be compared against an absolute reference. However, by accounting for the different adaptor heights, the height estimations can be compared. Figure 5.5 shows the height offsets from the GPS Marker height using the original data without supplying the antenna type in the RINEX header and after correcting the RINEX data with the estimated PCV corrections in 0.1°, 1° and 5° resolution. Since we compare with a known height and do not apply corrections for the PCO, the observed height offsets can be interpreted as an L_IF PCO estimate.

The first thing to look at is the height difference with and without applying receiver antenna PCV corrections. For the LEIAR antenna the difference is 18 mm, whilst the TRM5 antenna demonstrates almost no changes with or without the PCV correction. It means that the phase variations from the TRM5 antenna must be close to a circular constant phase pattern, while the LEIAR and other antennas apparently deviate more from a circular pattern which eventually results in the observed height offset. It is known that radomes, such as the one used by the LEIAR, can have an impact on the station height of several cm (see also [18]). Also, the effect of applying PCV corrections is much higher for both lower cost antennas (AV28, AMN-MB) than for the more expensive antennas (LEIAR, TRM5 and GA530). The lower cost antennas AV28 and ANN-MB are characterized by high offsets of 92 and 66 mm before applying the PCV corrections. After applying the corrections, the estimated L_IF PCOs are reduced to 26 and 39 mm, which appear rather reasonable. Interestingly, when a rectangular adaptor is utilized before calibration, the offsets are of opposite sign but in the same order of magnitude of about -70 mm. After calibration, they are reduced to about the same level as the results with a circular ground plane with offsets of 31 and 28 mm. Especially the fact that the offsets with the same antenna but with different mounting adaptors differ between 17 and 14 cm before correction and only up to 1 cm after the correction appears promising.

The results for various resolution bins (averaging width) do not vary significantly, with values between 1 and up to 4 mm, except for the GA530 antenna and AV28 antenna

with a rectangular adaptor in combination with a bin size of 5°. The latter could be due to a measurement outlier or caused by substantial PCV differences presumably caused by the near-field effects on the edges of the rectangular adaptor, that might be better represented at the finer scale but may behave poorly in case of the 5° averaging method.

5.4.2. RTKLIB PPK RESULTS

Post processed kinematic (PPK) positioning results, with and without antenna PCV corrections, are obtained using RTKLIB. The correction is performed by modifying both base and rover RINEX datasets with the absolute PCVs. However, the same effect can be achieved by correcting the rover data with the residuals obtained from the calibration. We provide results with different averaging widths used by the calibration procedure (0.1°, 1° and 5°). One full day is processed for each antenna and only ambiguity fixed estimations are used. Same as in the calibration step, the IGS station DLF1 is used as the base station. Errors caused by the troposphere or ionosphere are assumed equal and eliminated in the process. Other parameters, i.e. positioning components or clock errors, are estimated. One of the main goals of antenna calibration is to increase the repeatability of kinematic position solutions. We, therefore, analyze the positioning performance by computing the MAD of the kinematic North, East and Up (NEU) components, with the results for the vertical component given in Figure 5.6. For each run, also the median offset in the NEU components is computed, using the L_1+L_2 RTKLIB solution with the two - base and rover - LEIAR antennas as a reference, with results for the vertical component given in Figure 5.7. These provide estimates of the "L_1+L_2" PCO. Processing in RTKLIB can be done with L_1 only, or L_1+L_2 combined. To use all observations the L_1+L_2 option is used, but this results in a single L_1+L_2 position estimate (likewise, for the calibration itself, L_1+L_2 processing is used to obtain residuals for both L_1 and L_2). In the ANTEX files only separate L_1 and L_2 PCOs are available, but the combined PCO for L_1+L_2, which depends on the weighting applied in RTKLIB, is not available. However, this does not matter here, as in our calibration procedure the PCVs are given with respect to the combined L_1+L_2 PCO, and there is no reason why the L_1 and L_2 PCO cannot be the same as long as it is consistent with the provided PCV for each frequency. Another useful observation to make here, is that positioning results are not sensitive to a constant shift of the PCV: any constant that is added to the PCV is absorbed by the clock estimate in the positioning estimate. This means that we can have PCO/PCV calibrations for which the L_1 and L_2 PCO are the same, but the L_1 and L_2 PCV at zenith is zero, as is the case in our calibrations.

The MAD for the kinematic Up component from the L_1+L_2 solution is illustrated in Figure 5.6. Results containing the horizontal components and L_1-only results can be found in Tables A2-A4 in the supplementary file.

For the results without antenna phase center corrections, the highest cost antennas (LEIAR, TRM5 and GA530) have the smallest vertical MADs. They vary around 3 to 4 mm. The AV28 and ANN-MB antennas yield 5.6 and 5.2 mm, respectively. More importantly, after applying the corrections to the data, the precision always increased (or remained equal as in the reference LEIAR case). After correcting, the MAD for the higher cost TRM5 and GA530 antennas was reduced to 3.6 and 3.4 mm, getting close the LEIAR result (3.3 mm). The MAD of the AV28 and ANN-MB antennas were lowered significantly by 31%

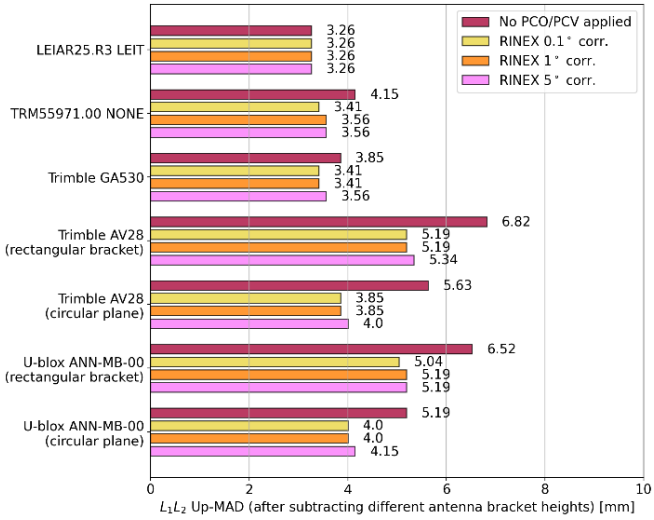

Figure 5.6: RTKLIB PPK Up-component MADs before and after input data correction

(3.9 mm) and 23% (4 mm), respectively. This is particularly promising since it brings them to an almost comparable level to the more expensive antennas.

The two cases with a rectangular adaptor showed the highest deviations but also the highest improvements after calibration, from 6.8 and 6.5 mm MAD down to 5.2 mm. Though the performance is not equal to the corrected results with a circular ground plane, they are on the same level as the uncorrected circular ground plane results and demonstrate the potential to significantly lower the multipath effects by using the proposed method.

The corrections with 5° binning size perform slightly worse than the higher resolution ones. However, only little differences are visible between the 0.1° and 1° binning size results. It implies that the highest resolution of 0.1° is not necessary, and that the 1° binning size appears to be a good trade-off between additional computing time requirements and smoothing potential outliers in the observations.

The median PCO height estimations using L_1+L_2 observations, before and after correcting for the PCVs, are illustrated in Figure 5.7.

The first thing to observe is that the estimated PCO for each antenna are quite consistent, even when no PCO/PCV is applied. This is quite understandable as our PCVs are computed from residuals from another RTKLIB processing, and the residuals are with respect to the L_1+L_2 position estimate using only a calibration for the base antenna. For the LEIAR and TRM5 antenna L_1+L_2 PCO values can be compared against L_1 and L_2 PCO values given by the IGS ANTEX file. Compared to the IGS ANTEX L_1 PCO (161.70 mm) and L_2 PCO (157.94 mm), our L_1+L_2 PCO for the LEIAR corrected case is 0.7 and 4.5 mm above the IGS L_1 and L_2 PCO. For the TRM5 antenna (L_1=66.73, L_2=57.69) this is respectively 2.2 and 11.2 mm after calibration. Clearly, our L_1+L_2 PCO estimate is closer to the IGS ANTEX L_1 than the L_2 estimate. According to the technical drawing on the

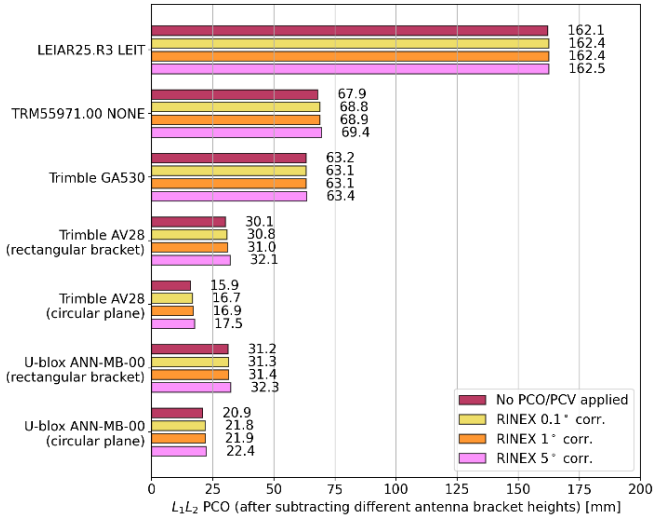

Figure 5.7: PPK estimated L_1L_2 Up-component offsets

side of the GA530 antenna, the PCO equals 78.3 mm. Our estimation of about 63 mm indicates an underestimation of the PCO. An external U-blox document ([19]) gives an L_1 PCO of 8.9 mm in the Up direction utilizing a 120 mm circular diameter ground plane. Using a circular ground plane of 100 mm, the results demonstrate L_1+L_2 PCOs of 20.9 before and 21.9 mm after calibration. Apart from using a different definition of the PCO, making comparisons meaningless, other contributing factors to these "discrepancies" are the applied elevation cutoff angle of 5°, different processing strategies (kinematic in the evaluation and static in the calibration) or a systematic error caused by erroneous manual height measurements. A likely reason for the difference in the ANN-MB case is the diameter of the ground plane having a direct influence on the obtained PCO. The special case scenarios utilizing a rectangular adaptor yield offsets of 30.1 and 31.2 mm before and 31 and 31.4 mm after correction. The main message we can take from these comparisons is that our L_1+L_2 PCO is consistent with using no PCV corrections, while the PCVs we provide are with respect to the same "phase center" as obtained without calibration, and – for reasons we do not fully understand - our L_1+L_2 PCO is probably closer to L_1 than the L_2 PCO.

5.5. CONCLUSION

THIS work aims to provide a simple-to-apply cost-efficient calibration method that improves antenna performance, especially for low-cost antennas. We present a field calibration procedure that is implemented and made available online as a web service (gnss-antcal.citg.tudelft.nl). It gives users the possibility to conduct an antenna calibration on their own, which opens the way for high precision positioning with low-cost equipment. In this paper, we analyzed the quality and remaining residuals in the an-

tenna calibration procedure and demonstrated the positioning performance in PPP and PPK applications with five antennas of different quality and price.

The analysis of the ambiguity fixed phase residuals before and after the conducted calibration demonstrates a clear reduction of the MAD for all antennas. Comparing the residuals before calibration to the results of our reference antenna LEIAR25.R3 LEIT, the lower priced antenna AV28 was on average off by 0.74 mm (29%) on L_1 and 1.78 mm (63%) on L_2. For ANN-MB these are 1.33 mm (53%) on L_1 and 2.52 mm (89%) on L_2. After calibration, the AV28 residuals could be reduced to a difference of 0.3 mm (12%) on L_1 and 0.44 mm (16%) on L_2. For ANN-MB, these were 0.89 mm (35%) on L_1 and 1.48 mm (52%) on L_2. In comparison, the higher-grade antennas TRM5 and GA530 were off by 0.74 mm (29%) and 0.59 mm (23%) on L_1 and 1.03 mm (36%) on L_2 before application of the calibration procedure and could be reduced to the same level of the reference antenna on L_1 and close to 0.29 mm (10%) on L_2.

With the implemented elevation-based residual averaging method, the phase pattern could be captured for a great part for all antennas. However, some distinctions can be made. It occurs that the TRM5 and GA530 are characterized by an almost circular phase pattern over the full horizon, whilst the lower priced antennas AV28 and ANN-MB indicate a greater azimuthal dependency.

The calibration efficiency of all antennas is demonstrated by evaluating the positioning stability and offsets. First, we investigated the PCV influence and estimated the positioning offsets on the ionosphere-free linear combination phase center in PPP. A height offset of 92 mm and 66 mm was observed for the lower priced antennas AV28 and ANN-MB before calibration. After calibration, the offsets were reduced to about 40 mm and 27 mm, respectively. Interestingly, the same antennas on a rectangular adaptor that yield height offsets of -76 and -70 mm before calibration were transformed to similar positive offsets of approximately 30 and 27 mm after calibration. Second, the kinematic positioning stability was analyzed over a short baseline in PPK. Similar to the residual performance, we observed the best positioning stability performance for the highest quality antennas. Comparably, the lower priced antennas demonstrated higher variance but improved significantly after the calibration. The MADs in the vertical direction of the low-cost antennas were reduced by 20.4% - 23.9%. For the AV28 antenna, they were lowered from 5.6 mm to 3.8 mm. For ANN-MB-00 they were brought from 5.2 mm to 4 mm. It brings them to a level close to the performance of the antennas LEIAR, TRM5 and GA530, which are characterized by MADs of 3.3, 4.1 and 3.8 mm before and 3.3, 3.6 and 3.4 mm after calibration.

The special case scenario consisting of the antennas AV28 and ANN-MB with a metallic rectangular adaptor demonstrated the highest deviations, the strongest azimuthal dependency, but also the greatest improvements in all cases.

Examining different binning widths of 0.1°, 1° and 5° for the elevation-based averaging method revealed in some cases a slight performance decrease of the standard 5° resolution over the 1° and 0.1° binning widths. Given the presence of the higher amount of potential outliers in the 0.1° and the increased computational costs, the 1° resolution appears to be a good trade-off between effectiveness and smoothing.

The reported PCOs of the PPK process are given with respect to the combined L_1+L_2 PCO and are close to the L_1 PCO. They are consistent with using no PCV corrections,

while the estimated PCVs are with respect to the same phase center as obtained without calibration. Compared to the PPP results, the estimated PCOs estimated by the online web service of the tested antennas are off between zero and 22.1 mm. The presented PCO estimations are subject to improvement due to uncertainty introduced by the manual height measurement. However, even without respecting the PCO, the estimated PCVs are strongly beneficial for deformation or atmosphere monitoring. Further testing using multiple frequencies could widen the application from the current GPS-only to all GNSS frequencies. The provided PCVs and PCOs and the online service to perform the antenna calibrations in the field can be helpful for widespread application of low-cost antenna and receiver setups for high precision applications.

REFERENCES

[1] B. Hofmann-Wellenhof, H. Lichtenegger, and E. Wasle, *GNSS-Global Navigation Satellite Systems: GPS, GLONASS, Galileo, and more* (Springer Science & Business Media, 2007).

[2] A. Leick, L. Rapoport, and D. Tatarnikov, *GPS Satellite Surveying* (John Wiley & Sons, 2015).

[3] B. R. Schupler, T. A. Clark, and R. L. Allshouse, *Characterizations of GPS user antennas: Reanalysis and new results,* GPS Trends in Precise Terrestrial, Airborne, and Spaceborne Applications , 328 (1996).

[4] G. L. Mader, *GPS antenna calibration at the National Geodetic Survey,* GPS solutions **3**, 50 (1999).

[5] G. Wübbena, M. Schmitz, F. Menge, V. Böder, and G. Seeber, *Automated absolute field calibration of GPS antennas in real-time,* ION GPS **2000**, 2512 (2000).

[6] A. Riddell, M. Moore, and G. Hu, *Geoscience Australia's GNSS antenna calibration facility: Initial results,* Proceedings of the IGNSS Symposium, Miami, Australia , 14 (2015).

[7] D. Willi, S. Lutz, E. Brockmann, and M. Rothacher, *Absolute field calibration for multi-GNSS receiver antennas at ETH Zurich,* GPS Solutions **24**, 1 (2020).

[8] B. Görres, J. Campbell, M. Becker, and M. Siemes, *Absolute calibration of GPS antennas: laboratory results and comparison with field and robot techniques,* GPS solutions **10**, 136 (2006).

[9] J. Dow, R. Neilan, and C. Rizos, *The International GNSS Service in a changing landscape of Global Navigation Satellite Systems,* Journal of Geodesy **83**, 191 (2009).

[10] F. Darugna, J. B. Wübbena, G. Wübbena, M. Schmitz, S. Schön, and A. Warneke, *Impact of robot antenna calibration on dual-frequency smartphone-based high-accuracy positioning: a case study using the Huawei Mate20X,* GPS Solutions **25**, 15 (2020).

[11] V. Hamza, B. Stopar, T. Ambrožič, G. Turk, and O. Sterle, *Testing Multi-Frequency Low-Cost GNSS Receivers for Geodetic Monitoring Purposes,* **20**, 4375 (2020).

[12] T. Takasu, *RTKLIB: An Open Source Program Package for GNSS Positioning,* https://github.com/tomojitakasu/RTKLIB (2019), accessed: 2019-06-03.

[13] T. Takasu, *RTKLIB github issue tracker,* `https://github.com/tomojitakasu/RTKLIB/issues/457#issuecom\ment-473523905` (2019), accessed: 2019-06-03.

[14] A. Krietemeyer, H. van der Marel, N. van de Giesen, and M.-C. ten Veldhuis, *High Quality Zenith Tropospheric Delay Estimation Using a Low-Cost Dual-Frequency Receiver and Relative Antenna Calibration,* Remote Sensing **12**, 1393 (2020).

[15] G. Matheron, *Principles of geostatistics,* in *Economic Geology*, Vol. 58 (Society of Economic Geologists, 1963) pp. 1246–1266.

[16] NRCan, *Canadian Spatial Reference System Precise Point Positioning tool (CSRS-PPP),* `https://webapp.geod.nrcan.gc.ca/geod/tools-outils/ppp.php?locale=en` (2020), accessed: 2020-08-06.

[17] F. Lyard, F. Lefevre, T. Letellier, and O. Francis, *Modelling the global ocean tides: modern insights from FES2004,* Ocean Dynamics **56**, 394 (2006).

[18] K. Kaniuth and K. Stuber, *The impact of antenna radomes on height estimates in regional GPS networks,* Vertical Reference Systems , 101 (2002).

[19] Ublox, *ANN-MB series Multi-band, high precision GNSS antennas: Data Sheet,* `https://www.u-blox.com/sites/default/files/ANN-MB_DataSheet_%28UBX-18049862%29.pdf` (2019), accessed: 2020-08-06.

SUPPLEMENTARY MATERIAL

Table A1: RTKLIB (RNX2RTKP) processing options.

Option	Parameter
Positioning solution	Static (-p 3)
Elevation cut-off	5° (-m 5)
Ambiguity Resolution (AR)	Fix-and-hold (-h)
AR validation Threshold	3 (-v 3.0)
Output positioning	East, North, Up (-a)
Statistics output	Residuals (-y 2)
Satellite system	GPS-only (-sys G)
Time format	YYYY/MM/DD (-t)
Kalman filter	Forward + backward (-c)

Table A2: RTKLIB PPK North component MADs in mm using L1 and L2 data (L1L2 column) and L1-only observations (L1-only column). The uncorrected results (no corr.) are shown on the left. The columns on the right (Δcorrected) show the MAD decrease (indicated by a '-'sign) after applying the elevation-only based calibrations with the averaging resolutions 0.1°, 1° and 5°.

	MAD [mm]							
	L1L2				L1-only			
Antenna	no corr.	Δ corrected			no corr.	Δ corrected		
		0.1°	1°	5°		0.1°	1°	5°
LEIAR25.R3 LEIT	1.9	±0.0	±0.0	±0.0	2.2	±0.0	±0.0	±0.0
TRM55711.00 NONE	2.2	-0.3	-0.1	-0.1	2.7	-0.6	-0.6	-0.6
Trimble GA530	2.2	-0.1	-0.1	-0.1	2.7	-0.4	-0.4	-0.4
Trimble AV28 (rectangular bracket)	4.2	-0.9	-0.9	-0.7	4.6	-0.7	-0.7	-0.7
Trimble AV28 (circular bracket)	2.7	-0.6	-0.6	-0.6	2.4	-0.1	±0.0	±0.0
U-Blox ANN-MB-00 (rectangular bracket)	4.7	-1.2	-1.2	-1.2	4.7	-0.9	-0.9	-0.9
U-Blox ANN-MB-00 (circular bracket)	3.0	-0.3	-0.3	-0.3	3.0	-0.2	-0.2	-0.2

Table A3: RTKLIB PPK East component MADs in mm using L1 and L2 data (L1L2 column) and L1-only observations (L1-only column). The uncorrected results (no corr.) are shown on the left. The columns on the right (Δcorrected) show the MAD decrease (indicated by a '-'sign) after applying the elevation-only based calibrations with the averaging resolutions 0.1°, 1° and 5°.

	MAD [mm]							
	L1L2				L1-only			
Antenna	no corr.	Δ corrected			no corr.	Δ corrected		
		0.1°	1°	5°		0.1°	1°	5°
LEIAR25.R3 LEIT	1.3	±0.0	±0.0	±0.0	1.6	-0.1	±0.0	±0.0
TRM55711.00 NONE	1.5	±0.0	±0.0	±0.0	1.8	-0.2	-0.2	-0.2
Trimble GA530	1.5	-0.1	-0.1	-0.1	1.8	-0.2	-0.2	-0.2
Trimble AV28 (rectangular bracket)	2.8	-0.7	-0.6	-0.6	3.9	-1.3	-1.3	-1.2
Trimble AV28 (circular bracket)	1.8	-0.2	-0.2	-0.2	1.8	-0.2	±0.0	±0.0
U-Blox ANN-MB-00 (rectangular bracket)	3.4	-1.0	-1.0	-0.9	4.3	-1.8	-1.8	-1.6
U-Blox ANN-MB-00 (circular bracket)	2.4	-0.3	-0.3	-0.3	1.9	±0.0	±0.0	±0.0

Table A4: RTKLIB PPK Up component MADs in mm using L1 and L2 data (L1L2 column) and L1-only observations (L1-only column). The uncorrected results (no corr.) are shown on the left. The columns on the right (Δcorrected) show the MAD decrease (indicated by a '-'sign) after applying the elevation-only based calibrations with the averaging resolutions 0.1°, 1° and 5°.

	MAD [mm]							
	L1L2				L1-only			
Antenna	no corr.	Δ corrected			no corr.	Δ corrected		
		0.1°	1°	5°		0.1°	1°	5°
LEIAR25.R3 LEIT	3.3	±0.0	±0.0	±0.0	3.6	-0.1	±0.0	±0.0
TRM55711.00 NONE	4.2	-0.7	-0.6	-0.6	4.7	-1.0	-1.0	-0.9
Trimble GA530	3.9	-0.4	-0.4	-0.3	4.6	-0.7	-0.7	-0.7
Trimble AV28 (rectangular bracket)	6.8	-1.6	-1.6	-1.5	7.4	-1.3	-1.2	-1.2
Trimble AV28 (circular bracket)	5.6	-1.8	-1.8	-1.6	5.3	-1.2	-1.2	-1.2
U-Blox ANN-MB-00 (rectangular bracket)	6.5	-1.5	-1.3	-1.3	7.3	-1.8	-1.8	-1.6
U-Blox ANN-MB-00 (circular bracket)	5.2	-1.2	-1.2	-1.0	5.6	-0.7	-0.7	-0.7

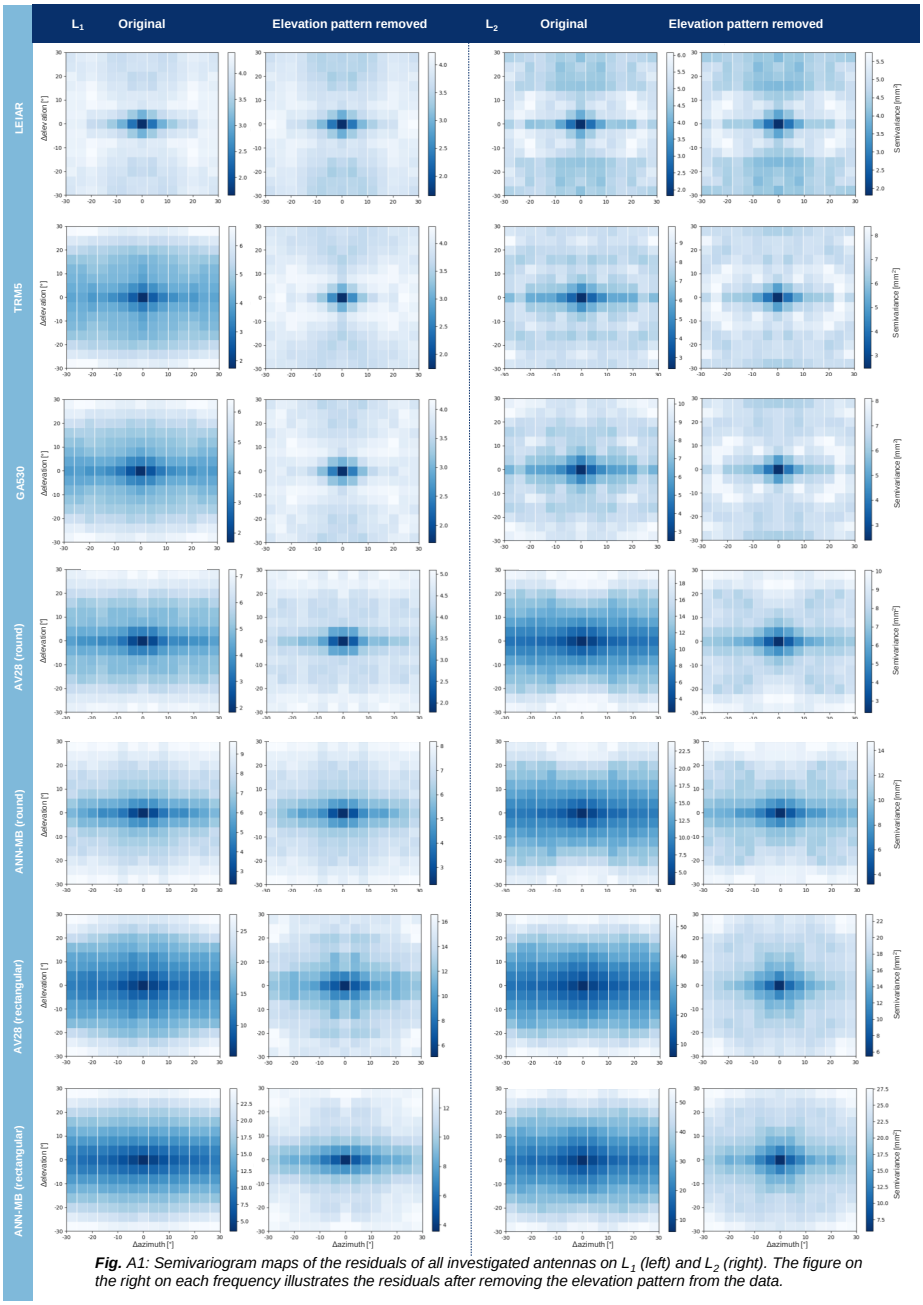

Fig. *A1: Semivariogram maps of the residuals of all investigated antennas on L_1 (left) and L_2 (right). The figure on the right on each frequency illustrates the residuals after removing the elevation pattern from the data.*

5

6

CONCLUSION

THE use of Global Navigation Satellite Systems (GNSS) ranges from 3D-positioning to meteorological applications. A key point for this thesis are the meteorological opportunities that GNSS provides. With the observed signal delays caused by the earth's atmosphere between the transmitting satellites and the receiver antenna, information about the state of the atmosphere can be obtained. One component of the time difference is the so-called Zenith Tropospheric Delay (ZTD) which provides information about the amount of water vapor in the atmosphere. ZTD-based water vapor observations are advantageous for weather predictions as the humidity observations in the atmosphere are generally under-represented in current weather models and limit the accuracy of rainfall predictions. To date, GNSS meteorology largely uses the same stations that were installed by governmental or private institutions for geodetic purposes. These stations are characterized by high data quality provided by cost-intensive (several thousand dollars) equipment. The network density is oriented towards fulfilling specific positioning requirements and subject to financial budget limitations in many areas of the world. As a result, some parts of the world, especially in the Global South, have no or only very sparse coverage by permanent GNSS stations. Additional installations of the conventional GNSS equipment are economically problematic.

In recent years however, the GNSS receiver technology rapidly evolved and resulted in affordable cost-efficient equipment which opens the potential for densification of existing networks or installation of new networks in underserviced areas. These new technologies and low-priced equipment not only come with material and logistic demands but also with technological trade-offs between their expensive counterparts which result in scientific challenges that must be solved. In this thesis, the ZTD and PWV estimation with single-frequency receivers using the SEID model using two different outside GNSS networks is investigated. Furthermore, the ZTD and positioning precision of a low-cost dual-frequency receiver and antenna setups are evaluated. To significantly improve the performance of low-cost antennas, a relative antenna calibration was realized. The applications were demonstrated in field experiments.

In chapter 2, the feasibility of using low-cost single-frequency receivers for densifica-

tion of existing networks is evaluated. At the time of the study, single-frequency receivers were the only cost-efficient alternative to their expensive dual- or multi-frequency counterparts. Using only a single frequency imposes a challenge to eliminate the delay caused by ionized particles in the atmosphere. A possible solution is to utilize a model to estimate the ionospheric delay based on a surrounding dual-frequency network. For this purpose, we used the Satellite specific Epoch differenced Ionospheric Delay (SEID) model and evaluated the performance experimentally. The main part of the experimental setup was placed at the NMi in Delft, Netherlands. At the NMi, two different single-frequency receivers and antennas were installed additionally to the permanent geodetic multi-frequency receivers. The co-located IGS station DLF1 was used in single-frequency mode and as a reference. As surrounding SEID network to account for the ionospheric errors, two different scenarios were investigated with outside station distances ranging from 80 to 300 km. This allowed simulating more realistic conditions to those outside of developed areas. The results demonstrated that low-cost single-frequency receivers can achieve almost identical ZTD estimations (RMSE between 4 and 10 mm) compared to high-cost receivers. This is very promising for the use of low-cost receivers to complement existing networks. At the same time, it was found that clock and hardware errors introduced by the receiver itself are very low and that the results depend mostly on the correct modeling of the ionosphere and on the antenna type.

As the low-cost receiver technology further progressed, low-cost dual-frequency receivers became widely available. With observations on two frequencies, the ionosphere-free linear combination can be applied to eliminate the majority of the ionospheric error in the data. This enables the stations to be used without modeling of the ionosphere by a surrounding network. The drawback is that the measurement noise in the observations is almost tripled. The results in chapter 3 show that the new receiver type itself is very well capable of being used for ZTD estimations. However, without any receiving antenna corrections in case of low-cost antennas, the introduced noise makes the observations impractical for atmosphere monitoring purposes. The observed biases were between 5 and 10 mm. With strong near-field effects, these increased up to 24 mm. To overcome this limitation, we introduced a relative antenna calibration procedure, applied directly in the field. The results showed that the performance of the low-cost antennas in terms of ZTD precision were brought to the same level as high-quality antennas (negligible biases and about 4 mm RMSE) and therefore enables high quality ZTD estimations with a combination of low-cost receivers and antennas.

Meteorological applications of cost-efficient receiver setups are important and clearly suggest an attractive possibility to expand existing networks or installing new GNSS stations in sparsely covered areas. This application is only one out of many possibilities from the available GNSS application spectrum. The main industry application of GNSS revolves around positioning applications. In chapter 4, the performance of the introduced antenna calibration procedure is evaluated in detail for positioning applications. An online web service is presented that allows users to generate antenna calibrations for their antennas directly in the field. The results demonstrate residual improvements in particular for the low-cost antennas. Comparing the residuals to a geodetic reference antenna, the differences were between 30-90% on L1 and L2 before calibration and were reduced to 12-52% after the calibration. A greater azimuthal dependency for the lower

priced antennas compared to the higher cost ones was also found. In terms of positioning performance, the results in the vertical component on a short baseline could be improved from about 6-7 mm RMSE to 4 mm, a level that is very close to the performance of the geodetic-grade antennas.

Perspectives

The work reported in this thesis sparks new scientific questions and opens new application opportunities, especially for meteorology and local positioning applications.

Potential for Numerical Weather Prediction

The low-cost dual-frequency equipment in combination with the introduced calibration procedure from this thesis offers the possibility to install and densify networks of GNSS stations in currently underserviced regions, especially in the Global South. The insufficient quantity of GNSS stations in these regions is partly caused by the high installation costs which makes the operation of GNSS networks economically not viable for most countries. Great potential exists to use cost-efficient stations for meteorological applications, in particular because the quality of weather forecasts in these areas is typically poor quality. Existing station networks lack the density to capture fine-scale atmospheric water vapor movements. The increased station density allows to gain much insight on the conditions leading to extreme weather events in these areas.

Weather characteristics in the Global South differ significantly from those in temperate regions of the northern hemisphere. Rainfall is often of convective nature and typically of high intensity with high spatiotemporal variability. Modeling and forecasting of tropical convection remain a huge challenge for numerical weather prediction models and large model biases exist. The current coarse observation networks do not represent flows within deep convective storms well and cause models to be unable to capture high-intensity events effectively. For a future study, the assimilation of GNSS data under different climatic and regional conditions (e.g. small-scale characteristics of the African easterly jet or West African Monsoon) can be investigated. The assimilation of observations derived from a dense GNSS network in this area will presumably have a significant impact on the rainfall predictions, since the currently under-monitored atmospheric humidity is crucial for precipitation forecasting. Improved rainfall forecasts will directly impact daily life and has great economical influence on agriculture and management of flash floods. Increasing the value of local forecasts over several days, but also even over shorter time spans, will be of great benefit for the local population.

Regarding climate modeling, new data is particularly useful in under-monitored areas since regional trends and interannual variations sometimes deviate from previous observations. It is therefore essential to monitor the water vapor with respect to climate analysis. Longer time series of an increased number of stations will help to improve the long-term accuracy of weather models or improve model calibrations. With globally increasing temperatures, the atmosphere consists of higher potential energy (and thus increased water vapor) which in turn causes more extreme weather events that make the monitoring and integration into weather prediction models increasingly important.

FUTURE NOWCASTING APPLICATIONS

While the warning of severe weather is of special relevance, the accurate forecast of such events with complex weather models still proves to be difficult. This is even more pronounced in data scarce regions. As an alternative, nowcasting applications based on near-real time observations can be used to alert affected parties. Nowadays, it is common practice to use precipitation observations derived from ground radar data as primary data source for this. The limitations are that the availability of these radars is limited outside of developed areas and that the radar data can only detect precipitation that has already been formed, whereas PWV (e.g. derived from GNSS observations) can indicate rainfall before droplets form. However, using solely GNSS observations for this purpose is not a sophisticated approach because single parameters alone are not decisive enough and abnormal PWV measurements are not necessarily related to severe rainfall. Therefore, the use of such parameters must be carefully evaluated. Instead, the combination with a wide range of different measurements should be considered. An interesting question to investigate is the synergy of different instruments (e.g. GNSS, radiosondes, water vapor radiometers, radar measurements) to characterize the conditions leading to specific events. The obtained insights can be used to evaluate and improve rainfall forecasts but also to obtain thresholds and indicators of such events to set up novel nowcasting applications. The use of artificial intelligence algorithms for nowcasting is promising for areas with a long observation history with high-quality measurements, where large training datasets are available.

IONOSPHERE MONITORING

Another potential future application field is the ionosphere monitoring. The presented work was performed under favorable ionospheric conditions. New sensor installations in regions with generally more intense and highly variable ionospheric activity also triggers new scientific opportunities. Particularly to mention are equatorial plasma bubbles (with known scales between cm up to about 1000 km) and scintillations caused by ionospheric disturbances that scatter and degrade radio waves. Even though the noise amplified by using the ionosphere-free linear combination when using low-cost antennas can be mitigated by calibrations, it remains unknown what accuracy can be achieved under these conditions. On the other hand, this opens opportunities to effectively monitor and improve our understanding of the physical properties leading to such phenomena. The occurrence and physical relationships across different regions along the geomagnetic equator have not been exhaustively investigated yet and can be explored with newly setup stations.

POSITIONING OUTLOOK

Apart from meteorological applications of GNSS, a major application of GNSS is for positioning purposes. Previously, the use of low-cost GNSS equipment for precise purposes was a side phenomenon. Now, this limitation can be overcome, and cost-efficient (permanent) installations are possible. Potential applications include surveying and other tasks that rely on high-quality positioning measurements. One possible application of low-cost GNSS setups is to monitor infrastructure to detect rigid and non-rigid changes of the structure position. Wind, land subsidence or hazardous events like landslides,

floods and earthquakes can adversely affect the stable position of structures (e.g. buildings, dams or natural landscapes) and induce damage or even total collapse. Such disasters can lead to a loss of human lives and large economic damages. The monitoring can improve the safety of structures and reduce the risk of failure. Currently, only a few selected infrastructures are continuously monitored of which even less are in developing countries. With new GNSS setups an increasing number of critical infrastructures can be monitored at low cost in the future. The data can be used for risk assessment tasks and may ultimately also lead to improved performance of failure models (e.g. for insurance affairs). Additionally, the application areas can be also expanded to hazardous areas (e.g. hill slides, volcano sites, lightning-prone or generally crime and safety-related locations). The design of monitoring networks with one or more reference stations for these tasks is a potential future topic where high-precision requirements apply. Though the current low-cost technology can provide accurate 3D displacement information, current limitations that need further improvements are e.g. multipath mitigation strategies, additional sensor integrations, or measurement-noise related fields.

Towards Market Implementation and Practical Recommendations

The use of low-cost GNSS receivers and methods demonstrated in this thesis show good potential to be used operationally in diverse applications.

To get the low-cost setup fully ready for field implementation, the receiver should be incorporated into a solid housing together with data transmission and battery recharge and management hard- and software. The reliable data recording and transmission, as well as potential automatic software processing need to be implemented. With these basic requirements fulfilled, wide-spread installations of additional GNSS receivers can be done.

Specially cases with less homogeneous antenna phase patterns over azimuth directions, the calibration method needs increased robustness to properly correct for multipath effects in the field. This effect can be inherited by the antenna design or increased multipath effects e.g. caused by objects in the near field. To this end, a first step is to rotate the rover antennas in several intervals and to increase the number of observation days. This results in additional observations in elevation and azimuth directions. It will improve the current interpolation strategy, with better outlier smoothing and filling gaps in azimuth direction. Further measurements in azimuth direction can also be obtained by considering different GNSS satellites that share the same center frequency. Sufficient data and carefully performed antenna rotations open the way for an azimuth- and elevation-based antenna calibration.

Ideally, calibration patterns are applicable to all antennas of the same model. To investigate repeatability of antenna calibrations, a major question left to be answered is if the individual calibrations of low-cost antennas can be applied to other antennas of the same model (type mean calibrations). A possible way to achieve this would be to investigate additional antennas of the same kind and compare the calibrations among each other. However, the possibility to obtain a wide range of calibrations from different suppliers also exists with the implemented web-tool. By analyzing crowd-sourced

data submitted by the users of the implemented web-tool, further analyses can be conducted. Furthermore, the comparison to absolute antenna calibrations is recommended - whether these are supplied by the manufacturer or obtained by anechoic chamber or absolute field calibrations with a robotic arm.

A complete calibration of GNSS antennas include horizontal and vertical offsets. The positioning results from the presented calibration method are mainly focused on the vertical component. To provide a full offset calibration, it is advisable to also include the horizontal offsets into the current calibration strategy. This implies to set up an experimental scenario which measures these with high confidence. Since the current method is based on GPS-only observations, a way to include multiple GNSS constellations to the current procedure is to introduce intersystem translation parameters. With multi-GNSS, the tracked satellites will be more spread out in the sky which will have a positive impact on the position dilution of precision and allows to achieve even better repeatability of position estimations.

To exploit the advantages of low-cost hardware e.g. for meteorological purposes, a dense network appears warranted. With a dense network of GNSS receivers, advanced geodetic techniques such as GNSS tomography can be applied. With GNSS tomography, the 3D refractivity field in the atmosphere can be obtained which can be directly assimilated into weather models. An increased network density gives an increasing amount of potential intersection points. Utilizing a dense network of low-cost GNSS equipment for this purpose was not performed yet and appears promising considering the high-quality observations that can be achieved with the cost-efficient setups presented in this thesis.

Since GNSS serves as a driver for productivity across the economy (farming, construction, mining, ...), areas relying on cost-efficient solutions will especially benefit from additional GNSS installations. The widespread installations will facilitate new business areas for the local population while benefiting scientific applications at the same time.

ACKNOWLEDGEMENTS

Though the single author name of this thesis is my own, I see this dissertation as a collection of experiences and accomplishments of the previous four and a half years. This time is without doubt characterized by memories of colleagues, friends and family without which I could not have achieved this.

First and foremost, I would like to express my sincere and deepest gratitude to my daily supervisor Marie-Claire ten Veldhuis. I could not even imagine having done this without your guidance and support. You inspired me throughout this long period and whatever my aspirations were, you always took time aside to give me good advice.

To Nick van de Giesen, thank you for the inspiration, motivation and showing the real-world application perspectives of the topics we were working on together. I have learned a lot from these years. A big thanks also goes to Hans van der Marel and Eugenio Realini. Only with your scientific and technical guidance I could expand my GNSS knowledge. Thank you for the challenging feedback and contributions. Every single time we discussed our findings, I could learn new things and could broaden my horizon to think about new interpretations.

To Ruud de Jong, thank you for your help to install and uninstall the GNSS stations in Rotterdam. It is such a relief to have someone as helpful and supportive as you.

A special thanks to Hessel Winsemius, Christian Tiberius, Ivan Gayton, Iddy Chazua, George Sserwadda and Richard Cliffe Ssenyunzi for the help and the interesting projects we were working on together, whether directly or with Master or Bachelor students for projects in Tanzania, Indonesia, Uganda and in the Netherlands.

I am also very grateful for my colleagues at TU Delft. Particularly Lydia and Betty, as well as my office roommates Camille, Petra, Bahar, Coco, Fransje and Jeroen. Even in stressful times you lightened up my life as a PhD candidate. I always enjoyed the lively discussions and our collective attitude to help each other. Especially since the lockdown, I realized how much I miss the lively environment in our office. Props to my amazing bouldering mates: Petra and Camille. Thank you for our weekly bouldering sessions. This is something I was looking forward to every week.

Thanks to Monica, Cynthia, David, Tian, Sha and Camille from the weekly 'score meeting group'. This group shows how diverse the topics of Water Management can be. The interactions with you helped me to feel at home in the department and to look beyond my own research topic.

To Charles Troupin: I am convinced that my scientific attitude was strongly influenced by the work we did together. Thank you for your support beyond the work even after I went to Delft.

For my mental health and the keep-on-going attitude I wish also to thank my friends in Germany: Janina, Marie, Elsa, Leon, Patrick, Jannik, Daniel, Tobias and Thomas. Especially Janina for her proofreading help and the lively discussions we had.

Finally, I would like to acknowledge my family for their entire continuous support – especially my brother and my father who helped me a lot with practical questions and solutions.

CURRICULUM VITÆ

Andreas KRIETEMEYER

04-01-1989 Born in Neubrandenburg, Germany.

EDUCATION

2016–2021 **PhD. Water Resources Management**
Delft University of Technology, the Netherlands
Thesis: Perspectives of cost-efficient GNSS equipment for wide-spread and high-quality meteorological and positioning applications
Promotors: Prof. dr. ir. Nick van de Giesen
Dr. ir. Marie-Claire ten Veldhuis

2012–2014 **M. Eng. in Geoinformatics and Geodesy**
University of Applied Sciences Neubrandenburg, Germany
Thesis: Computation of Precipitable Water Vapour Using GPS and Sparse Publicity Available Meteorological Data - Case Studies in New Zealand and Europe

2009–2012 **B. Eng. in Geoinformatics**
University of Applied Sciences Neubrandenburg, Germany
Thesis: Maintainance and Continuation of 3D city models in the 3D City Database and the CityServer3D

1999–2008 **Abitur**
Gymnasium, Altentreptow, Germany

WORK EXPERIENCE (SELECTION)

since 2021 **Research Engineer**
Expansion of the monitoring network at the islands of Saba and St. Eustatius, R&D Department of Seismology and Acousistcs (R&DSA), Royal Netherlands Meteorological Institute (KNMI), Ministry of Infrastructure and Watermanagement
De Bilt, The Netherlands

2019 **Technical Specialist**
Provision, training and usage of advanced GNSS surveying techniques for employees of the Humanitarian OpenStreetmap Team
Dar Es Salaam, Tanzania

2015–2016 **IT Engineer**
Data processing, quality control and visualization of atmospheric and oceanographic observations, Balearic Islands Coastal Observing and Forecasting System (SOCIB)
Palma de Mallorca, Spain

2015 **Freelancer**
Multiple service contracts for the Universities of Applied Sciences Neubrandenburg & Stralsund on website development and implementation of interactive online Math exercises in LON-CAPA
Neubrandenburg & Stralsund, Germany

AWARDS

2019 **EC Student Grant**
to orally present at the conference ESA Living Planet Symposium 2019, Milan, Italy

2014 **Best student in Geoinformatics and Geodesy**
awarded by the University of Applied Sciences Neubrandenburg and Sparkasse Neubrandenburg-Demmin

2013 **PROMOS stipend**
awarded by the German Academic Exchange Service to co-finance the 6-month research stay in Dunedin, New Zealand

List of Publications

Peer Reviewed Journal Articles

4. **Krietemeyer, A.**, van der Marel, H., van de Giesen, N. & ten Veldhuis, M.-C., *A field calibration solution to achieve high-grade level performance for low-cost dual-frequency receiver and antennas*, Submitted to GPS Solutions (2021).

3. **Krietemeyer, A.**, van der Marel, H., van de Giesen, N. & ten Veldhuis, M.-C., *High Quality Zenith Tropospheric Delay Estimation Using a Low-Cost Dual-Frequency Receiver and Relative Antenna Calibration*, Remote Sensing, 12(9), 1393 (2020).

2. **Krietemeyer, A.**, ten Veldhuis, M.-C., van der Marel, H., E. Realini & van de Giesen, N., *Potential of cost-efficient single frequency GNSS receivers for water vapor monitoring*, Remote Sensing, 12(9), 1493 (2018).

1. Ličer, M., Mourre, B., Troupin, C., **Krietemeyer, A.**, Jansá, A. & Tintoré, J., *Numerical study of Balearic meteotsunami generation and propagation under synthetic gravity wave forcing*, Ocean Modelling, 111, 38-45 (2017).

Popular Scientific Writing

1. **Krietemeyer, A.**, *Irrigating the data desert: A cheap solution to extreme weather forecasting.*, ExtraCT (Studievereniging van studenten Civiele Techniek aan de TU Delft) Jaargang 21, Water Management Special, 20 - 21, (2018)

Oral and Poster Presentations

18. **Krietemeyer, A.**, van der Marel, H. ten Veldhuis, M.-C. & van de Giesen, N., *Improving the antenna performance for Zenith Tropospheric Delay estimations with consumer-grade antennas and a low-cost dual-frequency receiver, Online Display*, EGU General Assembly Conference Abstracts, 9663 (2020).

17. Winsemius, H., **Krietemeyer, A.**, van Dongen, K., Gayton, I., Annor, F., Tiberius, C., ten Veldhuis, M.-C., Samboko, H., Hut, R. & van de Giesen, N. *Low-cost, high accuracy Global Navigation Satellite System positioning for understanding floods, Online Display*, EGU General Assembly Conference Abstracts, 8446 (2020).

16. **Krietemeyer, A.**, van der Marel, H. ten Veldhuis, M.-C. & van de Giesen, N., *Creating relative antenna pattern corrections to improve the performance of a low-cost dual-frequency receiver for Zenith Tropospheric Delay estimations, Speaker*, International Workshop on Improving GNSS and SAR Tropospheric Products for Meteorology, Luxembourg (2019).

15. **Krietemeyer, A.**, van der Marel, H. ten Veldhuis, M.-C. & van de Giesen, N., *Using Low-Cost Single-Frequency GNSS Stations for Water Vapor Estimation, Speaker*, ESA Living Planet Symposium, Milan, Italy (2019).

14. **Krietemeyer, A.**, van der Marel, H. ten Veldhuis, M.-C. & van de Giesen, N., *What we learned for rainfall analysis using tropospheric gradients and slant zenith tropospheric delays, Speaker*, EGU General Assembly Conference Abstracts, 9663 (2019).

13. **Krietemeyer, A.**, van der Marel, H. ten Veldhuis, M.-C., Realini, E. & van de Giesen, N., *Using low-cost GNSS receivers to densify existing GNSS water-vapour monitoring networks, Speaker*, EMS 2018, Session OSA 1.6 Meteorological observations from GNSS and Copernicus satellites (2018).

12. **Krietemeyer, A.**, van der Marel, H. ten Veldhuis, M.-C., Realini, E. & van de Giesen, N., *Densified GNSS-based water-vapour monitoring network in Rotterdam using low-cost single-frequency receivers, Poster*, EGU 2018, Session G5.2 Atmospheric Remote Sensing with Space Geodetic Techniques (2018).

11. van de Giesen, N., **Krietemeyer, A.**, ten Veldhuis, M.-C. & Annor, F., *TWIGA: Sensors for geo-services in Africa. Early results, perspectives, and an invitation, Poster*, EGU 2018, Session HS1.1 The MacGyver session (2018).

10. **Krietemeyer, A.**, ten Veldhuis, M.-C., van der Marel, H., Realini, E. & van de Giesen, N., *Low-cost sensors for high resolution water vapor monitoring in Rotterdam, Poster*, EMS 2017, OSA2.7/UP3.7 High-resolution precipitation monitoring for hydrological and climate-related applications (co-organized) (2017).

9. Mourre, B., Ličer, M., Troupin, C., **Krietemeyer, A.**, Jansá, A. & Tintoré, J., *Modelling high-frequency sea level oscillations associated with meteotsunamis over the Balearic shelf, Presentation*, Altimetry for coastal/regional ocean models, GODAE - COSS TT Workshop ICM-5, April 2017 (2017).

8. Ličer, M., Mourre, B., Troupin, C., **Krietemeyer, A.**, Jansá, A. & Tintoré, J., *Numerical Study of Balearic Meteotsunami Generation and Propagation under Synthetic Gravity Wave Forcing, Poster*, OS2.3 Oceanography at coastal scales. Modelling, coupling and observations, EGU April 2017 (2017).

7. **Krietemeyer, A.**, ten Veldhuis, M.-C., van der Marel, H., Realini, E. & van de Giesen, N., *Using Low-Cost GNSS Receivers to Investigate the Small-Scale Precipitable Water Vapour Variability in the Atmosphere for Improving High Resolution Rainfall Forecasts, Poster*, HS7.8 Precipitation and Urban Hydrology, EGU April 2017 (2017).

6. **Krietemeyer, A.**, ten Veldhuis, M.-C., van der Marel, H., Realini, E. & van de Giesen, N., *Investigating the Small-Scale Spatial Variabilty of Precipitable Water Vapour by Adding Single-Frequency Receivers into an Existing Dual-Frequency Receiver Network, Poster*, G5.2/ AS4.44/ CL2.20 Atmospheric Remote Sensing with Space Geodetic Techniques (co-organized), EGU April 2017 (2017).

5. Mourre, B., Ličer, M., Troupin, C., **Krietemeyer, A.**, Jansá, A. & Tintoré, J., *Balearic Rissaga Forecasting System: recent progress and study of meteotsunami propagation under synthetic gravity wave forcing, Presentation*, Advances in Oceanographic Modelling in the Mediterranean Sea, MonGOOS Workshop November 2016 (2016).

4. Mourre, B., Ličer, M., Troupin, C., **Krietemeyer, A.**, Jansá, A. & Tintoré, J., *Balearic Rissaga Forecasting System: studying meteotsunami propagation under synthetic gravity wave forcing and revisiting the 2006 event, Presentation*, Planet Ocean, A tribute to Drs. Marta

Estrada, Jordi Font and Jordi Salat, pioneers of modern Mediterranean oceanography, XXXII Trobades cientifiques de la Mediterrania - Josep Miquel Vidal, October 2016 (2016).

3. Troupin, C., Frontera, B., Sebastián, K., Beltran, J.P., **Krietemeyer, A.**, Gómara, S., Gomila, M., Escudier, R., Juza, M., Mourre, B., Garau, A., Cañellas, T., March, D. & Tintoré, J., *Medclic: the Mediterranean in one click by C. Troupin et al. (2016), Services for Users and Education, Poster*, IMDIS - International Conference on Marine Data and Information Systems October 2016 (2016).

2. Troupin, C., Frontera, B., Sebastián, K., Beltran, J.P., **Krietemeyer, A.**, Gómara, S., Gomila, M., Escudier, R., Juza, M., Mourre, B., Garau, A., Cañellas, T., March, D. & Tintoré, J., *Data processing and visualisation at the Balearic Islands Coastal Observing and Forecasting, Poster*, Data Services in ocean science, IMDIS - International Conference on Marine Data and Information Systems October 2016 (2016).

1. Troupin, C., Frontera, B., Sebastián, K., Beltran, J.P., **Krietemeyer, A.**, Gómara, S., Gomila, M., Escudier, R., Juza, M., Mourre, B., Garau, A., Cañellas, T., March, D. & Tintoré, J., *Medclic: the Mediterranean in one click by C. Troupin et al. (2016), Services for Users and Education, Poster*, ESSI1.1, Informatics in Oceanography and Ocean Science, EGU April 2016 (2016).